Impact of Beam Strength on Seismic Performance of Chevron Concentrically Braced Frames

Clare Terpstra

A thesis

submitted in partial fulfillment of the

requirements for the degree of

Master of Science in Civil Engineering

University of Washington

2017

Committee:

Charles W. Roeder, Chair

Jeffrey W. Berman

Dawn E. Lehman

Program Authorized to Offer Degree:

Civil and Environmental Engineering

University of Washington

Abstract

Impact of Beam Strength on Seismic Performance of Chevron Concentrically Braced Frames

Clare Terpstra

Chair of the Supervisory Committee:
Professor Charles W. Roeder
Civil and Environmental Engineering

Special concentrically braced frames (SCBFs) are a popular choice for lateral force resisting systems in regions of high seismicity. SCBFs with braces oriented in a chevron (or inverted V) configuration are often preferred for their architectural advantages. Current design provisions require the beam in chevron SCBFs to develop the unbalanced load resulting from one brace at its maximum tensile capacity and the other brace at a significantly degraded compressive capacity. This results in large, expensive beam sections in chevron SCBFs and as a result the popularity of this system has declined. Very little research has been done to support the current beam strength provisions, and several studies have indicated that beams that do not meet this requirement still allow the system to achieve adequate strength and ductility.

The objective of this research is to systematically evaluate the effect of beam strength on the seismic performance of chevron SCBFs. Three full-scale frames were tested under a quasi-static cyclic displacement history to achieve this objective – one with a beam that met current strength provisions and two with beams weaker than currently required. The results show that chevron SCBFs with yielding beams achieve somewhat smaller lateral resistance but increased ductility and energy dissipation compared to frames that meet current beam strength requirements.

Table of Contents

List of Figures

List of Tables

Acknowledgements

I would first like to thank my advisors, Professors Charles Roeder, Jeffrey Berman, and Dawn Lehman for their support and guidance throughout my master's degree. I am extremely grateful for the opportunity they have given me to make an impact on the engineering community and to develop as an engineer. I have learned so much from their input on this research project and will miss the lively discussions in our weekly meetings.

Thank you to Marsha Swatosh who taught me (almost) everything I needed to know to conduct experimental work in the lab and who allowed me to join her office's soccer team. Travis Thonstad and Max Stephens were always there when I needed advice or assistance in the lab, even though they were busy finishing their dissertations. Andy Sen was an invaluable resource – he always had the answer to my questions and was a master at controlling the actuator during the tests. Andre La Rosa, Michael Hanek, John Hastings, and Laura Hillman were dedicated lab assistants who made fabrication and testing of the frames much easier and more enjoyable.

I would like to thank Vince C., the lab technician, for his support for the 10 months I was working in the lab. His depth of experience was a valuable asset in the lab and I will miss our Teriyaki lunches. Thank you to Doug Lindblad for being the world's best ironworker and providing high-quality welds for the frames. Thank you to Otto aka "Lil' Man" for keeping me company while Doug was welding.

Thank you to my cubicle-mate, neighbor, and mortal enemy Leikune Aragaw who provided me with much distraction during the writing of my thesis. My time in grad school would not have been the same without our friendship. Abby Christman, Tom Lin, Cassie Gills, Sara Ibarra, and many other graduate students made my experience at UW More enjoyable.

Thank you to AISC for providing funding for this research project and for hiring me as an intern when I was an undergraduate at Northwestern.

Most of all I would like to thank my family for their unconditional love and support from across the country.

Chapter 1

Introduction

1.0 Background

Concentrically braced frames (CBFs) are a popular choice for lateral force resisting systems in steel construction. They have traditionally been an efficient and economical means of providing lateral strength and stiffness and are familiar to architects, engineers and fabricators. In regions of high seismicity, special concentrically braced frames (SCBFs) are typically used as they allow for a reduction in the design seismic forces because they are specially detailed to ensure ductile behavior in an earthquake. The design of SCBFs includes restrictions on bracing configuration and strength of surrounding beams, columns, and connections.

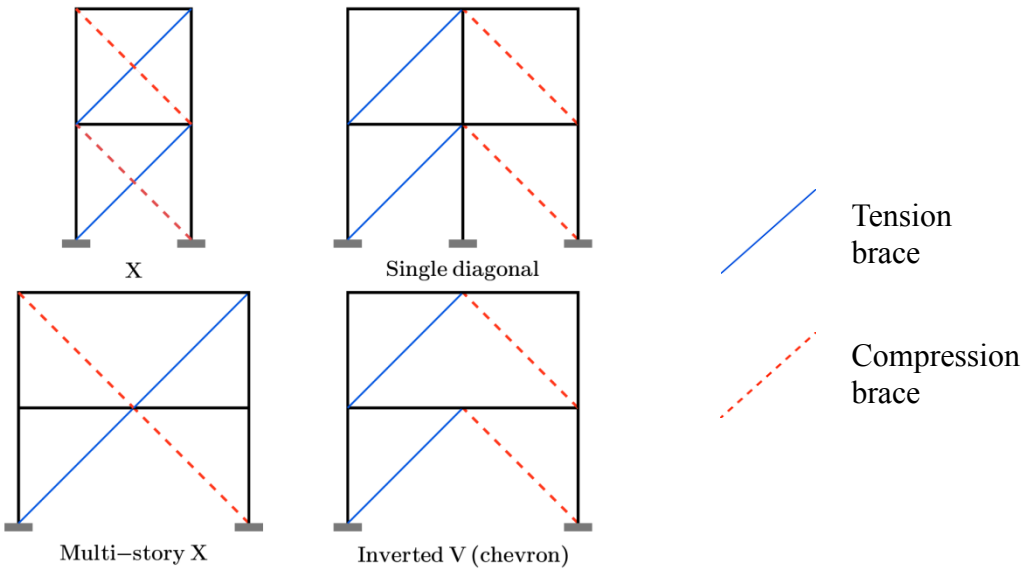

Figure 1.1: Concentrically braced frame configurations.

CBFs resist lateral forces through axial tension and compression in the bracing members. Because the tensile and compressive behavior of the braces differs, braces are typically used in pairs to give the

building symmetric behavior. The braces can be oriented in a variety of ways as shown in Figure 1.1. CBFs with braces oriented in a chevron (or inverted V) configuration are often preferred by architects because they accommodate elements such as doors and windows.

During a severe earthquake, the braces in SCBFs are subjected to large cyclic deformations in tension and compression. Flexural buckling of the brace in compression can lead to formation of a plastic hinge at the brace midpoint and significant cyclic compressive strength and stiffness degradation. The tensile strength of the braces is significantly higher than the compressive strength, and this strength does not degrade over the course of multiple displacement cycles. Because of the difference in in tensile and compressive behavior of the braces under cyclic loading, SCBFs are required to be designed for two analysis scenarios: one where all braces are expected to reach their maximum forces in tension and compression, and one where all tension braces resist their maximum strength while all compression braces resist only 30% of their initial strength. In chevron frames the latter scenario results in a large net vertical force at mid-span of the beam which places a high flexural demand on the beam, as shown in the diagram in Figure 1.2. Consequently, this provision typically results in large, expensive beam sections in chevron SCBFs.

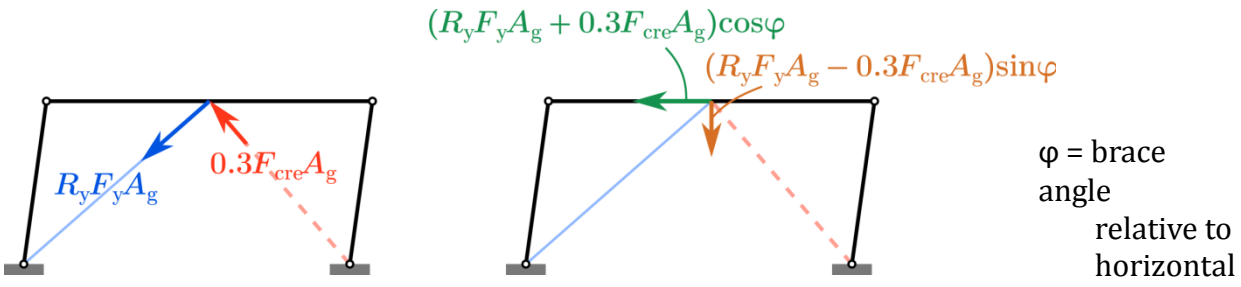

Figure 1.2: Chevron SCBF beam demand.

The current chevron beam strength requirement primarily results from a dynamic test of a six-story chevron CBF that was conducted in Japan in 1981 (described in Section 2.2.1), prior to the development of the current beam strength requirement. There was significant damage to the beams and composite slabs, and brace fracture occurred relatively early in the test. However factors other than beam strength had a significant effect on the frame behavior. The beams had an unusual splice detail at mid-span in the brace connection region that had a negative impact on the beam performance, and the braces used in the frame were not seismically compact which likely caused the premature brace fracture. Since then, studies of chevron CBFs with beams not meeting the current unbalanced load demand (Fukuta et al. (1989) and

Sen (2014)) have shown that these frames can achieve high ductility and effectively dissipate energy with the use of continuous beams and seismically compact braces.

Tests of modern chevron SCBFs by Uriz (2005) and Okazaki (2013) showed that vertical deflection of the chevron beam causes reduced brace elongation in tension and increased brace shortening in compression, but it is unclear how this effects the fracture life of the braces and ductility of the SCBF. Even when the beam is designed for the unbalanced load, elastic beam deflection can prevent the braces from reaching their tensile capacity. These results call into question the appropriateness of the current beam strength provision, especially because it so often results in large and expensive beam sections. The effect of chevron beam strength on the cyclic performance of both the overall CBF system and the braces needs to be systematically studied in order to improve understanding of chevron CBF behavior and to determine appropriate design provisions for chevron beams.

1.1 Research Objectives

The research objectives for the work presented in this thesis are as follows:

- Experimentally evaluate the effect of beam strength on the seismic performance of chevron SCBFs
- Determine the effect of chevron beam strength on the cyclic inelastic behavior and fracture life of the braces
- Determine the effect of chevron beam strength on connection performance
- Evaluate the current chevron beam strength provision based on observed performance
- Propose recommendations for the design of beams in chevron SCBFs

1.2 Document Overview

To address the stated research objectives, this report is divided into five additional chapters. Chapter 2 provides background information for this research project. It presents a short history of CBF design and discusses past research relevant to the issue of beam strength in chevron SCBFs.

Chapter 3 provides descriptions of the design of both the experimental setup and the three test specimens used to achieve the research objectives.

Chapter 4 documents the observed performance of each of the test frames. A series of performance states are defined to facilitate evaluation and comparison of specimen performance. The performance of the three specimens is compared at several drift levels.

Chapter 5 describes the processing and analysis of the data collected during the experiments. The results of the data analysis are used to compare the performance of the overall specimens as well as the individual components of the frames.

Chapter 6 summarizes the research conducted and provides conclusions and recommendations for future work.

Chapter 2

Project Background

2.0 Introduction

This chapter provides context and justification for the research program presented in this thesis. Section 2.1 discusses the evolution of the design provisions for SCBFs, focusing on the provisions that affect chevron CBF beams. Section 2.2 describes the previous research that has investigated chevron CBFs that were designed prior to the development of modern seismic design provisions. Section 2.3 documents the relevant experimental studies that have been conducted on chevron SCBFs designed according to modern standards. Section 2.4 provides a summary of the past research and provides some concluding remarks based on the findings presented.

2.1 Evolution of SCBF Design Provisions

The design of CBFs has evolved considerably since the late 1980s due to extensive research and observed performance of steel buildings during earthquakes. Table 2.1 summarizes the major changes in CBF design requirements since 1988. Modern SCBF design is based upon the principle of capacity design. This approach limits inelastic action to a specific ductile mechanism (in this case brace buckling and yielding) by requiring the capacity of all other possible limit states within the system to be greater. This ensures the system will behave in the desired ductile manner. Prior to 1988, the framing members and connections were designed for approximately the same design seismic forces as the brace. Braces are sized based on their compressive capacity, and as a result the tensile yield strength of the brace is almost certainly greater than the forces associated with seismic loads. For older braced frames this means braces

can attract more force than the frame members and connections were designed for, leading to unexpected failure modes which can greatly reduce the ductility of the system.

Another important development was more stringent brace slenderness and compactness criteria, as ductility of CBFs is highly dependent on brace performance. Non-compact braces experience reduced fracture life due to onset of severe local deformation due to plastic hinge formation at low story drifts, whereas braces that meet modern compactness criteria exhibit ductile behavior even for relatively large compressive deformations.

Table 2.1 Comparison of Pre-1988 and present day CBF design criteria.

Component	**Pre-1988 Requirement**	**Modern (SCBF) Requirement**
Brace Slenderness	No limit	KL/r < 100
Brace Compactness	No limit	Compactness ratio < λ_{hd}
Framing Member Compactness	No limit	Compactness ratio < λ_{md}
Brace End Rotational Clearance	No limit	$2t_p$ linear or $8t_p$ elliptical for corner gusset plates, 6tp for mid-span gusset plates
Connection Design	Design for brace force from seismic loads	Design for expected brace capacity
Framing Member Design	Design for brace force from seismic loads	Design for expected brace capacity
Chevron Beam Design	Design for brace force from seismic loads	1) Design for brace unbalanced load (P_y + $0.3P_{cr}$) 2)Beams must be continuous 3)Provide minimum lateral bracing

Recent work has focused on new methods for improving the deformation capacity of SCBFs. The Balanced Design Procedure (BDP) was proposed by Roeder et al. (2011) as a way to improve deformation capacity of SCBFs by taking advantage of ductile limit states other than brace yielding and buckling. This is achieved by using balance factors to promote desirable yielding mechanisms, such as gusset plate and beam yielding, and prevent undesirable failure modes, such as interface weld fracture. Connections designed according to this method have been shown to increase the deformation capacity of SCBFs (Johnson (2005), Kotulka (2007), Herman (2007), Lumpkin (2008)).

Clearance for brace end rotation is now required in recognition of the high strain demands imposed on connections and adjacent framing members by brace buckling. Traditionally a $2t_p$ linear clearance model has been used, however an elliptical clearance model proposed by Lehman et al. (2008) allows for thinner and more compact gusset plates compared to those designed the with the linear clearance model. These smaller gusset plates are not only more economical but provide increased frame deformation capacity.

In modern chevron SCBFs, capacity design requirements are also applied to the beam. It is required to be sized for the demands resulting from tensile yielding in one brace and an assumed post-buckling compressive strength in the other brace. While in line with capacity design principles, the modern strength requirement for beams in chevron SCBFs can be traced back to a series of tests on a six-story chevron CBF that were conducted in 1981 in Japan (described in Section 2.2.1). The beam deflection, slab damage, and somewhat premature brace fracture that occurred in one test led to the introduction of provisions in the 1988 Uniform Building Code (UBC) that required braces in chevron frames to be designed for 150% of the normal seismic design load. This provision was an attempt to avoid brace buckling as it was believed that buckling and strength degradation after buckling caused the large vertical beam deflections observed in the 1981 test. In the 1994 UBC, the 150% increase in design forces was eliminated in favor of provisions very close to what are used today, namely that the beam must be continuous and must be designed to resist the unbalanced load resulting from the full tensile strength in one brace and 30% of the compressive strength in the other brace. This requirement was adopted by the AISC Seismic Provisions in 1997 and has remained essentially unchanged since then. Relatively little work has been done to justify this beam strength requirement. The relevant studies are presented in the following sections.

2.2 Weak-Beam Chevron CBF Research

2.2.1 United States/Japan: Full-Scale Six-Story Building (Foutch et al. 1987; Roeder 1989)

Experimental testing of a full scale steel building was conducted in 1981 in Tsukuba, Japan as part of the U.S.-Japan Cooperative Earthquake Research Program Utilizing Large-Scale Testing Facilities. The frame was 6 stories tall and 2-by-2 bays, with a chevron CBF located in one bay; the details of which are reproduced in Figure 2.1. The experimental setup, test program, and results have been reported by Foutch et al. (1987) and Roeder (1989). The frame was pseudo-dynamically loaded using actuators at each floor and was subjected to three groundmotions – an elastic, moderate, and final test. The Miyagi-ken-Oki acceleration record was used, scaled to a peak acceleration of approximately 6.5, 25, and 50% of gravity for the three tests. The test specimen was designed based on both the 1976 Uniform Building Code and the 1981 Seismic Design Code of Japan, and represented a blend of current practice in the U.S. and Japan at the time. The beams were designed for composite action and had fully restrained beam-to-column connections. The frames had a rather unusual beam splice detail that was common in Japan at the time, shown in Figure 2.2. Table 2.2, developed by Sen (2014), lists the chevron frame dimensions, member sizes, and unfactored beam demand-to-capacity ratios (DCRs) for axial-flexural interaction due to the brace load combination defined in the AISC Seismic Provisions (AISC 2010a). Brace tensile and compressive strengths are calculated based on documented yield strengths from coupon tests and compression force at buckling in the experiment. All of the chevron beams had an axial-flexural interaction ratio greater than one, meaning they were unable to develop the unbalanced load from the braces and thus fail to meet modern SCBF requirements.

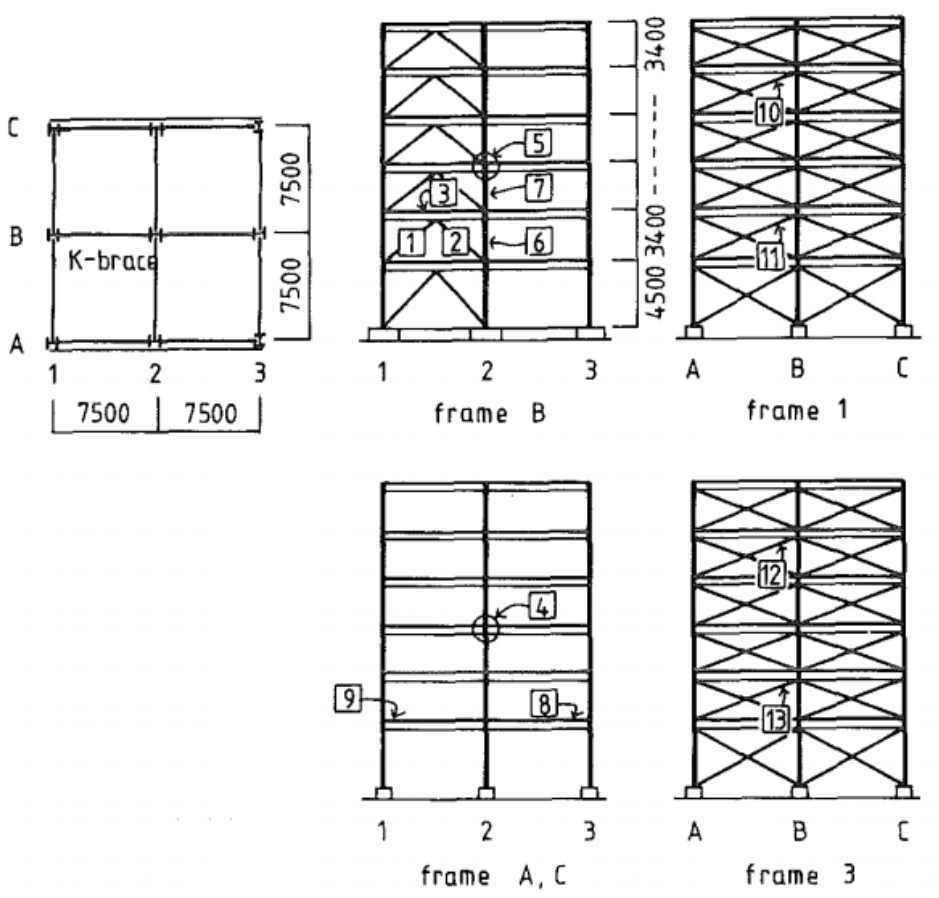

Figure 2.1: U.S./Japan 6-story test frame plan and elevations.

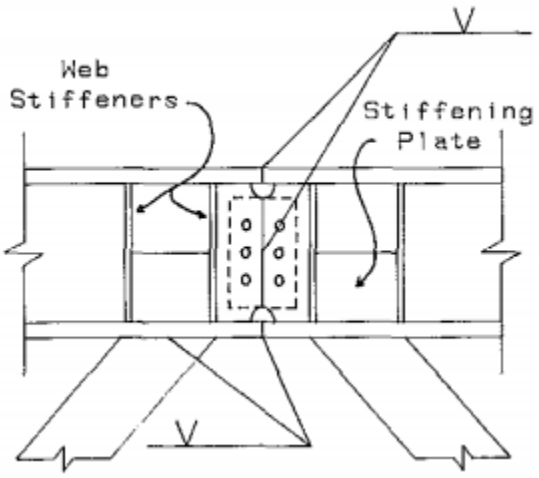

Figure 2.2: Chevron beam splice detail used in U.S./Japan 6-story tests.

Table 2.2 Geometry, members, and beam interaction DCRs in U.S./Japan 6-story test frame (Sen 2014)

Story	Story Height (mm)	Beam Shape	Brace Shape	Beam Interaction DCR
1	4500	W18x40	ST6x6x1/2	3.77
2	3400	W18x40	ST6x6x1/4	1.83
3	3400	W18x40	ST6x6x1/4	1.83
4	3400	W18x35	ST5x5x1/4	1.81
5	3400	W18x35	ST4x4x3/16	1.11
6	3400	W16x31	ST4x4x3/16	1.43*

* P_{cr} estimated using K = 0.82, L = centerline length

Findings

- In the moderate test, limited brace buckling occurred in the second and third floors, while floors 4 through 6 remained essentially elastic. There was no brace buckling on the first floor, however there was a failure of the beam web panel zone at the splice location. This unusual 3-piece tear of the beam web was attributed to several factors. First, the beam was spliced in a location of high shear and bending demand. Second, the brace-to-beam connection geometry caused the beam panel zone to act as a short eccentric shear link. Third, the splice detail involved a bolted splice plate on only one side of the beam web which resulted in an eccentricity that caused twisting and prying of the beam web. The damaged beam splice was repaired before the final test.
- During the final test, more widespread brace buckling occurred. Brace buckling was most severe in the 2nd and 3rd story, and plastic hinging led to local tearing at the corners of the tubular braces at the centers of the braces relatively early in the test. The north brace on the 3rd level ruptured completely and the test was stopped at this point. Slab cracking was observed and was most severe over the brace to beam connections. The second floor composite slab had separated from the steel beam by a few centimeters by the end of the test. The beam splice regions in the second and third story frames experienced similar twisting prying behavior as noted in the first floor beam web failure, but no tearing occurred.
- Brace buckling and yielding were major sources of energy dissipation during the final test, but as the braces tore and fractured, the beams and columns became important secondary sources of energy dissipation. At the beginning of the final test, the braces dissipate approximately 80% of the total energy, while at the end of the test the brace only dissipated 60% of the total energy.
- Composite action increased the initial strength and stiffness of the frame, but deterioration of composite action over the course of the test, supported by strain gauge data, led to loss of this

increased strength and stiffness. As a result composite action did not have a major effect on the structural performance in the final test.

Commentary

The beam splice connection was an unusual detail and is in fact prohibited by the current seismic provisions (AISC 2010a) which require beams in chevron SCBFs to be continuous. The failure observed in this connection is not particularly relevant to the continuous beams used in most chevron frames except to illustrate the high shear and bending demand placed on that region of the beam. Modern connection details typically use a gusset plate to connect the braces to the beam and often include stiffeners at the center of the beam and mid-span gusset plate. This adds significant stiffness to the region making eccentric shear link behavior unlikely. Beam deflection and cracking of the slab contributed to loss composite action and the initial additional strength and stiffness gained from it. However composite action is typically ignored in the design of modern chevron beams. Brace buckling and tearing was an important part of the cyclic behavior of the frame, however is unclear whether the beam performance affected this behavior.

2.2.2 United States/Japan: Half-Scale Three-Story Building (Fukuta et al. 1989)

A series of three-story half-scale chevron CBFs were tested in 1989 as part of the U.S.-Japan Cooperative Earthquake Research Program Utilizing Large-Scale Testing Facilities. The details of the frame design, testing procedure, and results are documented by Fukuta et al. (1989). Six frames were tested under quasi-static cyclic loading – five with chevron bracing and one without bracing. The frame geometry and loading method is depicted in Figure 2.3. The first two specimens had beams designed for composite action and were intended to mimic the first three stories of the 6-story full-scale U.S./Japan test frame described in the previous section. Table 2.3, developed by Sen (2014), shows lists the chevron frame dimensions, member sizes, and unfactored beam DCRs for axial-flexural interaction. Axial and flexural demands were determined using the brace capacities calculated from measured material properties from coupon tests and assuming a brace effective length of 0.58, the average effective length factor observed in

the prototype 6-story tests. All of the chevron beams had an axial-flexural interaction DCR greater than one, meaning they were unable to develop the unbalanced load from the braces and thus fail to meet modern SCBF requirements.

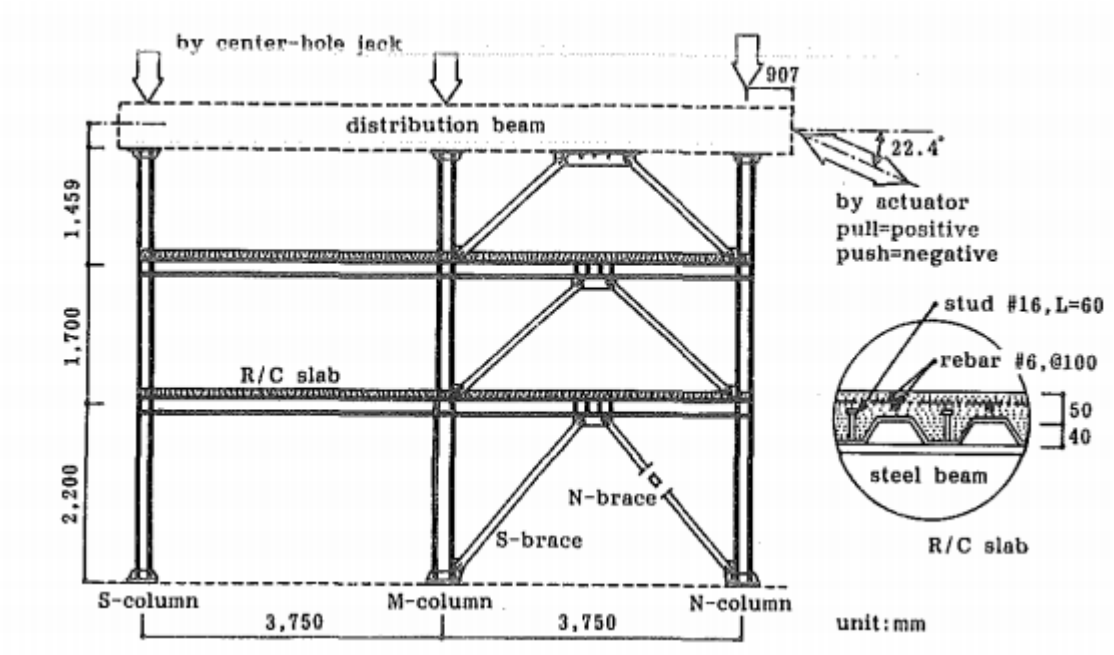

Figure 2.3: U.S./Japan 3-story test frame elevation (Fukuta et al. 1989).

Table 2.3 Geometry, members, and beam interaction DCRs in U.S./Japan 3-story test frame (Sen 2014)

Story	Frame	Story Height (mm)	Beam Shape	Brace Shape (d x b x t)	Beam Interaction DCR
3		1459	Rigid	□—105x45x4.5	<< 1
2	1,2,3	1700	W8x10	□—105x45x4.5	1.82
1		2200	W8x13	□—110x55x4.5	1.92
3		1459	Rigid	□—70x35x6.0	<< 1
2	4	1700	W8x10	□—70x35x6.0	2.31
1		2200	W8x13	□—70x40x9.0	2.80
3		1459	Rigid	□—105x45x4.5	<< 1
2	5	1700	W8x10	□—105x45x4.5	1.60
1		2200	W10x17	□—110x55x4.5	1.17

Based on the experimental results, a simplified hysteresis model for chevron frames was developed that uses plastic analysis to account for the interaction between beam deflection and brace force. The dual lateral system was divided into its respective components, the moment-resisting frame portion and the brace portion. As shown in the equation below, lateral resistance from the tension brace, Q_{bt}, is controlled by the strength of the beam, Q_g, and the strength of the brace in compression, Q_{bc}. The beam strength is limited by the force needed to cause a sway mechanism in the moment frame from plastic hinging at each end of the beam.

$$Q_{bt}(X) = -Q_{bc}(X) - Q_g(X) \leq P_y \cos\theta$$

$$Q_g(X) \leq 2M_{gp}/h$$

where

M_{gp} = full plastic moment capacity of the beam

h = story height

Findings

- The braces contributed about 80% of the lateral resistance in the elastic range and 50% of the lateral resistance in the post-buckling range. The beams and columns were stable against local and lateral-torsional buckling. The load-displacement curves of the braced frame specimens approached that of the moment frame only specimen over the course of the tests
- Composite action (and correspondingly beam flexural strength) did not affect the load at which the braces buckled. Tests 1 and 3 were identical except for the presence of a composite slab in Frame 1. The calculated plastic capacity of the beam in Frame 1 was 2.42 times larger than that of Frame 3, but the braces buckled at the same lateral shear force in each test. Frame 1 did however carry more lateral force in the tension brace than Frame 3. The increased beam strength and stiffness enabled greater elongation in the tension brace.
- None of the braces were able to elongate enough axially to reach their yield strength in tension. Large story drift mainly induced large axial shortening in the compression brace, leading to severe local buckling and plastic hinge formation.
- The proposed hysteretic model showed good agreement with experimental results.

Commentary

This series of tests is the most comprehensive experimental data available on weak-beam chevron CBFs. Even though the first and second story beams were weak with respect to the brace load unbalanced load, the frames were able to effectively dissipate energy. After an initial drop in strength after brace buckling, the frame lateral resistance remained quite stable, even at large drifts. Comparisons between test frames 1 and 3 allowed for important conclusions to be drawn about the effect of beam strength and composite action on the response of the braces. However the frames were only put through a few displacement cycles and were not cycled to failure, so conclusions cannot be made about how brace-beam interaction affects the ultimate behavior of the frame. In addition, all the frames had fully restrained beam-column connections which are not common in braced frame design in the U.S. The proposed hysteretic model tends to slightly over-predict the lateral resistance at large drifts and may become more inaccurate at higher drifts or after a greater amount of brace cyclic strength degradation. Advances in computer performance have decreased the necessity of this type of model, however it is useful in understanding the relationship between beam strength and brace performance.

2.2.3 Numerical modelling of chevron CBFs (Khatib et al. 1988)

A numerical investigation of the cyclic inelastic behavior of chevron CBFs was conducted by Khatib et al. 1988. The study consisted of a review of existing brace models, quasi-static simulation using a stiffness-driven system model, dynamic simulation, and parametric studies. The study aimed at identifying the parameters that influence the inelastic behavior of chevron CBFs, primarily focusing on brace slenderness and beam stiffness. After development of numerical models to study the effect of these parameters, various optimization schemes were run in order to come up with design recommendations for chevron frames.

Findings

- The inelastic behavior of chevron braced frames is complex and requires a system level approach. Focusing on different behaviors or using different loading protocols can lead to different conclusions. For example, modelling just the braces under monotonic compressive deformation led to a recommendation that intermediate slenderness braces be avoided. This recommendation was supported by pushover analysis of a single-bay, 2-story chevron frame which favored stiff beams with stocky or slender braces. However a different optimization procedure led to

recommendation of flexible beams and intermediate slenderness braces, and dynamic analyses discouraged the used of slender braces with stiff beams.

- The inelastic response of chevron frames was highly sensitive to the characteristics of the ground excitation and the tendency to form soft stories.
- The use of stiff beams in multistory chevron CBFs may be counterproductive due to the build-up of large column compressive forces

Commentary

As recognized by the authors, the contradictory results from the different analysis scenarios do not provide much clarity on appropriate design of chevron CBFs. In addition, the issue of beam strength is not directly studied. All beams in the study were assumed to be stiff or flexible with respect to brace stiffness *and* strong with respect to the brace unbalanced load. However relationships between brace, beam, and lateral stiffness were examined in detail and their important effect on system behavior was demonstrated.

2.2.4 Experimental testing of full-scale two-story weak beam chevron CBFs (Sen 2014)

Experimental testing of two-story chevron CBFs was conducted in 2013 at the National Center for Research on Earthquake Engineering in Taiwan (NCREE). The purpose of these tests was to assess the performance of older chevron CBFs in the U.S. to identify their seismic vulnerabilities and design economical retrofit strategies. The two-story full-scale frames were subjected to a quasi-static cyclic displacement protocol using actuators at the top level. Figure 2.4 shows the testing configuration for a typical test specimen. Four specimens were tested; the first represented a typical older, non-ductile chevron CBF and the remaining three tested different retrofit strategies for the first frame. Table 2.4 provides the frame geometry, member sizes, and beam axial-flexural interaction DCRs for each test specimen. All of the frames had weak first story beams with respect to the brace unbalanced load. The first specimen, TNCBF1-N-HSS, had deficiencies other tan beam strength that were typical of older braced frames, such as a non-compact brace section, insufficient gusset plate-to-beam interface weld strength, and insufficient lateral bracing of the beam. The second specimen, TNCBF1-R-HSS, examined an in-plane buckling knife plate retrofit with seismically compact HSS braces on the first floor. The third specimen, TNCBF1-R-WF, consisted of a retrofit with seismically compact wide flange braces on the first floor. Specimen 4, TNCBF2-D-HSS examined a retrofit with out-of-plane buckling seismically compact HSS braces on both floors.

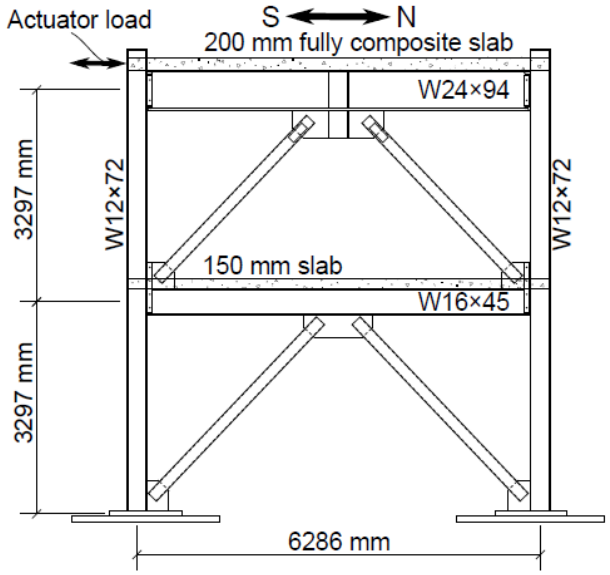

Figure 2.4: NCREE two-story test frame elevation (Sen 2014).

Table 2.4 Geometry, members, and beam interaction DCRs in NCREE 2-story test frames (Sen 2014)

Test Number	Specimen Name	Story	Story Height (mm)	Beam Shape	Brace Shape	Beam Interaction DCR
1	TNCBF1-N-HSS	1	3297	W16x45	HSS7x7x1/4	2.52
		2	3297	W24x94	HSS7x7x1/4	0.42
2	TNCBF1-R-HSS	1	3297	W16x45	HSS5x5x3/8k	2.66
		2	3297	W24x94	HSS7x7x1/4	0.42
3	TNCBF1-R-WF	1	3297	W16x45	H175x175x7.5x11	2.55
		2	3297	W24x94	HSS7x7x1/4	0.42
4	TNCBF2-D-HSS	1	3297	W16x45	HSS5x5x3/8	1.43
		2	3297	W24x94	HSS5x5x3/8	0.44

Findings

- The weak first story beam did not severely impact the performance of any of the four test specimens but was nevertheless influential to the frame behavior in each test
- The ductility of the first specimen was limited by rapid degradation of the non-compact brace in compression. Severe local buckling led to early fracture of one of the braces at less than 0.5% story drift. After fracture the weak beam prevented buckling of the second brace as it was too

weak to develop the brace critical buckling load. This caused an eccentrically braced frame (EBF) mechanism that persisted until connection fracture of the second brace at 1.04% drift. The EBF mechanism was stronger than the moment frame mechanism that began after brace fracture, indicating that the weak beam improved the post-fracture performance of the frame.

- The second specimen was retrofitted with seismically compact in-plane buckling HSS braces which buckled out-of-plane, likely due to the low torsional stiffness of the weak beam and lack of lateral bracing at mid-span of the beam. The frame response was ductile and lateral resistance was maintained until brace fracture at a drift range of 4.6%. Twisting of the beam at mid-span appeared to limit weld damage in the mid-span gusset. The beam deflected significantly under the brace unbalanced load, reaching a maximum of 63 mm (2.5 inches). This placed a large rotational demand at the beam end, resulting in weld cracking at the beam-to-column connection.
- The third specimen also experienced large beam deflection due to the brace unbalanced load, and high rotational demands caused beam-to-column connection damage which was exacerbated by fracture of the second story brace-to-corner gusset connection early in the test and heat effects from multiple weld repairs
- The fourth specimen exhibited ductile behavior, reaching a drift range of 4.12% before brace fracture. The weak beam deflected up to 50 mm (2 inches) which limited the tensile force developed in the braces. In contrast, the strong beam on the second floor was able to develop the tensile yield strength of the specimen. Based on these observations, the braces on the first floor underwent less elongation and more shortening than the brace on the second story.

Commentary

These tests provide valuable data on the behavior of weak-beam chevron CBFs. The weak beam did not negatively impact the ductility of the frames; early failures in the first and third test were due to other deficiencies and the second and fourth specimens reached drift ranges comparable to SCBFs. The strength of the beam may have had an impact on the shear tab-to-beam connection fracture in the third test because of the increased rotational demand at the connection, however it is difficult to separate the contribution of beam end rotation, heat damage from weld repair, and the failure at the second floor corner gusset-to-brace connections. It is clearly important to consider the increase in beam end rotation due to increased deflection of weak chevron beams. Because there were several variables other than beam strength affecting the performance of each frame, it is hard to draw definitive conclusions on the effect of beam strength. However these results suggest that weak beams do not negatively impact frame ductility and may provide a secondary source of energy dissipation.

2.3 Strong Beam Chevron SCBF Research

2.3.1 Experimental test of two-story, full-scale chevron SCBF (Uriz, 2005)

A two-story, single bay chevron SCBF was tested in 2004 at the University of California, Berkeley. The test was part of a broader research program aimed at improving understanding of the behavior of CBFs under cyclic inelastic deformations, validating and improving computer models for predicting CBF behavior, and improving understanding of the relationship between system, member, and connection behavior. The research program consisted of experimental testing of three buckling restrained braced frames (BRBFs) and one chevron SCBF frame, as well as extensive analytical studies. Only the chevron SCBF test is discussed here. Details of the frame design, test setup, and results are documented by Uriz (2005). The test setup, frame geometry, and member sizes are shown in Figure 2.5. The frame was tested in a horizontal configuration, so the beams and columns did not have any in-plane forces associated with gravity loads and were solely designed for the brace forces. The frame was designed according to the requirements of the 1997 AISC Seismic Provisions (AISC 1997), and thus had a beam axial-flexural interaction DCR less than 1 for the unbalanced load from the braces. The columns were designed for the expected lateral resistance of the frame, taken as twice the horizontal component of the brace critical buckling load, multiplied by and overstrength factor of 2. The gusset plate connections were designed to develop the brace tensile and compressive strengths, with force distribution computed using the Uniform Force Method. The simple shear beam-to-column connections were designed for the expected brace forces. The frame was subjected to a quasistatic cyclic displacement history using an actuator attached to the top floor chevron beam.

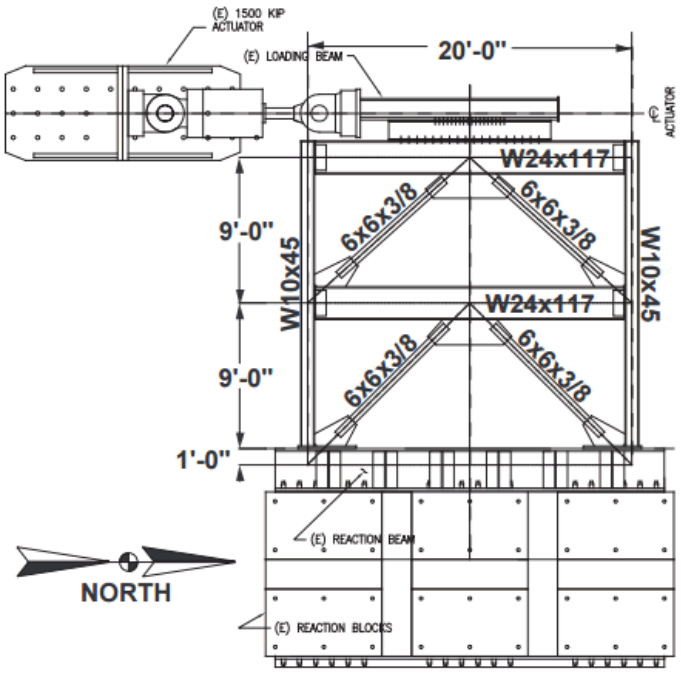

Figure 2.5: Testing configuration for two-story chevron SCBF frame (Uriz 2005).

Findings

- The frame developed a maximum lateral resistance of 135% of the nominal design capacity (taken as twice the horizontal component of the brace critical buckling load). The braces began to buckle at a story drift of 0.45%. After initial brace buckling, the frame behavior was dominated by out-of-plane buckling of the first story braces, followed by concentration of drift demand and eventual fracture of the braces and columns on the lower level.
- By the third cycle at 0.67% story drift, about 85% of the roof displacement had concentrated in the lower level, demonstrating the susceptibility of CBFs to concentrate inelastic damage in a single story
- Once brace fracture occurred in the lower level, significant strength and stiffness was lost and moment frame action was relied on to provide lateral resistance. The moment frame resisted 28% of the maximum lateral force resisted by the specimen.
- The braces did not yield or elongate significantly in tension due to flexibility of the beam. Although the beam is designed to be strong enough to resist yielding due to the tensile capacity in one brace and reduced compression capacity in the other brace, there are no restrictions placed on the deflection of the beam in this configuration. The beam deflected vertically almost 1 inch, reducing the tensile elongation that needs to be developed to yield the brace. This leads to

asymmetric brace hysteretic loops where compressive shortening dominates over tensile elongation.

Commentary

This study represents one of very few tests of chevron CBFs designed according to modern seismic provisions. As such it provides valuable insight into the behavior of capacity designed chevron SCBFs and the effectiveness of current design standards. It is interesting to note that even though the beam was designed for the unbalanced force from the braces, it was unable to develop the tensile strength of the brace because elastic deflection of the beam limited the ability of the brace to elongate in tension. This result calls into question the necessity of designing the beam for this unbalanced load, especially since this provision typically results in very large, expensive beams in chevron SCBFs.

2.3.2 Shake table testing of single-bay, single-story chevron SCBF (Okazaki, et al. 2013)

Dynamic shake table testing of a 70% scale single bay, single story chevron SCBF was conducted at E-Defense, Japan in 2013. Details of the test setup, frame design, and results are reported by Okazaki, et al. 2013. The test specimen geometry and member sizes are shown in Figure 2.6. The frame was designed to meet the requirements of the 2005 AISC Seismic Provisions, thus the beam had an interaction DCR of less than one for the brace unbalanced forces calculated based on nominal brace properties. Coupon tests revealed that the yield strength of the brace material was 56% larger than its nominal yield strength, so the true beam DCR was actually greater than 1. The beam-column connections were fully restrained, and the gusset plate connections were designed using the elliptical clearance model proposed by Lehman et al. (2008). The frame was subjected to the JR Takatori ground motion scaled to 10, 12, 14, 28 (twice), to 42, and finally, 70%.

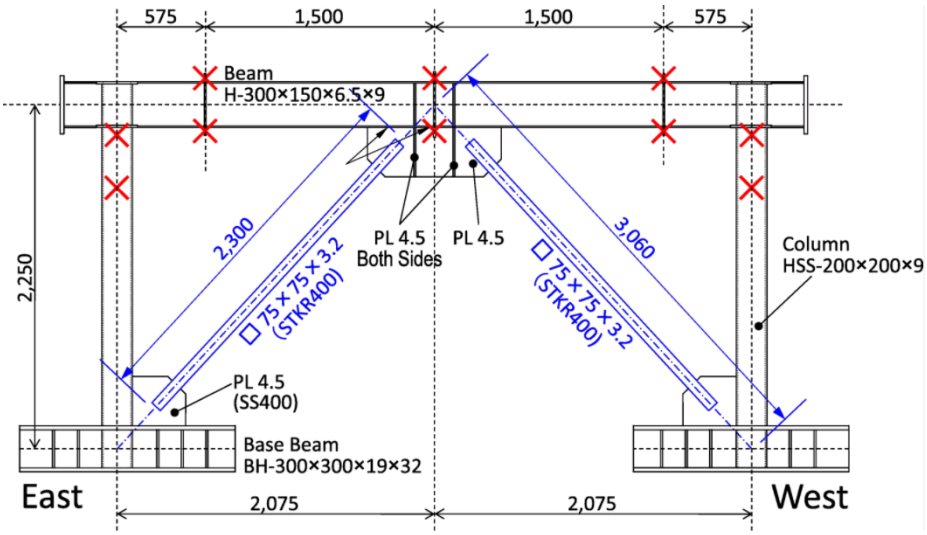

Figure 2.6: Shake table test specimen and out-of-plane bracing points (mm) (Okazaki et al. 2013)

Findings

- The frame responded elastically up through the 28% scaled ground motion and there was some limited brace buckling at the 42% scale. The 70% motion resulted in significant nonlinear behavior in the frame. The braces buckled and fractured within three negative to positive drift excursions between –0.015 and 0.01 rad. After both braces fractured, the specimen acted as a moment-resisting frame with reduced strength and stiffness.
- The specimen failed at a drift range of just over 3.5% which is smaller that ordinarily expected, however this is likely due to the fact that the walls of the HSS brace were relatively thin and did not meet AISC seismic compactness criteria
- Although the frame experienced similar drifts in each direction, the braces developed significantly more shortening in compression than elongation in tension, and the braces did not develop their yield capacity. This behavior was shown to result from beam deflection at mid-span, which reached a maximum of 15 mm (0.6 inches) during the last cycle before brace fracture. Deflection of the beam prevented tensile elongation of the brace and promoted compressive shortening of the brace.

Commentary

This test is one of few experimental evaluations of modern chevron CBFs (although there were a few deficiencies in the frame that prevented it from being an SCBF) and may be the only shake table test of

such a frame. This test replicated the finding by Uriz (2005) that tensile elongation of the brace was limited due to beam vertical deflection.

2.4 Summary of Past Research

Table 2.5 shows a summary of the results of the experimental studies discussed in Section 2.2 and 2.3. Fukushima et al. (1989) and Sen (2014) demonstrated that chevron CBFs with beams that do not meet the current strength requirement can achieve adequate deformation capacity. In tests where brace fracture occurred at relatively low story drifts, the non-compact braces were primarily to blame. The tests on chevron frames with compliant beams achieved smaller story drifts before brace fracture than most of the non-compliant specimens. These results call into question the appropriateness of the current severe strength requirement for beams in chevron SCBFs. The effect of beam strength on frame resistance, deformation capacity, and brace behavior needs to be systematically evaluated in order to determine rational design provisions.

Table 2.5 Summary of relevant experimental research

Test	Stories	Specimen	Brace b/t	Beam DCR*	Interstory drift achieved before brace fracture
U.S./Japan 1981	6	1	19-27.8	1.11-3.77	1.8%
Fukushima et al. 1989	3	1	21.3,22.4	1.82,1.92	6%
		2	21.3,22.4	1.82,1.92	6%
		3	21.3,22.4	1.82,1.92	7.5%
		4	9.7,5.8	2.31,2.80	4%
		5	21.3,22.4	1.60,1.17	3%
Sen 2014	2	1	28	2.52	0.46%
		2	11.3	2.66	2.34%
		3	11.3	2.55	n/a
		4	11.3	1.43	2.27%
Uriz 2005	2	1	14.8	<1	1.35%
Okazaki 2013	2	1	20.4	<1	1.5%

*top story not included

Chapter 3

Experimental Setup and Specimen Design

3.0 Introduction

This section describes the rationale used to design both the test specimens and the experimental setup. The test setup and specimens were designed to achieve the test objectives while simultaneously meeting the constraints of the UW Structural Research Laboratory (SRL). A discussion of this design process is presented, followed by an overview of the final design of the test specimens. Finally, the instrumentation and testing procedure are discussed. Detailed drawings of the components of the test setup and sample calculations for the specimen design can be found in the Appendices 1 and 2, respectively.

3.1 Test Setup Design

The goal of this series of tests was to study the effect of beam strength on the seismic performance of chevron SCBFs. The test setup was designed to allow this effect to be studied under conditions as close as possible to what would be found in an actual building frame. The specimens were built and tested in the UW SRL, so the design was constrained by the layout and available equipment of the SRL. A plan view of the final testing configuration is shown in Figure 3.1. The various components of the test setup are labelled and will be referred to throughout this chapter. The primary considerations in the design of the

test setup were the overall size of the specimen, the position of the specimen within the lab, the method of loading the specimen, and the method of providing the necessary restraint.

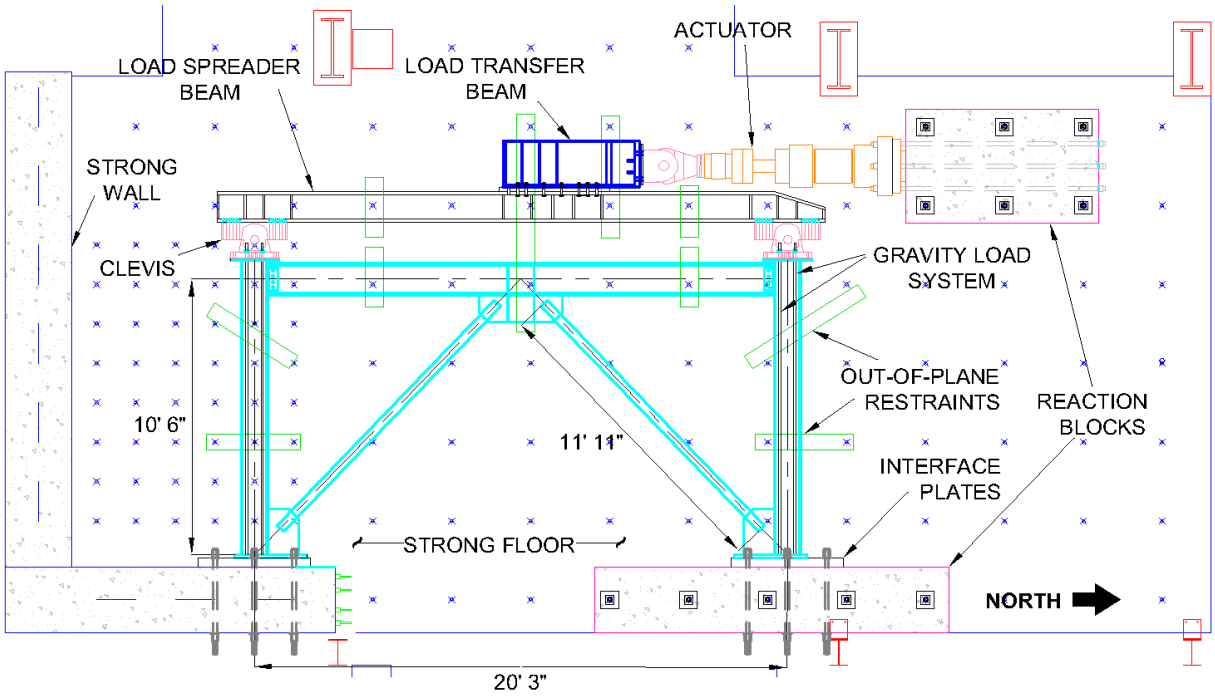

Figure 3.1: Experimental setup.

3.1.1 Frame Positioning

The UW SRL has a 30-inch-thick prestressed concrete strong wall with embedded conduits placed in an 18-inch grid. The strong floor is also prestressed concrete, with embedded conduits placed in an 18-inch grid in the area bounded by the strong wall and a 3-foot grid in all other areas. The holes in the strong floor have threaded anchors with a capacity of 200 kips embedded at the base of the hole that are used to fasten components to the floor. The limited length and height of the strong wall necessitated testing the frames in a horizontal position rather than upright. Measures were taken to ensure the frame experienced realistic conditions even though it was in a horizontal position. For example, column gravity loads were simulated using a post-tensioning system, and although the beam did not have a composite slab, out-of-plane bracing was provided at several locations to ensure its stability. Such setup design features will be discussed later in this chapter.

In order to make the frame as large as possible and to leverage the strong wall as a support, the frame was oriented in a north-south direction, with the south column anchored to the strong wall and the north column anchored to a newly constructed concrete reaction block. The centerline of the plane of the frames was set at 27 inches above the floor because it was directly in between the first and second rows of conduits in the strong wall. This was the most efficient position for attaching the column to the strong wall and allowed room for downward out-of-plane buckling of the braces.

The new reaction block, shown in Figure 3.2, is the same width as the strong wall and is secured to the strong floor with 5 2-inch diameter threaded rods each tensioned to 200 kips. A layer of Hydrostone was placed under the entire block and on top of the block underneath the rod bearing plates to ensure proper bearing surface area. Embedded conduits are placed in an 18-inch grid, offset 9 inches from the strong floor and strong wall grid because those spots were occupied by the threaded rods used to clamp the block to the strong floor. The conduits were designed to mimic those in the strong wall so that the connections between the columns and the reaction components would be consistent. A detailed drawing of the block and its reinforcing steel is in Appendix 1.

Figure 3.2: Reaction block used for N column anchorage.

Figure 3.3: Hydraulic actuator and reaction block.

3.1.2 Lateral Loading System

A hydraulic actuator, shown in Figure 3.3, was used to apply the lateral force and displacement history to the specimens. The actuator, part of the lab inventory, had a stroke of ± 10 inches and a capacity of 450 kips in tension and 550 kips in compression. Another reinforced concrete reaction block was constructed to provide anchorage for the actuator, as shown in Figure 3.4. This block was anchored to the strong floor

in the same way as the other reaction block, with 6 threaded rods instead of 5. The rods we tensioned to 200 kips each. The actuator was stressed to the block with 6 1-1/8 inch B-7 threaded rods. A 2-inch thick cotton duck elastomeric bearing pad was placed in between the actuator and the block, as shown in Figure 3.4, to allow for slight rotation of the actuator relative to the block.

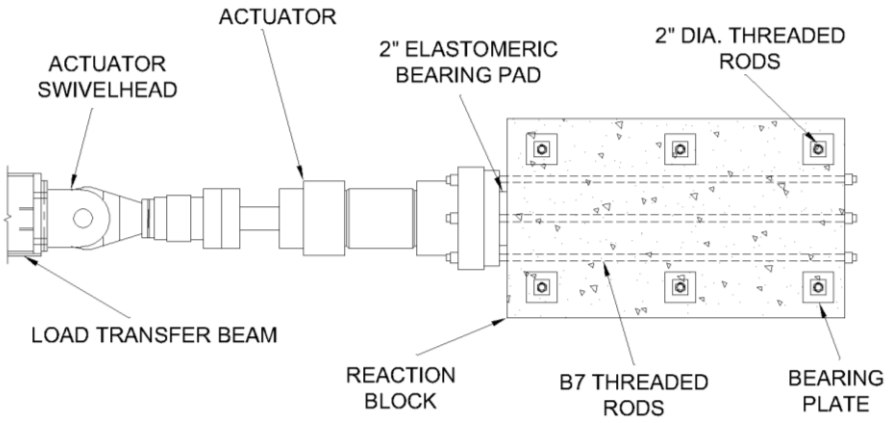

Figure 3.4: Actuator and reaction block assembly.

Because the focus of this experimental research program is to study the performance of a yielding chevron beam, the actuator could not be attached directly to the chevron beam, because the deflections would complicate force transfer. The load was delivered through the tops of the columns. In order to distribute load from the actuator to the tops of the columns, a load spreader beam was designed, as shown in Figure 3.5. The spreader beam was loaded near the midpoint of the beam to ensure approximately symmetric distribution of load to the frame. A W12x152 section was chosen for the spreader beam rather than a deeper, lighter section in attempt to maximize the specimen story height.

A pair of existing clevises was utilized to achieve the transfer of lateral load from the spreader beam to the top of the columns while ensuring no moment transfer occurred. The clevises, shown in Figure 3.6, were designed by Winkley (2009) for another research project and had adequate capacity for these tests. These large clevises added considerable depth to the loading apparatus, taking away some space for the specimen, but were used because they were readily available and meant new pins did not need to be fabricated.

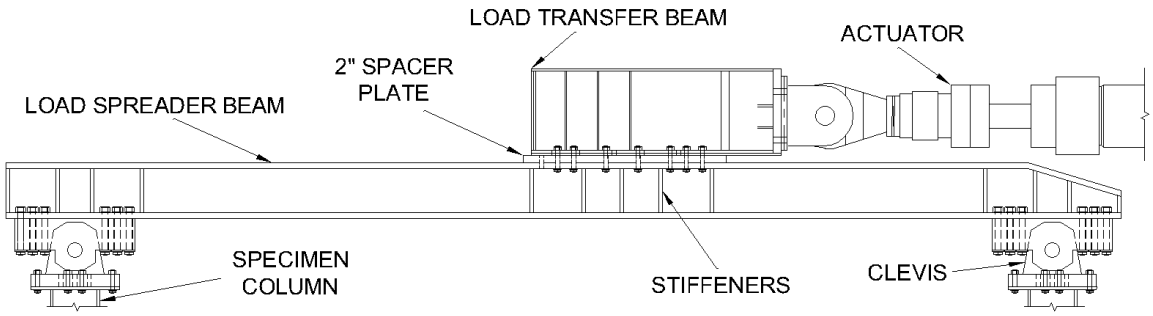

Figure 3.5: Loading apparatus.

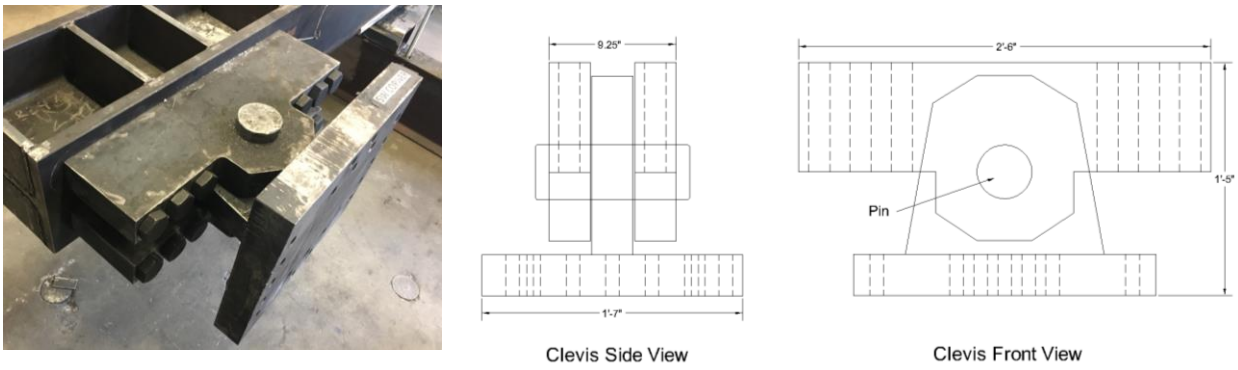

Figure 3.6. Clevis (a) photo and (b) drawings.

An existing load transfer beam, shown in Figure 3.5, was employed to carry load from the actuator to the spreader beam. The transfer beam, designed by Johnson (2005) for a series of braced frame tests, was connected to the actuator with 4 1-inch diameter A490 bolts. The transfer beam was connected to the spreader beam with 14 1-inch diameter high strength bolts, which were fully tensioned to create a slip-critical connection. Each clevis is connected to the load beam with 12 1-1/2 inch diameter bolts as shown in Figure 3.6.

3.1.3 Preliminary Frame Design

After the general layout of the frame within the lab and the loading method were determined, some preliminary decisions about the specimens could be made. The reaction block for the actuator was placed as far west as possible on the strong floor to maximize the height of specimen. The position of the actuator and depth of the load transfer beam, load spreader beam, and clevises left around 11-1/2 feet between the bottom of the clevis and the column anchorage points. Therefore the beam centerline was approximately 10-1/2 feet above the base of the frame. In order to create realistic proportions for the frame, the column spacing was set at 20 feet on center. This resulted in a brace angle of roughly 45 degrees, which was considered to be geometry similar to that found in a typical building. The 20 foot column spacing was consistent with the dimensions of the actuator and the desire to load the spreader beam as close to the center as possible. The spreader beam would have limit movement of the actuator itself if it was too long, and wider column spacing would require a longer spreader beam. Even with 20 foot column spacing, the spreader beam had to be modified to accommodate movement of the actuator. The corner of the spreader beam nearest the actuator was beveled and a 2” spacer plate between the spreader beam and the actuator was added, as shown in Figure 3.5.

Due of the position of the conduits in the strong wall and reaction block, the final spacing of the columns was 20’ 3”. After the story height and column spacing were established, the brace length and angle were determined. In building design, the braces would be selected based on the design lateral force calculated from a seismic analysis, but for these tests the braces were selected based on the capacity of the actuator that was used to load the frame. The braces were sized so that the expected maximum lateral resistance of the frame due to brace forces, plus an additional 30% contribution from the columns, did not exceed 75% of the capacity of the actuator. Square HSS braces were selected because they are commonly used for braces in chevron SCBFs. An HSS4x4x5/16 section was chosen because it met the limit on resistance and met the seismic compactness criteria required by the AISC Seismic Provisions (AISC 2010a). The resulting chevron frame is representative of what might be found in a 2 to 3 story building. The W12x50 columns were sized based on typical gravity loads for a 2 to 3 story office building and the capacity design requirements of the AISC Seismic Provisions. The columns sustain some additional axial forces due to overturning of the test frame due to the difference between the actuator location and mid height of the specimen beam.

3.1.4 Column Anchorage

An anchorage system was designed to connect the columns to the reaction block and strong wall. It was decided that the columns would be restrained at the base to avoid uplift of the columns and to simulate boundary conditions for the lower story of a braced frame. A column base plate and an interface plate to connect the base plate to the concrete block and wall were designed in tandem; Figure 3.7 and 3.8 shows photos of these components and detailed drawings are in Appendix 1. The interface plate was needed because the only means of attaching components to the strong wall and reaction block is through the conduits which are spaced 18 inches apart, and the thick interface plate transfers reactions from the smaller base plate to the reaction block and strong wall. The interface plate was connected to the reaction block and strong wall via the embedded conduits, and it had threaded holes in an efficient layout to attach the column base plate. The interface plates were reused but the columns and base plates were replaced for each test.

Figure 3.7: Interface plate attached to strong wall.

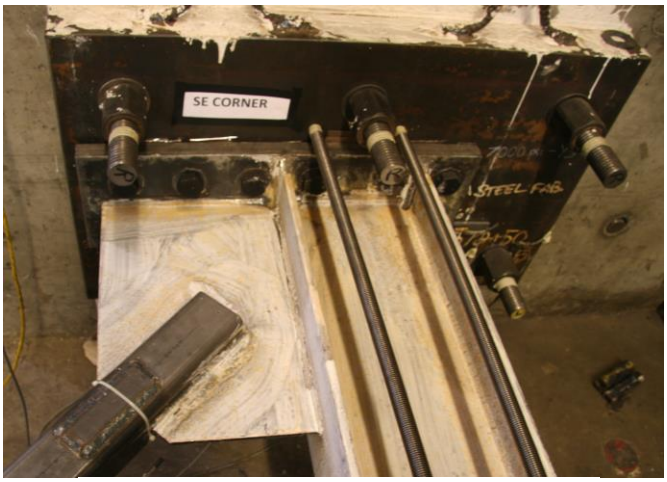

Figure 3.8: Base plate attached to interface plate.

The plates were designed to develop the full plastic capacity of the column plus additional axial forces from overturning of the frame. A finite element model of the column stub, corner gusset plate, base plate, and interface plate was created in SAP2000. Figure 3.9 shows the mesh and geometry of the model and 3.10 shows an example of output from the model. The column's expected plastic capacity ($R_yF_yZ_x$) was applied to the top of the column stub as an axial couple in the flanges, and a tensile force was applied to the entire section for overturning. The brace's expected tensile capacity was applied to the end of the brace stub. The bolts were modeled as a series of tension-only springs between the base plate and the interface plate. The bottom surface of the base plate was connected to the interface plate by springs that only transferred shear and compression. The base plate thickness was optimized so that the maximum stress on the face of the plate did not exceed 50 ksi. A 1.5 inch thick A572 Grade 50 base plate was chosen, shown in Figure 3.11. Bolt forces were determined from the force resultants on the tension-only springs; 1-1/4 inch diameter Grade 8 tap bolts were selected to develop the required forces.

.

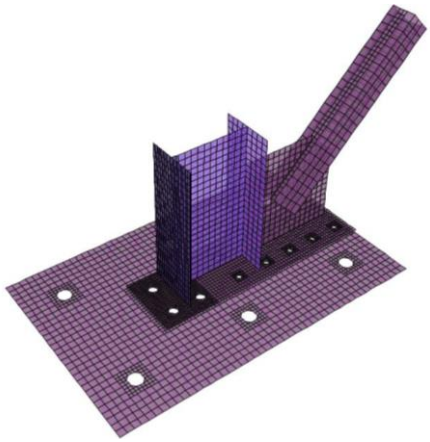

Figure 3.9. Overview of SAP2000 model.

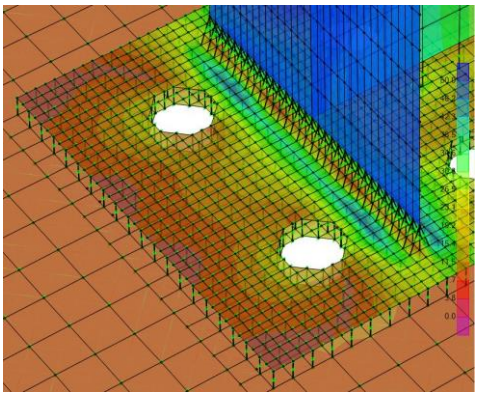

Figure 3.10. Von Mises Stress on face of baseplate.

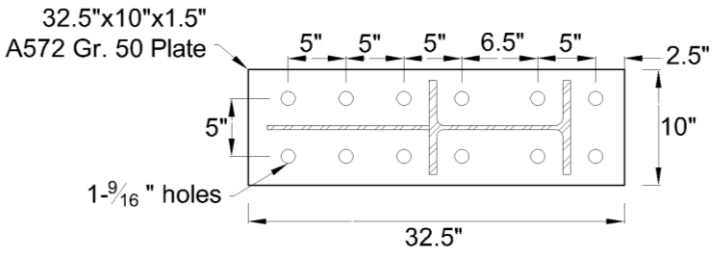

Figure 3.11: Base plate detail.

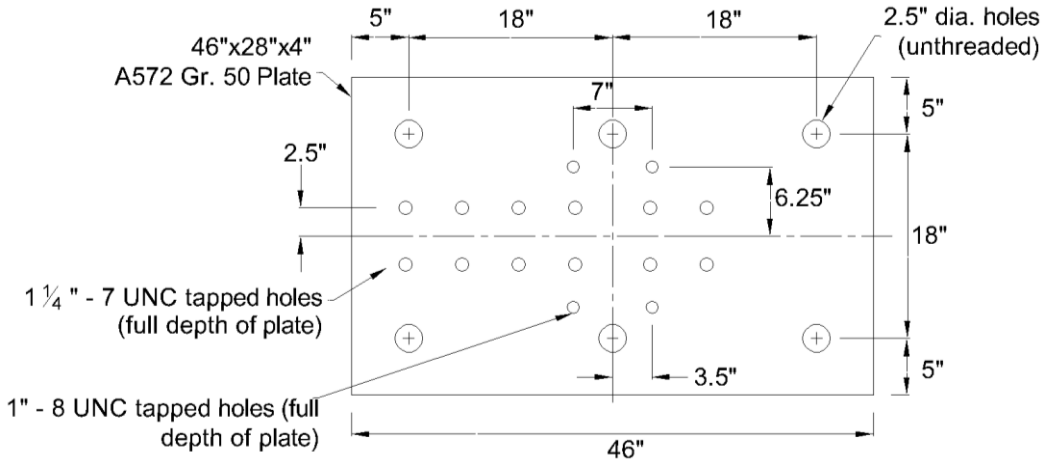

Figure 3.12. Interface plate detail.

The SAP2000 analysis indicated that the interface plate only needed to be 2 inches thick to develop the required forces without yielding the steel. However there was concern that the threaded holes would not be able to fully develop the tensile capacity of the high strength bolts because the plate was made from a weaker steel than the bolts. In order to avoid permanent deformation of the threads in the interface plate, the necessary hole depth to fully develop the tensile capacity of the bolts was calculated assuming a failure mode of shear rupture of the threads in the interface plate. The necessary shear area to prevent thread fracture for the tensile capacity of the bolt was correlated with a required hole depth of just over 3 inches, so a 4 inch thick interface plate was selected. Tapped holes were also provided for the column post-tensioning system, discussed in the following section. The interface plates were connected to the reaction block and strong wall with 6 2-inch diameter threaded rods, each tensioned to 150 kips. A thin layer of Hydrostone was placed between the interface plates and the concrete in order to provide a uniform bearing surface. The interface plates and base plates used some of the available height for the specimen, so the final column height was 11’ 2”.

3.1.5 Column Gravity Load System

In order to simulate a gravity load, a post-tensioning system was designed to apply a compressive stress on the columns. The post-tension system utilized threaded rods that ran from the bottom plate of the clevis to the interface plate, as shown in Figure 3.13. Existing holes in the clevis were designed to accommodate 1 inch diameter bolts, so 1 inch threaded rods were used for the post-tension system. The rods were threaded into 1 inch diameter tapped holes in the interface plate. In order to get the desired axial load, 4 threaded rods were required per column – two running above the column and two running underneath the column. Each rod was tensioned to 40 kips for a total axial load of 160 kips per column. This resulted in a compressive stress in the column of approximately 11 ksi.

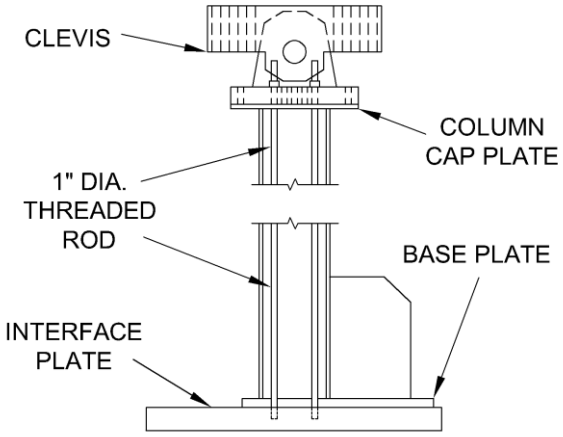

Figure 3.13: Column post-tensioning system.

3.1.6 Out-of-Plane Restraint

The specimen columns and beam, as well as the load transfer beam and load spreader beam, were restrained from moving out-of-plane to control out-of-plane lateral torsional buckling and to facilitate delivery of load to the frame and prevent damage to the hydraulic actuator. Out-of-plane bracing was provided at numerous locations, as shown in Figure 3.14. The bracing also provided support to the frame during erection. Out-of-plane restraint of the beam was provided at spacing no greater than L_p for the beam sections used. The beam was braced at mid-span and at the quarter points of the beam in each test.

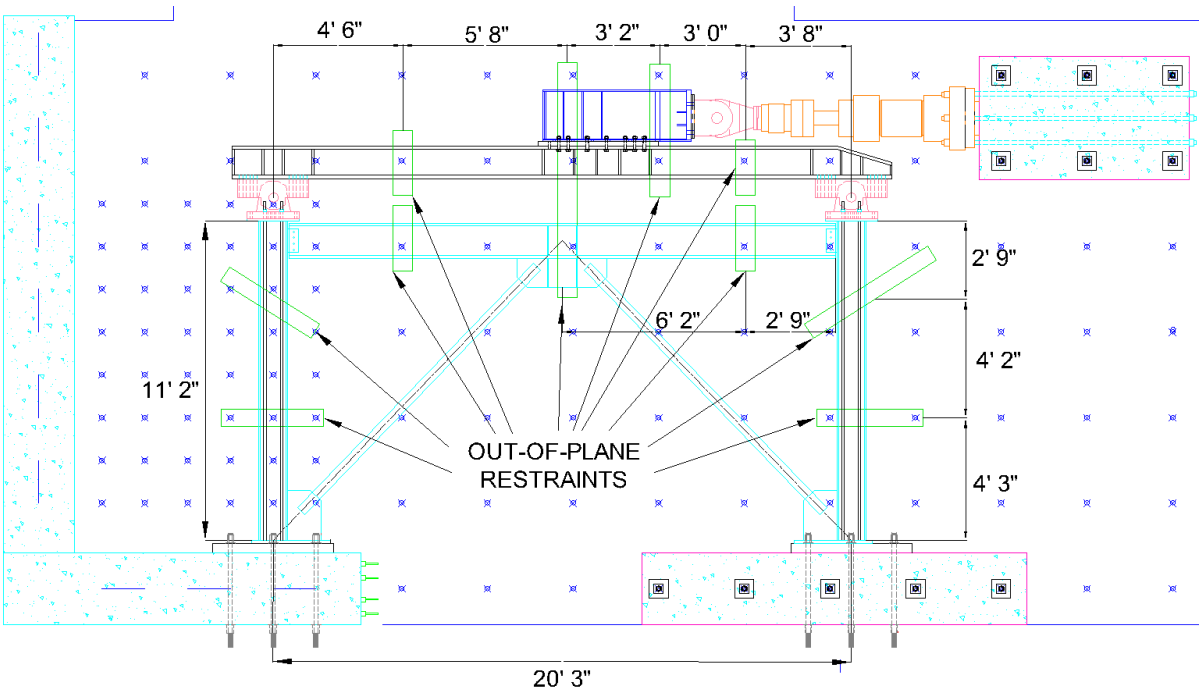

Figure 3.14. Out-of-plane restraint layout.

The out-of-plane restraint was provided by "sandwiching" the elements between steel sections that were anchored to the strong floor, as shown in Figure 3.15 and 3.16. This meant the location of the out-of-plane restraints was constrained by the location of anchorage points in the strong floor. The lateral supports were designed so that they did not impede movement in-plane. Teflon "sleeves" were placed on the flanges of the members, which bore on stainless steel sheets which were welded to the out-of-plane restraint and covered with a layer of lubricant to ensure frictionless sliding.

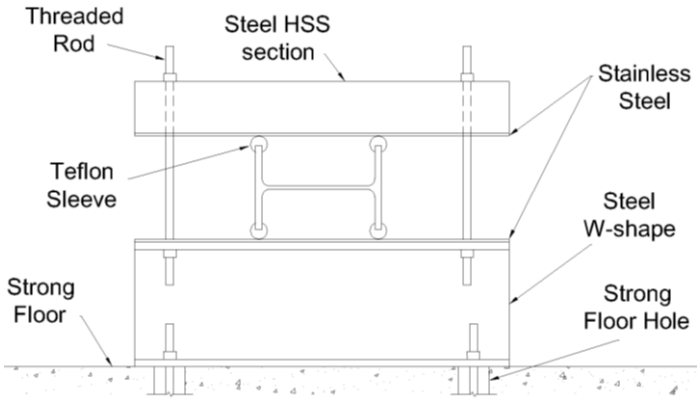

Figure 3.15: Out-of-plane restraint diagram.

Figure 3.16: Installed out-of-plane restraints.

3.2 Specimen Design

3.2.1 Overview

Three specimens with the general form seen in Figure 3.17 were tested in the UW SRL. The specimen dimensions, brace size, and column size were determined as described in Section 3.1.3. The chevron beam and the connections were designed using AISC 360-10 LRFD and the seismic capacity design methods of AISC 341-10.

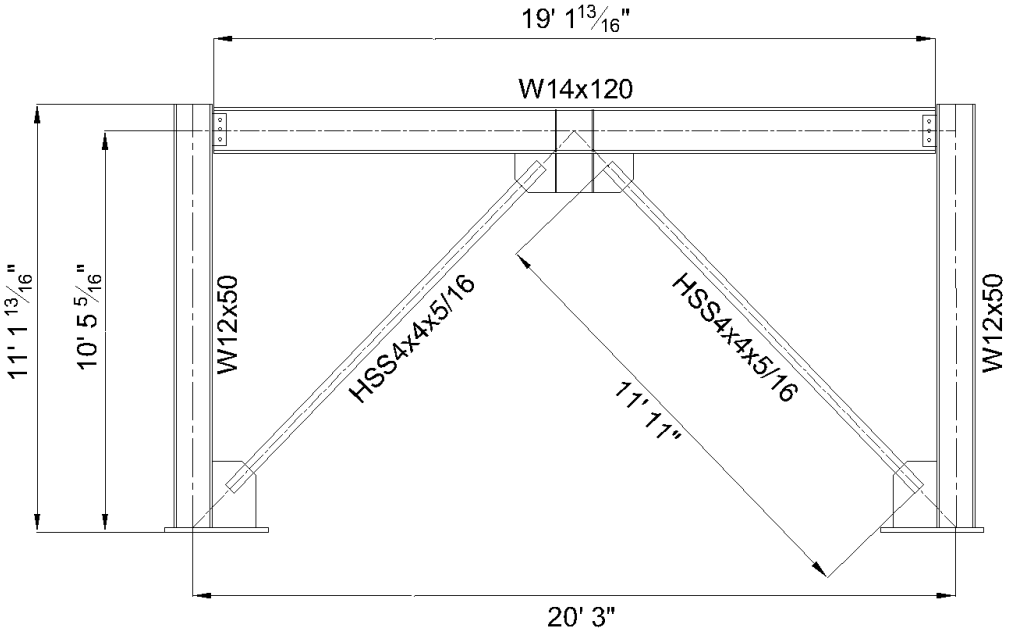

Figure 3.17: Typical specimen (Chevron 1).

Table 3.1 Specimen Design Summary

Specimen Name		**Chevron 1**	**Chevron 2**	**Chevron 3**
Column Size		W12x50	W12x50	W12x50
Brace Size		HSS4x4x5/16	HSS4x4x5/16	HSS4x4x5/16
Beam Size		W14x120	W14x61	W14x38
Beam DCR	**Axial**	0.07	0.13	0.24
	Flexural	0.79	1.65	2.73
	Interaction	**0.83**	**1.71**	**2.66**

Table 3.1 summarizes the final design of the test specimens. The first specimen (Chevron 1) was designed to satisfy all current code provisions, in particular that the beam was able to resist the unbalanced load that results from the difference between the post-buckling and tensile yield strength of the braces in a chevron frame. The second and third specimens were designed with beams that provide a reduced resistance for this unbalanced load. The second specimen (Chevron 2) was designed to have a beam demand-to-capacity ratio (DCR) for the combined axial and flexural demands of the unbalanced load of approximately 2, while the third specimen (Chevron 3) was designed to have a beam DCR of approximately 3. Computation of the beam DCR is discussed in Section 3.2.3.

In order to isolate the effect of beam size on chevron frame performance, all other braced frame details remain the same for all specimens. Specifically, the frame geometry, column section, brace section, and connection details are identical in each of the specimens. To maintain the same geometry it was necessary to use beams of similar depth (i.e. all W14) for all specimens because the constraints of the test setup required the brace length and angle to change with changing beam depth. Such changes in geometry make it difficult to compare the test results. W14 beams were chosen for all the specimens to accommodate all expected beam DCRs.

The specimen beam and connections were designed assuming A500 HSS4x4x5/16 braces, which were sized based on the actuator capacity. However, A1085 braces were used for the test specimens instead of A500. A500 steel has a yield strength of 50 ksi an R_y value of 1.4, where R_y is the ratio of the expected yield stress to the specified minimum yield stress. A1085 has a yield stress of 50 ksi and an R_y value of 1.25 – thus the expected strength, R_yF_y, of the braces changed from 70 ksi to 62.5 ksi. Because the frame was designed for the expected capacity of A500 braces, some aspects of the final design are slightly more conservative than originally intended.

3.2.2 Design Provisions for SCBFs

Chevron SCBFs are designed to adhere to the requirements in the 2010 AISC Seismic Provisions (AISC 2010a). All equations presented in this section are from the AISC Seismic Provisions unless otherwise specified.

General SCBF Requirements

Capacity design limits inelastic behavior to a specified ductile element in order to avoid undesirable failure modes. The braces are the ductile elements in SCBFs, and all other components of the frame are designed to develop the strength and deformation capacity of the braces from the limit states of tensile yielding and compressive buckling. The beams, columns, and connections in SCBFs are all designed for the larger of the forces determined from two scenarios:

(i) All braces assumed to resist forces corresponding to their expected strength in tension or compression

(ii) All braces in tension assumed to resist their expected strength while the braces in compression are assumed to resist their expected post-buckling strength

The expected brace strength in tension is $R_yF_yA_g$ and the expected brace strength in compression is $1.14F_{cre}A_g$. F_{cre} is determined using the equations for F_{cr} in the AISC Specification for Structural Steel Buildings (AISC 2010b), with R_yF_y used in lieu of F_y. The expected post-buckling strength is taken as a maximum of 0.3 times the expected compressive strength of the brace to account for compressive strength degradation after buckling.

Chevron System Requirements

Beams that are intersected by braces away from beam-to-column connections are subject to additional requirements:

(i) Beams shall be continuous between columns.

(ii) Beams shall be braced to satisfy the requirements for moderately ductile members. Lateral bracing is required at the point of intersection unless the beam has sufficient out-of-plane strength and stiffness to ensure stability between adjacent brace points.

Member Requirements

Local buckling can lead to deteriorating resistance and deformation capacity under earthquake loading, so the Seismic Provisions have more stringent local slenderness limits than the AISC Specification. The columns and braces in SCBFs must meet compactness criteria for "highly ductile members" per table D1.1 of the Seismic Provisions. Beams must meet the requirements for "moderately ductile members".

For HSS sections, the highly ductile criterion is defined by the width-to-thickness ratio of the walls of the tube:

$$b/t \leq 0.64\sqrt{E/F_y}$$

For W shapes, these ductility criteria are defined by the width-to-thickness ratio of both the flanges and the web. For the flanges of W shapes the $b/_{2t}$ ratio is limited to:

$$0.38\sqrt{E/F_y} \quad \text{for moderately ductile members.}$$

$$0.30\sqrt{E/F_y} \quad \text{for highly ductile members.}$$

For the webs of W shapes, the local slenderness limit changes based on the axial demand-to-capacity ratio, $C_a = P_u/\phi P_y$. For members with low axial load ($C_a \leq 0.125$), the $h/_{t_w}$ ratio is limited by:

$$3.76\sqrt{E/F_y}\,(1\text{-}2.75C_a) \text{ for moderately ductile members.}$$

$$2.45\sqrt{E/F_y}\,(1\text{-}0.93C_a) \text{ for highly ductile members.}$$

For members with relatively high axial load, ($C_a > 0.125$), the $h/_{t_w}$ ratio is limited by:

$$1.12\sqrt{E/F_y}\,(2.33\text{-}C_a) \quad \text{for moderately ductile members.}$$

$$0.77\sqrt{E/F_y}\,(2.93\text{-}C_a) \text{ for highly ductile members.}$$

3.2.3 Beam Design

In chevron SCBFs, the demand considering the post-buckling capacity of one brace with the expected tensile capacity of the other brace almost always controls the beam design. In either case, the fact that the compressive brace provides less resistance than the tensile brace results in a net downward force at the center of the beam. However, the post-buckling capacity results in a much larger downward force and thus higher flexural demand on the beam, as illustrated in Figure 3.18, where φ is the brace angle relative to horizontal.

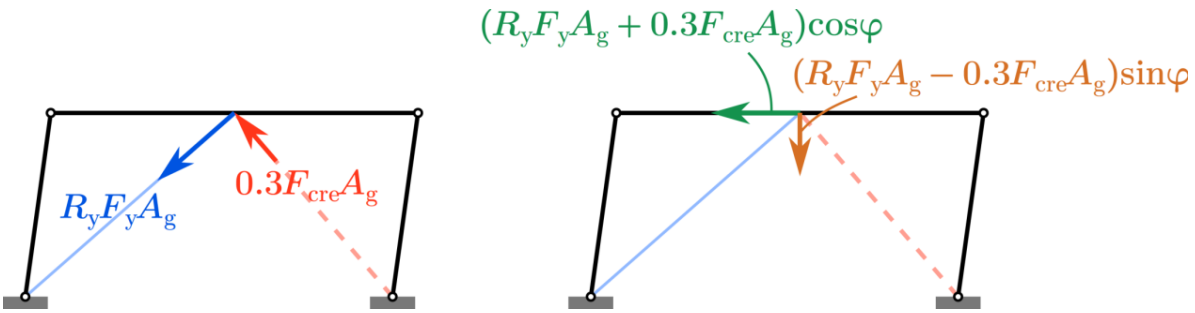

Figure 3.18: Demand on beam from post-buckling braces.

The net axial load on the beam is lower in the post-buckling configuration than when both braces are at their expected capacity, but because the axial component of the axial-flexural interaction equation is typically much lower than the flexural component the post-buckling case typically controls. The axial-flexural interaction equation used for the design of the beam is Equation H1-1 in the AISC Specification (AISC 2010b):

(a) When $\frac{P_r}{P_c} \geq 0.2$

$$\frac{P_r}{P_c} + \frac{8}{9}\left(\frac{M_r}{M_c}\right) \leq 1.0$$

(b) When $\frac{P_r}{P_c} < 0.2$

$$\frac{P_r}{2P_c} + \frac{M_r}{M_c} \leq 1.0$$

P_r and M_r are the compressive and flexural demand on the beam, respectively. P_r is taken as half of the net horizontal load from the braces as shown in the free body diagram in Figure 3.19. The maximum moment demand in the beam occurs at the center; however that region is significantly stiffer and stronger than the rest of the beam due to the presence of the mid-span gusset plate. When the mid-span gusset plate and stiffeners are welded to the beam, the new combined section is much deeper than the beam itself, which

increases the moment of inertia and plastic moment capacity significantly. As a result, plastic hinging will typically occur at the edges of the mid-span gusset plate where the moment of inertia abruptly changes rather than the center of the beam where the moment demand and capacity are the highest. Thus the design moment, M_r, is taken as the moment at the edge of the gusset plate.

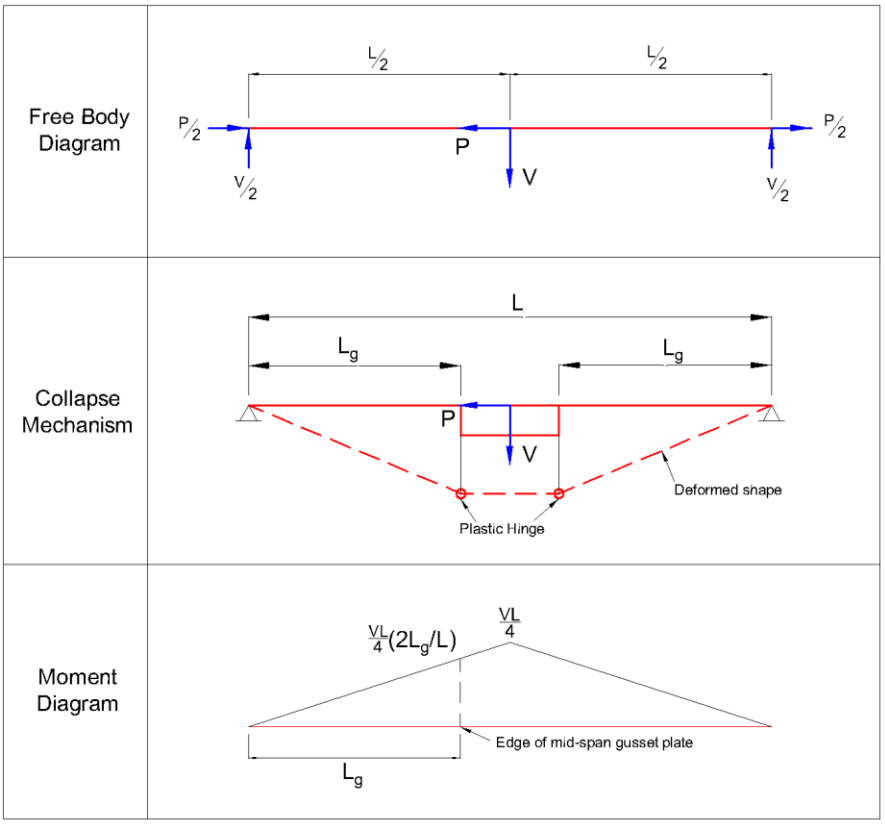

Figure 3.19: Assumed beam free body, collapse mechanism, and moment diagrams.

P_c and M_c are the factored capacity of the beam in compression and flexure, respectively, calculated according to the AISC *Specification*. Selected beams met slenderness requirements for moderately ductile members and lateral bracing was provided to resist flexural and lateral-torsional buckling, so the beams were expected to be able to develop their full plastic capacity in flexure. The lateral bracing spacing was also used as the unbraced length for calculating the compressive strength of the beams.

Table 3.1 shows the results of the beam design for the three test specimens. The flexural DCR is defined as the ratio of the beam flexural demand to the beam available flexural capacity, $M_r/\phi M_n$, and the axial DCR is defines as the ratio of the beam compressive demand to the beam available compressive capacity, $P_r/\phi P_{cr}$. The combined DCR is the result of the axial-flexural interaction equation described above. Detailed calculations for the beam design can be found in Appendix 1. The first test specimen was designed to meet current code requirements and thus has a combined DCR less than 1. The second and third specimens were designed to test the effect of a beam yielding mechanism on the performance of the frame and thus have DCRs greater than 1.

3.2.4 Connection Design

Gusset Plate Connections

The gusset plates were designed to develop the expected brace capacity and to accommodate the end rotation of the brace due to buckling. Both the corner and mid-span gusset plates were designed based on the Balanced Design Procedure (Roeder et al. 2011). This method has been shown to improve the seismic performance of SCBFs by balancing yielding of the brace with yielding of the gusset plate to increase the inelastic deformation capacity of the system. To accommodate brace end rotation it employs an elliptical clearance for corner gusset plates and a $6t_p$ vertical clearance for mid-span gussets, which results in more compact gusset plates. It uses a 3-4-5 triangle to calculate the Whitmore width since this has been shown to be conservative in past research (Yam 1994) and it encourages yielding of the gusset plate. In addition, it uses a relaxed block shear resistance factor since the AISC block shear requirement has been shown to be very conservative for concentrically applied load, since LRFD evaluation of concentrically loaded block shear failure data (Huns et al. 2002) results in a resistance factor greater than 1.0 for the current design equation.

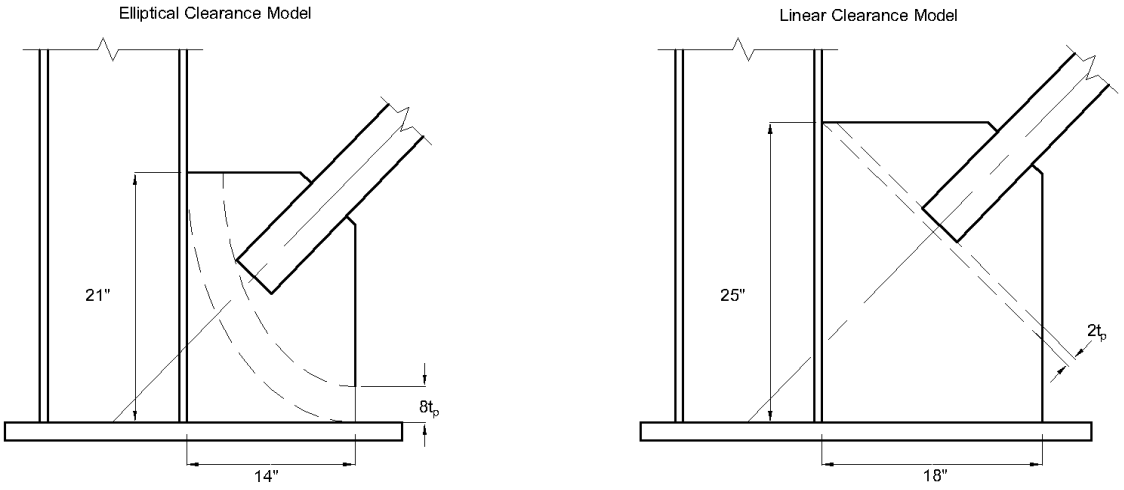

Figure 3.20: Gusset plate clearance model comparison.

The BDP encourages tensile yielding of the gusset plate as a secondary yield mechanism after brace yielding and buckling, so the design equations for the BDP result in thinner gusset plates than conventionally designed gusset plates. Conventionally designed gusset plates are not only thicker than those designed with the BDP but also larger because of the difference in clearance model, as shown in Figure 3.20.

The other major difference between conventionally designed plates and BDP designed plates is the interface welds between the gusset plate and the beam or column. Using the conventional design procedure, interface welds are designed to develop the brace tensile capacity with forces on the welds determined using the Uniform Force Method (UFM). The UFM is an equilibrium method that does not account for additional strain on the welds due to inelastic deformation of the gusset plate, and thus the demands on the weld are often under predicted. The BDP requires the interface plate welds to develop the yield capacity of the gusset plate because of the additional demands on the weld due to inelastic action caused by gusset plate rotation due to end rotation of the buckled brace.

Figures 3.21 and 3.22 show the final design of the mid-span and corner gusset plates, respectively. The gusset plate connections are identical in each of the 3 specimens since brace size and geometry does not change. Stiffeners were added to the center of the mid-span gusset and beam to stabilize the plate and beam against excess deformation while keeping the gusset plate thin to encourage tensile yielding (Lumpkin, 2009). The stiffeners are the same thickness as the gusset plate and are placed 12 inches apart to mimic the column flange spacing.

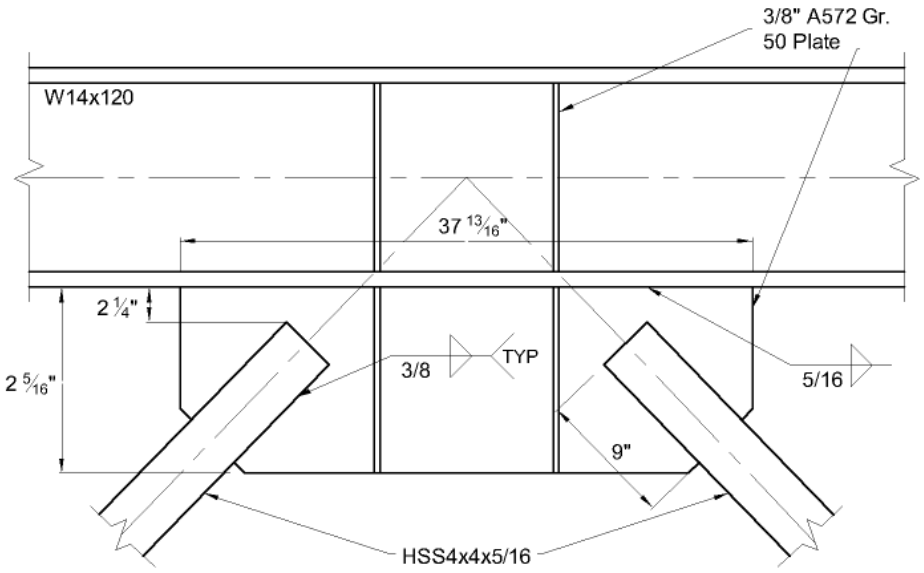

Figure 3.21: Mid-span gusset plate detail.

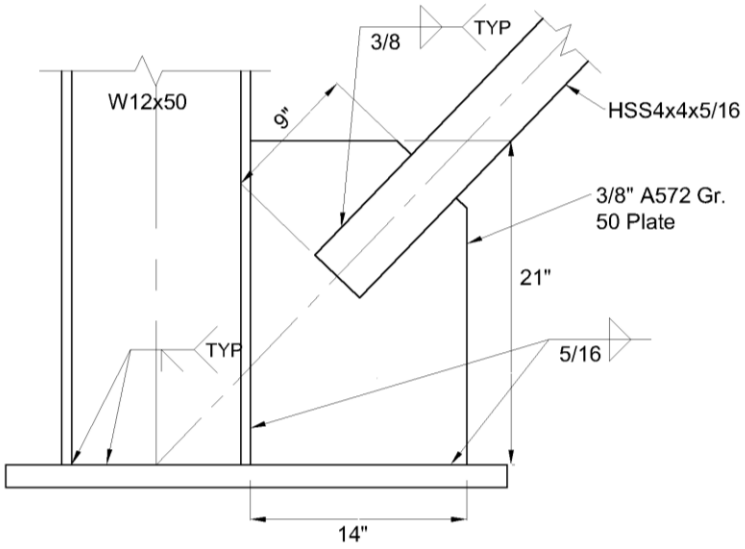

Figure 3.22: Corner gusset plate detail.

Beam-to-Column Connections

In each specimen the beam is connected to the columns via shear plate connections as shown in Figure 3.22. Shear connections were chosen over fully restrained connections because this is common in engineering practice. The shear plates were designed for the controlling shear and axial forces from the two analysis scenarios described in Section 3.2.2. The capacity is calculated according to the equations in Chapter J of the AISC Specification (2010b).

For the second and third specimens, the beam web was too thin for block shear due to the expected brace forces. A ¼" web doubler plate, shown in Figure 3.23, was added to ensure that block shear failure would not occur.

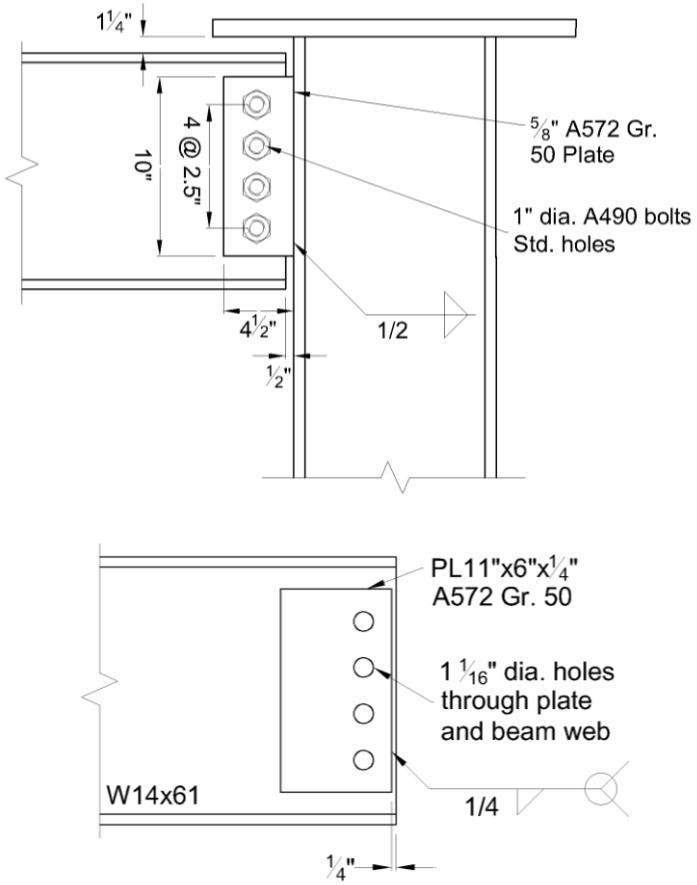

Figure 3.23. Shear tab (top) and beam web doubler plate (bottom) detail.

Column Web Doubler and Cap Plate

There was a ¾ inch cap plate welded to the top of each column and bolted to the bottom plate of each clevis to provide force transfer between the clevises and the tops of the columns, as shown in Figure 3.24. This allowed replacement of the specimen and reuse of the clevises in each test. The cap plate connection was designed to resist half of the maximum actuator capacity in order to ensure that there would be no damage to this critical connection.

The webs of the W12x50 columns used in the tests did not have adequate shear strength to transfer the expected load from the clevis to the beam and braces via the shear tab. A ½ inch thick web doubler plate, shown in Figure 3.24, was welded to the column in each of the specimens to enable full transfer of load to the test frame.

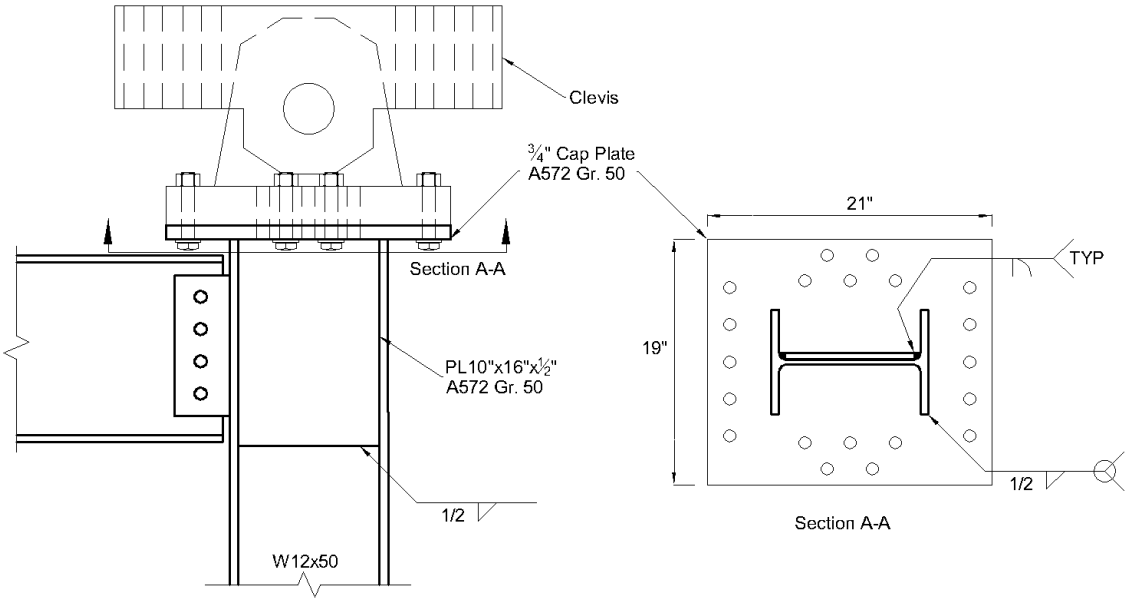

Figure 3.24: Column web doubler (left) and cap plate (right) detail.

3.2.5 Materials

The nominal material specification and overall dimensions for each component of the specimens are shown in Table 3.3. The measured material properties from tension coupon testing are shown in Table 3.4. Material tests were performed according to ASTM Standard Test Methods and Definitions for Mechanical Testing of Steel Products (ASTM A370).

Table 3.3 Material Specification and Dimensions

Component	Material	Size	Dimensions
Beam	A992 Gr. 50	W14x120 (Chevron 1) W14x61 (Chevron 2) W14x38 (Chevron 3)	19’ 1-5/16” long
Columns	A992 Gr. 50	W12x50	11’ 1-13/16” long
Braces	A1085 Gr. 50	HSS4x4x5/16	11’ 11” long
Gusset Plates	A572 Gr. 50	3/8” thick	37-13/16”x12-5/16” mid-span) 14”x21” (corner) 7-1/8”x12-5/16” (stiffeners)
Shear Tab	A572 Gr. 50	5/8” thick	10”x4-1/2”
Base Plate	A572 Gr. 50	1-1/2” thick	32”x10”
Cap Plate	A572 Gr. 50	3/4” thick	19”x21”
Doubler Plate	A572 Gr. 50	½” thick (column) ¼” thick (beam)	10”x16” (column) 11”x6” (beam)

Table 3.4 Material Properties from Coupon Testing

Component	Shape or plate thickness	Yield stress, $F_{y,meas}$ (ksi)	Ultimate stress, $F_{u,meas}$ (ksi)
Column	W12×50	52.4	65.9
Beam	W14×120	56.7	70.1
Beam	W14×61	58.5	74.3
Beam	W14×38	53.1	68.7
Brace	HSS4×4×5/16	62.5	74.8
Gusset PL	3/8”	75.3	85.0

3.2.6 Fabrication

All three specimens were fabricated and constructed by students in the UW SRL under the supervision of an experienced lab technician. All the welding was performed by Doug Lindblad, a professional welder certified in the FCAW process for all positions. The frames were constructed as follows:

- Cut all plates to size
- Cut beam, columns, and braces to length
- Weld doubler plates and shear plates onto columns
- Prepare weld access hole for column CJP welds to base plate (Fig. 3.25)
- Weld baseplates and corner gusset plates onto column
- Weld gusset plates, stiffeners, and doubler plates onto beam
- Cut slots in braces and weld net section reinforcement
- Assemble beam and columns into final position in the testing rig
- Drill holes in the beam web and bolt it to the shear plate
- Weld cap plate to the top of the column
- Bolt the cap plates and base plates to the testing rig
- Assemble braces into position and weld to gusset plates
- Install out-of-plane restraints
- Tension bolts and threaded rods

Figure 3.25: Completed weld access hole.

Each of the components was cut to a 1/16 inch tolerance. All cuts were made with an oxygen-acetylene torch except for the braces, which were cut with a horizontal bandsaw. For the single bevel CJP welds, the flanges were cut to a 45° angle with a 1/4 inch root opening. Backing bars were removed and the welds were then back gouged and reinforced with a fillet weld. Brace slots were cut 1/8 inch wider than the gusset plate thickness, which made it easier to slide the braces over the gusset plates after the frame was assembled. The slot was made by first drilling a hole at the top of the slot, and then flame cutting the slot from the hole to the end of the brace. The edges of the slots were then ground smooth. The bolts were tensioned with a hydraulic wrench, using direct-tension-indicator washers to verify that the correct pretension was achieved. The threaded rods were tensioned with a calibrated hydraulic cylinder jack.

3.3 Instrumentation

A variety of instruments were used to collect data on strain, load, displacement, and deformation of the specimens. The National Instruments software, LabVIEW, was used to collect data from the potentiometers and strain gauges, described in sections 3.3.2 and 3.3.3. The NDI FirstPrinciples software was used to collect data from Optotrak LED markers, described in Section 3.3.4. The instrumentation plan remained identical from specimen to specimen, except for the addition of potentiometers to measure column shortening after the first test, described in Section 3.3.2. The sections below describe the instrumentation by instrument type and discuss the key measurements and their role in determining frame response characteristics.

3.3.1 Actuator Load Cell and LVDT

The hydraulic actuator used to apply load to the frame had a load cell and LVDT installed internally. Channels 1 and 2 in the LabVIEW system were used to measure the actuator force and displacement from the load cell and LVDT, respectively. The actuator load cell reading was used to determine the total base shear for analysis of the frame.

3.3.2 Potentiometers

Two types of potentiometers were used to measure displacement of the specimen and various components of the testing rig. The UniMeasure P510 string potentiometers were used to measure displacements that were expected to be greater than 2 inches or that needed to be measured over a long distance, such as from the top of the column to the base plate. The BEI Duncan 600 Series linear conductive potentiometers were used to measure displacements less than 2 inches. Examples of these potentiometers are shown in Figure 3.26 and 3.27. All potentiometers were calibrated prior to the first test.

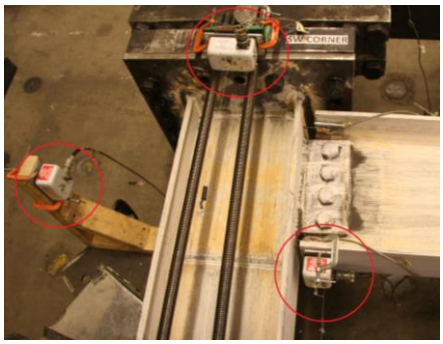

Figure 3.26: String potentiometers.

Figure 3.27: Duncan potentiometers.

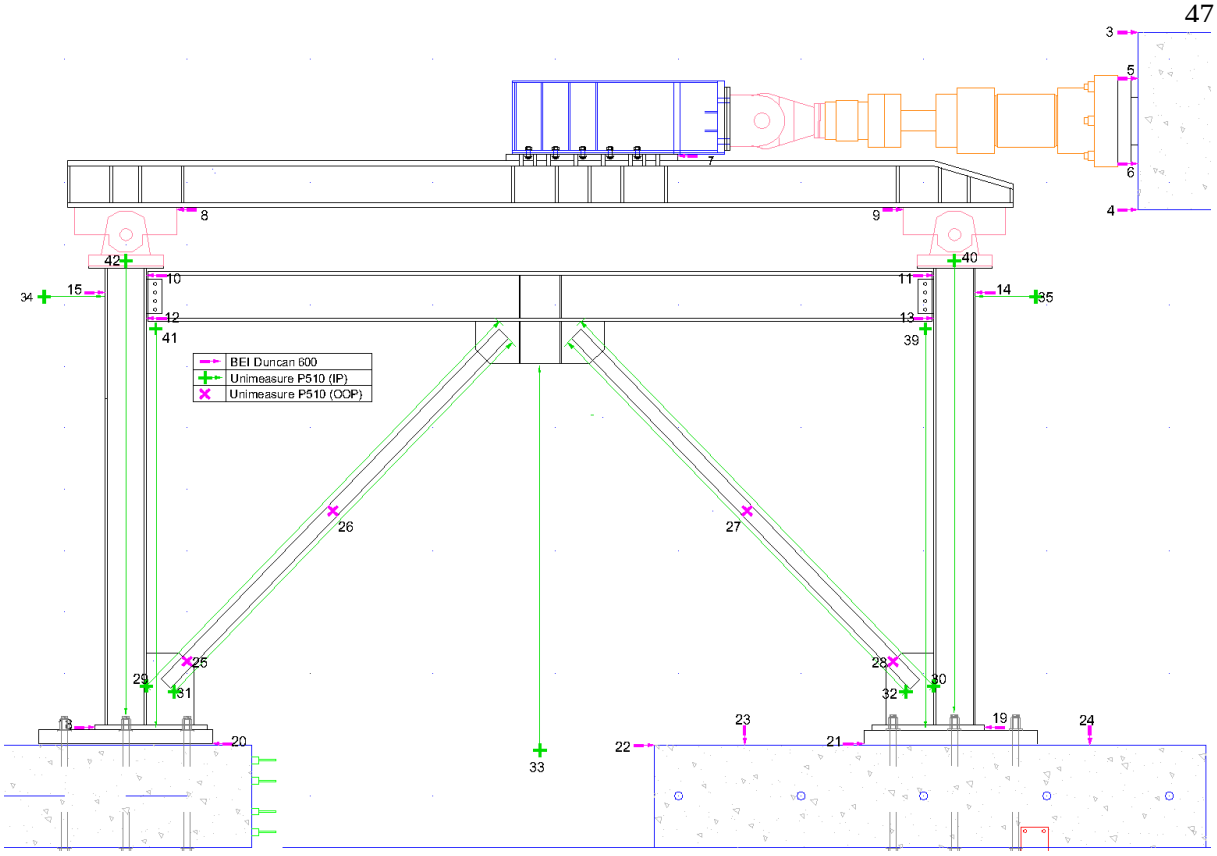

Figure 3.28: Potentiometer layout.

Lateral Drift Potentiometers

Potentiometers 34 and 35 were used to measure the lateral drift of the frame, and were attached to the outside of the columns at the beam centerline. These potentiometers were used in the application of the displacement protocol for the tests. The measurements from the two channels were averaged, and the actuator was moved until the test frame reached the target displacement based on the averaged displacement reading. These potentiometers were used to control displacement rather than the actuator LVDT because there is significant difference in the lateral movement of the frame and the actuator due to the difference in height above the fixed base and flexibility within the test setup.

Column Potentiometers

Potentiometers 40 and 42 were used to directly measure column shortening and elongation, and were added after the first test. During the Chevron 1 test, there was a loss of tension in the threaded rods used to simulate gravity load in the column, which indicated column shortening had likely occurred. In order to directly measure this phenomenon, potentiometers 40 and 42 were added for the remaining tests.

Beam Potentiometers

Potentiometers 39 and 41 measured the vertical displacement of the beam ends relative to the base of the specimen. These were also added after the first test in order to capture the effects of column shortening. These potentiometers were used to correct the beam deflection measurement from potentiometer 33. Potentiometer 33 measured the vertical deflection of the beam at mid span relative to a fixed point on the strong floor, so it included to downward movement of the beam due to column shortening. In order to find the beam deflection relative to its ends, the deflection from potentiometers 39 and 41 were subtracted from the beam deflection measurement from potentiometer 33. Potentiometers 10 through 13 were used to measure the rotation of the beam end relative to the column face.

Brace Potentiometers

Potentiometers 26 and 27 measured the out-of-plane displacement of the center of the brace. The potentiometers were attached to a heavy piece of steel sitting on the strong floor, so the top of the potentiometer was roughly 17 inches below the bottom face of the brace. In each of the tests the braces reached a maximum out-of-plane displacement of more than 17 inches, so these potentiometers were removed late in the test and were not used to measure the maximum brace out-of-plane deformation. Potentiometers 31 and 32 were used to measure the elongation and shortening of the brace and were attached to the ends of each brace. Potentiometers 29 and 30 measured the brace elongation but were attached to the beam and column flange in line with the brace in attempt to capture any additional elongation due to gusset plate yielding.

Gusset Plate Potentiometers

Potentiometers 25 and 28 were used to measure the out-of-plane displacement of the corner gusset plate at the center of the edge where the brace intersects it, shown in Figure 3.28.

Boundary Condition Potentiometers

Several of the BEI Duncan potentiometers were used to measure slip of the reaction blocks, clevises, load transfer beam, interface plates, and base plates, as well as rotation of the actuator relative to the reaction block it was anchored to.

3.3.3 Strain Gauges

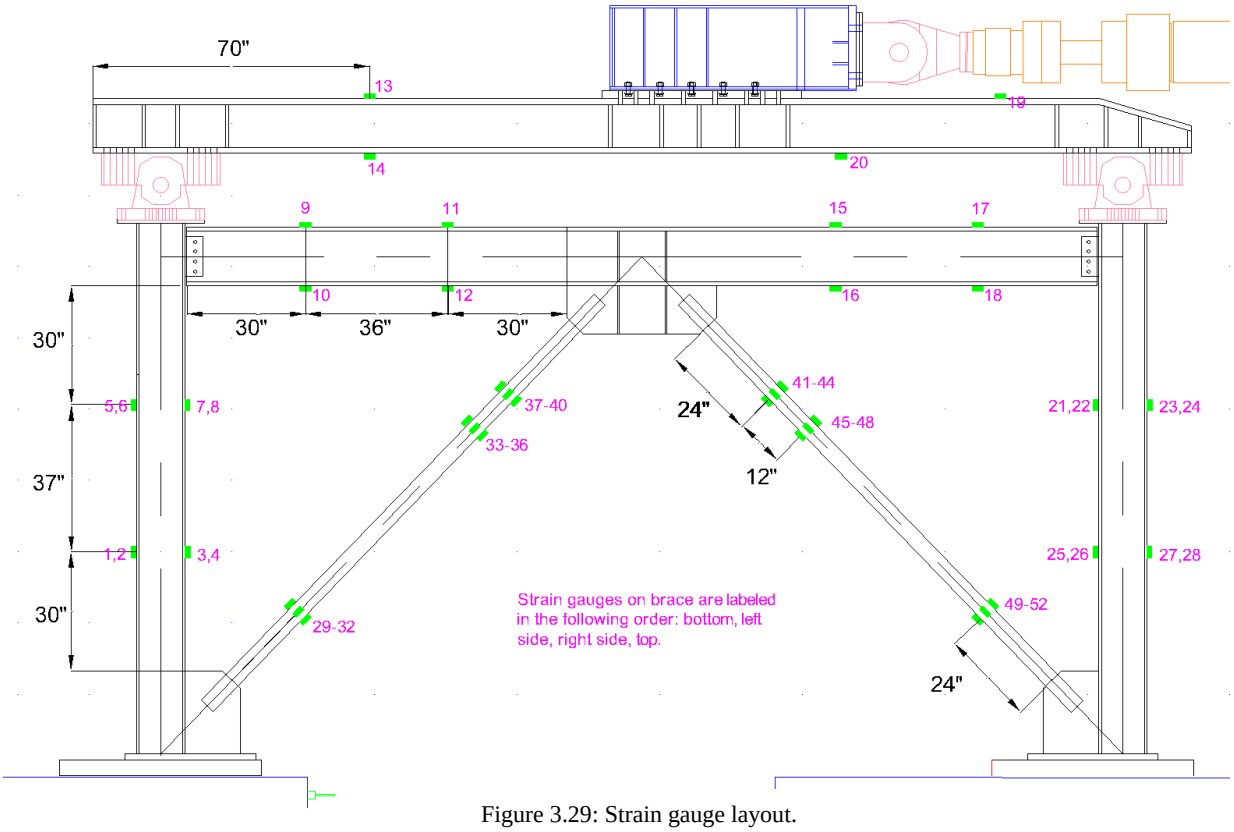

Figure 3.29: Strain gauge layout.

Strain gauges were used to capture strains at desired locations on the frame and load spreader beam. These strains were used to determine shear force, axial force, and moment on the frame elements throughout the test. The primary goal was to determine the relative contribution to base shear of the columns and braces, but the beam flexural demand was also of interest. Strain gauges were placed on the load spreader beam to help assess whether the load was distributed evenly to the columns or not. Figure 3.29 shows the positioning of the strain gauges used in each of the 3 specimens. Effort was made to place strain gauges away from yielding to ensure elastic behavior at the gauge locations.

The strain gauges on the columns were placed as far apart as possible while staying away from the corner gusset plate and shear tab connections where column yielding might occur. Placing the strain gauges far apart means there is a larger difference in strain due to flexure, which makes it easier to calculate the shear force in the columns. Strain gauges were placed in pairs to provide redundancy in case one strain gauge failed to work because column shear is an important measurement. The strain gauges on the beam were also placed as far apart as possible, while trying to avoid the gusset pate and shear tab connection regions where beam yielding might occur. The strain gauges on the brace were placed on all 4 sides of the

brace in order to capture the flexural demand on the brace due to buckling. The strain was measured at 3 locations along the brace to provide redundancy and to capture the change in flexural demand along the length of the brace.

Tokyo Sokki Kenkyujo Co., Ltd. FLA-6-11-SLT and YFLA-6-11-SLT 3-wire strain gauges were used on all the specimens. They were placed at the midpoint of the flanges or at the center of the face of the brace, along the longitudinal axis of the member. Because each test lasted over 8 hours, 3-wire gauges were used to compensate for temperature fluctuation throughout the test.

3.3.5 OptoTrak

In order to more accurately capture the absolute and relative deformation of the beam mid-span connection region, the Northern Digital Inc. (NDI) OptoTrak system was utilized. This system uses sophisticated cameras to collect high resolution 3D displacement measurements of LED targets placed on the specimen. The accuracy of this system is within a few tenths of a millimeter, so it can be used to capture a wide range of behavior. The data gathered from the OptoTrak system was primarily used to measure brace out-of-plane displacement, beam vertical and out of plane displacement, and gusset plate out of plane displacement. There were 79 LEDs placed on each specimen, as shown in Figure 3.31. The LEDs were placed in the same locations for all of the specimens.

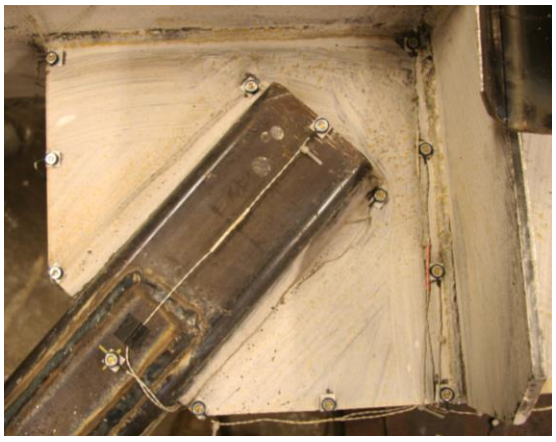

Figure 3.30: Optotrak LEDs on midspan gusset.

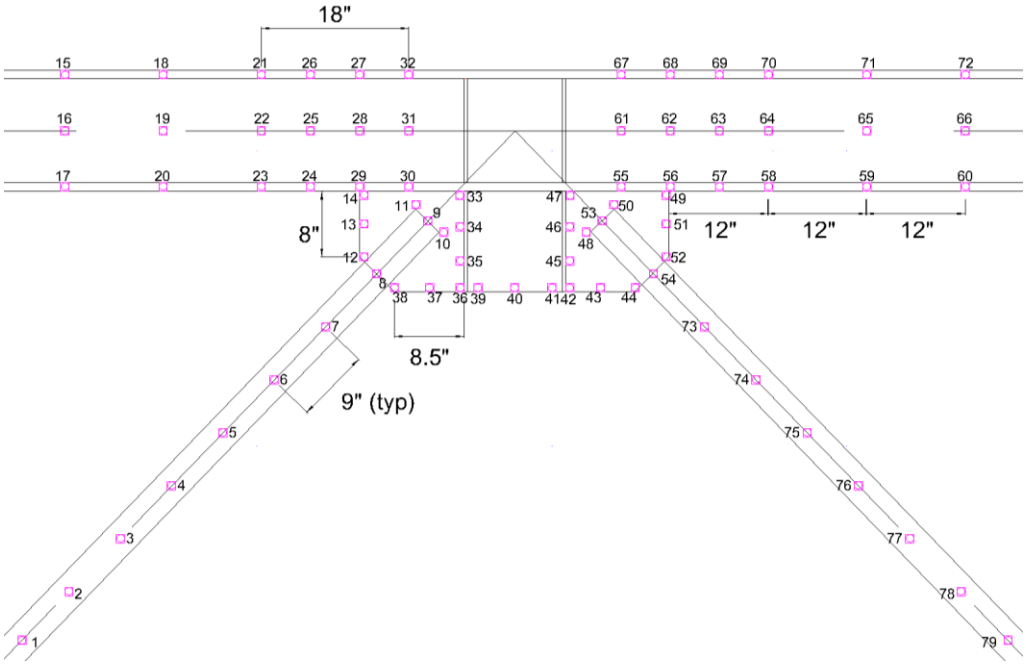

Figure 3.31: Optotrak LED layout.

3.3.6 Whitewashing

The connection regions of the specimen were painted with a thin layer of Hydrostone in order to make yield lines visible. When hot-rolled steel yields, mill scale on the surface of the member flakes off. This allows locations where yielding has occurred to be visually identified. Places where yielding was expected were whitewashed, except for on the braces which are cold rolled and thus do not have mill scale. Figure 3.32 shows a whitewashed specimen and a close up of yielding at the base of one of the columns during a test.

Figure 3.32: Whitewash on completed specimen (top) and yield lines at column base (bottom).

3.4 Testing Procedure

3.4.1 Pre-Test Preparation

After the specimens were fully assembled, strain gauges were applied and connected to the data acquisition system. The specimen was then whitewashed as described in Section 3.3.6, followed by installation of the potentiometers. The bases of the string potentiometers were clamped to the desired location on the specimen, and the end of the string was glued to a magnet which was in turn glued to the specimen. The Duncan potentiometers were hot glued to the desired location on the specimen. After potentiometers were installed and connected to the data acquisition system, the LED markers were installed. To attach the LED targets to the specimen, the contact surface was first ground to remove any whitewash or mill scale present. Then a small piece of double sided tape was used to attach the marker to the specimen. Digital cameras were positioned at various locations to document the test. A handheld camera was also used to capture close up pictures of damage throughout the test.

3.4.2 Loading

The specimens were tested with a quasi-static cyclic displacement protocol. The actuator was controlled with MTS FlexTest software, using manual displacement control. As described in Section 3.3.4, the actuator was pushed to the target displacement based on an averaged reading of story deflection from two string potentiometers.

<u>Main Protocol</u>

The main test consisted of pushing the frame back and forth at increasingly larger displacements until failure, as shown in Figure 3.33. The frame was first pushed to a positive target displacement (corresponding to the North brace in compression; North is labelled in the experimental setup diagram in Fig. 3.1) and then the same target displacement in the negative direction (South brace in compression). Two full cycles were run at each target displacement in order to capture cyclic strength degradation. The target displacements were set as multiples of the yield displacement, i.e. $0.5\Delta_y$, Δ_y, $2\Delta_y$, $3\Delta_y$, $4\Delta_y$ and so on.

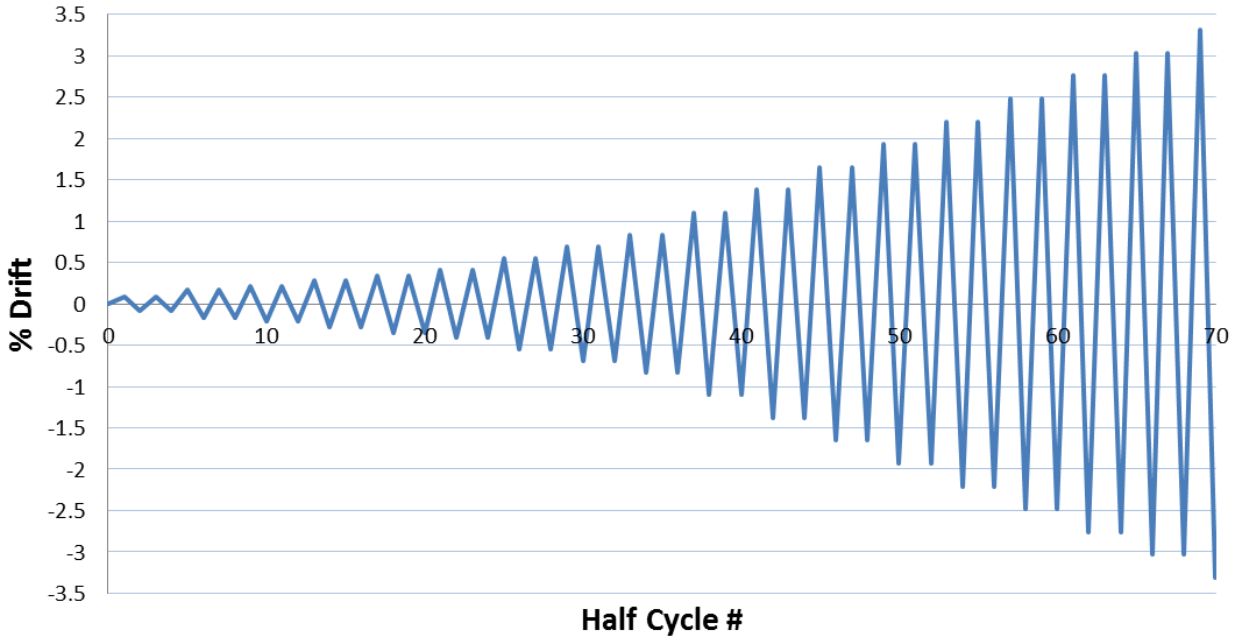

Figure 3.33: Main displacement protocol.

Post-Fracture Protocol

After fracture of both braces, post-fracture cycles were run to determine the residual lateral resistance of the frame after both braces had fractured. The specimens were loaded using a pre-programmed displacement protocol controlled by the actuator LVDT. This was done because it greatly expedites the testing process. It was not as important to hit specific drift targets in the post-fracture test because the goal was simply to determine the lateral resistance provided by frame action. The actuator displaced in increments of one inch each cycle, an only one cycle was run at each displacement.

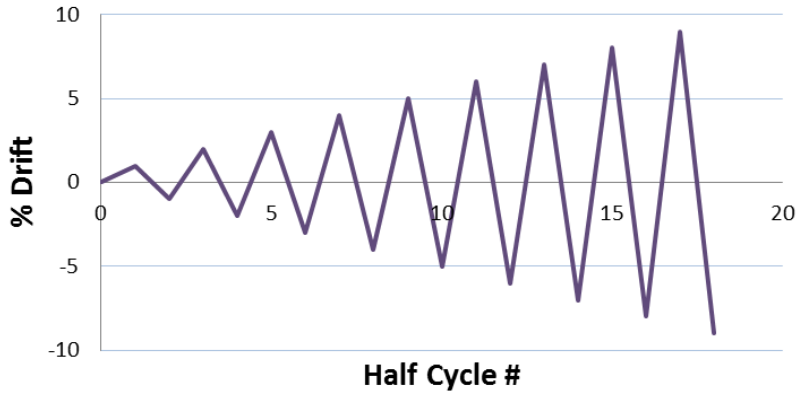

Figure 3.34: Post-Fracture displacement protocol.

Chapter 4

Test Observations

4.0 Introduction

This chapter will document the observed performance of the three chevron SCBF test specimens. To aid in the description and comparison of the specimens, a series of performance states are defined in Section 4.1. Sections 4.2 through 4.4 describe the observations for each test. For each specimen, the chapter includes the test objective and a detailed description of the frame performance, including a table documenting the performance states of the various components as a function of drift. Finally, a comparison of the specimen performance is presented in Section 4.5.

4.1 Performance State Descriptions

The performance of the specimens depends on the progression of yielding, onset of failure modes and development of the final failure modes. As such it is important to document the severity of yielding and damage throughout each test. Table 4.1 shows the yielding mechanisms and failure modes that were observed during the tests, which correspond to performance states defined in this section. The performance states are based on those developed by Ballard (2015). Each performance state is described by a letter and a number; in some cases an additional letter is necessary. The letter (shown in Table 4.2 next to the corresponding behavior) describes the type of damage, while the number describes the severity of the damage: 1-initial, 2-moderate, 3-severe, and 4-failure. The tables in this chapter provide pictures and definitions of each performance state. The rows of each table are in order of increasing severity, with increasingly darker shading to indicate the increased severity. The performance state abbreviations and shading are used in tables in Sections 4.2 through 4.4 to document the damage observed in each test.

Table 4.1 Observed Yield Mechanisms and Failure Modes

Brace Performance States	Connection Performance States	Frame Performance States
Brace Buckling (B1,B2)	Weld Tearing (WT1,WT2,WT3)	Frame Yielding (Y1,Y2,Y3)
Brace Plastic Hinging (B3-PH)	Plate Yielding (Y1,Y2,Y3)	Frame Local Buckling (LB1,LB2,LB3)
Brace Tearing (B3-BT)	Plate Cracking (PC1,PC2,PC3)	
Brace Fracture (B4-BF)	Bolt Fracture (FB)	

4.1.1 Brace Performance States

The brace performance is controlled by buckling, plastic hinge formation, tearing and fracture. Initially, the brace buckles in an approximate half sine wave (B1, B2). As out of plane deflection of the brace increases, the brace develops severe local cupping at the center of the brace (B3-BC) as a consequence of the formation of a plastic hinge. As the local buckling becomes more severe, striation lines begin to form when the brace straightens in tension and the brace starts to tear (B3-BT). Eventually the brace fractures through the entire section in tension (B4). Table 4.2 defines these performance states.

Table 4.2 Brace Performance States

Photograph	Abb.	Performance State	Description
	**B1**	Initial Global Buckling	Brace mid-span deflection is visible but less than twice the brace depth.*
	**B2**	Moderate Global Buckling	Brace mid-span deflection exceeds twice the brace depth.*
	**B3 – BC**	Brace Local Cupping Deformation	Visible cupping at brace midpoint.
	**B3 – BT**	Brace Tearing	Striation lines begin to separate in plastic hinge region of the brace.
	**B4**	Brace Fracture	Brace factures through entire section.

*The brace out of plane deformation was measured using Optotrak data in order to distinguish between B1 and B2 performance states.

4.1.2 Frame Performance States

The framing members (beam and columns) typically sustained yielding and local buckling during the tests. The two types of performance states for framing members correspond to these behaviors. For the framing members, the specific location of the observed damage is indicated, with another set of letters following the performance state (for example 'Y1-OF'). The locations are inner flange (IF), outer flange (OF) and web (W), and are shown in Figure 4.1 and 4.2 for the columns and the beam, respectively. The plastic hinge region for the column extends from 2 feet above the top edge of the corner gusset plate to 6 inches below the top edge of the corner gusset. The plastic hinge region in the beam extends out 2 feet on either side of the mid-span gusset plate. On the beam inner flange, the plastic hinge region ends 6 inches to the inside edge of the mid-span gusset. On the beam top flange, the plastic hinge region ends at the beam stiffeners. Tables 4.3 and 4.4 define the performance states for the beam and columns, with photographs shown for both members.

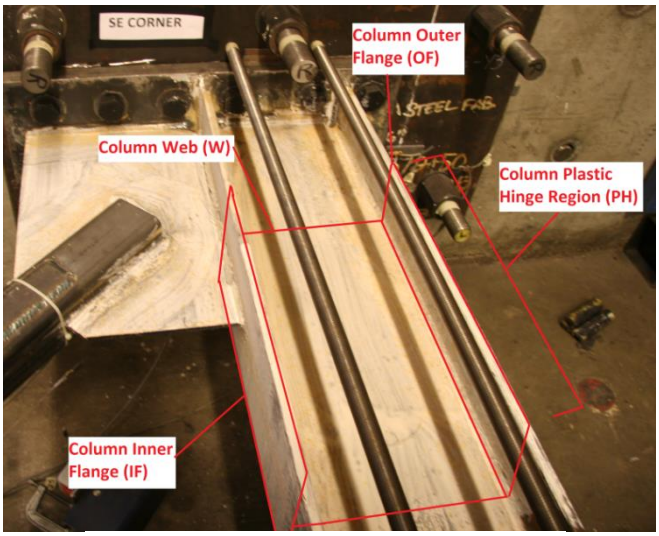

Figure 4.1: Column Damage Locations

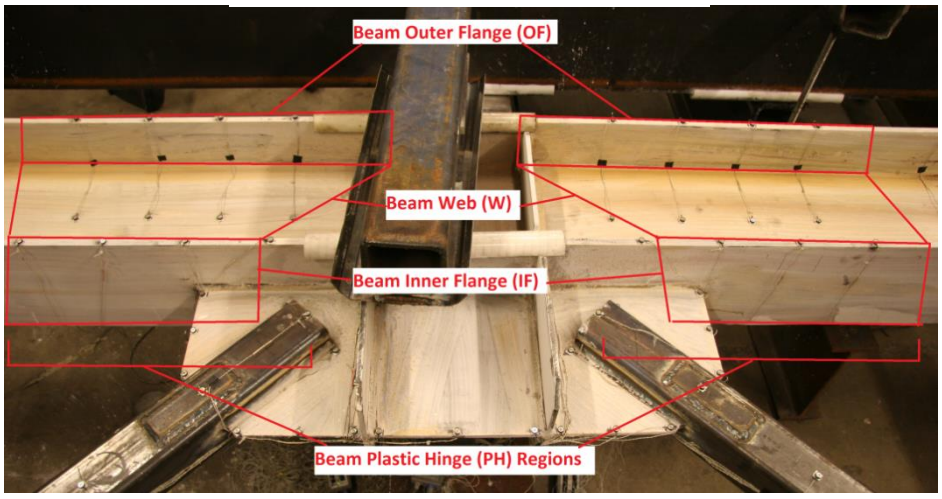

Figure 4.2: Beam Damage Locations

Table 4.3 Frame Yielding Performance States

Picture	Abb.	Performance State	Description
 	**Y1**	Initial Yielding	First visible yield lines in specified location.
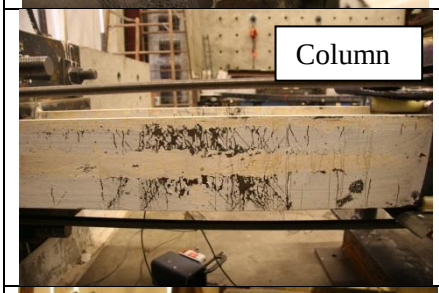 	**Y2**	Moderate Yielding	Whitewash is flaked off on 50% of the specified location.
 Not observed in beam.	**Y3**	Severe Yielding	Whitewash is flaked off on >80% of the specified location.

Table 4.4 Frame Local Buckling Performance States

Picture	Abb.	Performance State	Description
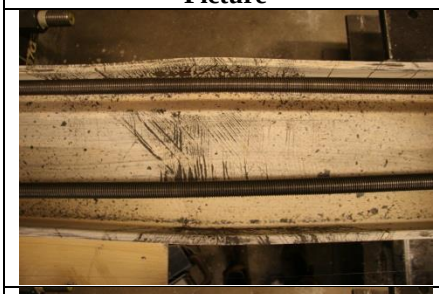	**Y1**	Initial Local Buckling	OOP local deformation observed in flange or web.
	**Y2**	Moderate Local Buckling	OOP local deformation exceeds element thickness.
	**Y3**	Severe Local Buckling	OOP local deformation exceeds two times the element thickness.

4.1.2 Connection Performance States

The connection performance states include plate yielding, plate cracking, weld tearing, and bolt fracture. The gusset plate connections experienced plate yielding, plate cracking, and weld tearing. The shear plate connections experienced plate yielding and, in Chevron 1, bolt fracture. There was also some bolt hole elongation in the beam web - photos of the final state of the bolt holes after both the main and post-fracture load cycles are included at the end of the chapter for each test. No damage was observed in the base plate or cap plate connections.

4.1.2.1 Plate Yielding

The plate yielding performance states are defined by the percentage of whitewash that has flaked off of the element in question. The initial (Y1), moderate (Y2), and severe (Y3) plate yielding performance states are defined in Table 4.5. Example photos are shown for both the gusset plates and shear plates.

For Chevron 1, the undersides of the gusset plates were not painted with whitewash so it is difficult to quantify the severity of the gusset plate yielding for that test. In the performance state table for Chevron 1, estimates of when plate yielding performance states occurred are given based on the results of Chevron 2 and 3 where the undersides of the gusset plates were painted.

4.1.2.2 Plate Cracking

Cracking was observed in the gusset plates at the toe of the brace-to-gusset welds and at the mid-span gusset-to-stiffener welds. Table 4.6 shows the initial (PC1) and moderate (PC2) cracking performance states. A severe (PC3) performance state is defined but it was not observed in any of the tests. In the performance state tables, plate cracking is indicated for the weld at which it occurred rather than the element that experienced cracking, because in the mid-span gusset plate cracks occurred at multiple locations.

4.1.2.3 Weld Tearing

Weld tearing performance states are defined by the percentage of the weld length that has torn, as shown in Table 4.7. The weld performance states were designed to mimic the fracture mechanics concepts of crack initiation (WT1), stable crack growth (WT2), and unstable crack growth (WT3). None of the welds experienced complete fracture. The damage states are defined by the percentage of the weld length that has fractured. For the mid-span gusset-to-beam weld, the weld can crack at both the North and South corner. The weld length is taken as the distance from the North or South edge of the weld to the stiffener on that side of the mid-span gusset plate. The weld crack lengths were measured on the top face of the weld only.

4.1.2.4 Bolt Fracture

Bolt fracture occurred in the shear plate connection in Chevron 1, on the same cycle as the first brace fracture. Table 4.8 defines the bolt fracture performance state.

Table 4.7 Plate Yielding Performance States

Picture	Abb.	Performance State	Description
 	**Y1**	Initial Yielding	First visible yield lines in specified location.
 	**Y2**	Moderate Yielding	Whitewash is flaked off on 20-50% of the plate area.
Not observed in gusset plate or shear plate.	**Y3**	Severe Yielding	Whitewash is flaked off on >50% of the plate area.

Table 4.8 Plate Cracking Performance States

Picture	Abb.	Performance State	Description
	**Y1**	Initial Cracking	First visible cracks appear in plate.
	**Y2**	Moderate Cracking	Plate cracks through entire thickness.
Not oberved during tests.	**Y3**	Severe Cracking	Plate crack exceeds 30% of plate dimension.

Table 4.9 Weld Tearing Performance States

Picture	Abb.	Performance State	Description
	**WT1**	Initial Weld Tearing	First visible weld cracks appear.
	**WT2**	Moderate Weld Tearing	Weld tear exceeds 10% of weld length.

	**WT3**	Severe Weld Tearing	Weld tear exceeds 30% of weld length.

Table 4.10 Bolt Performance States

Picture	Abb.	Performance State	Description
	**FB**	Bolt Fracture	Complete fracture of bolt occurs.

4.2 Chevron 1

Chevron 1, shown in Figure 4.3, had a beam with a DCR of 0.83 and was tested on October 11, 2016. Chevron 1 met all seismic code provisions for SCBFs (AISC 2010a). The purpose of this test was to provide a baseline of performance with which to compare the performance of the weak beam specimens.

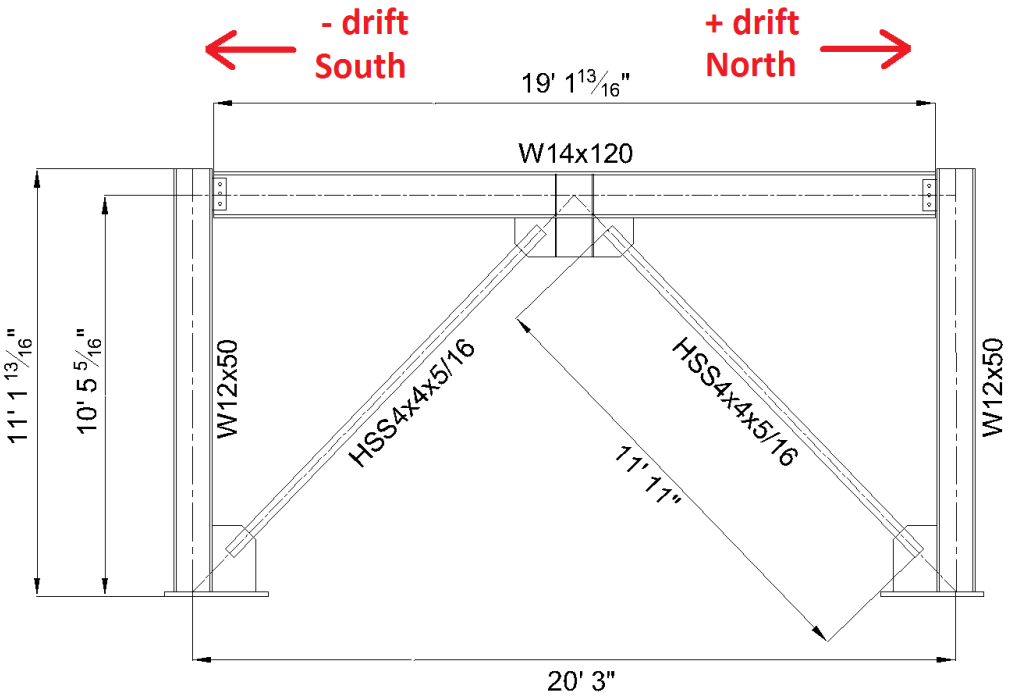

Figure 4.3: Chevron 1 drawing

Figure 4.4: Chevron 1 photograph.

4.2.1 Overview of Performance

Chevron 1 reached a maximum drift range of 6.3% and had a maximum lateral resistance of 234 kips, as shown in Figure 4.5. The beam did not yield and had a maximum deflection of 1.1 inches. The failure mode was brace fracture; the south brace fractured first at 3% drift, and the north brace fractured second at -3.3% drift. The braces began to buckle out of plane (OOP) at ±0.28% drift, and sustained progressively larger OOP buckling deformations each cycle, leading to plastic hinge formation in the center of the braces. The braces began to deform locally at mid-span as a result of plastic hinge formation, eventually leading to tearing and fracture of the braces. Connection damage included plate yielding, plate cracking, weld tearing, and bolt fracture. The columns sustained yielding and local buckling in the plastic hinge region. Table 4.9 shows the drift range at which certain performance states were observed.

After both braces had fractured, post-fracture cycles were run to determine the residual lateral resistance from frame action. The frame was cycled to ±5% drift, shown in Figure 4.5. The columns sustained more severe yielding and local bucking at high drift levels, but no other damage was observed.

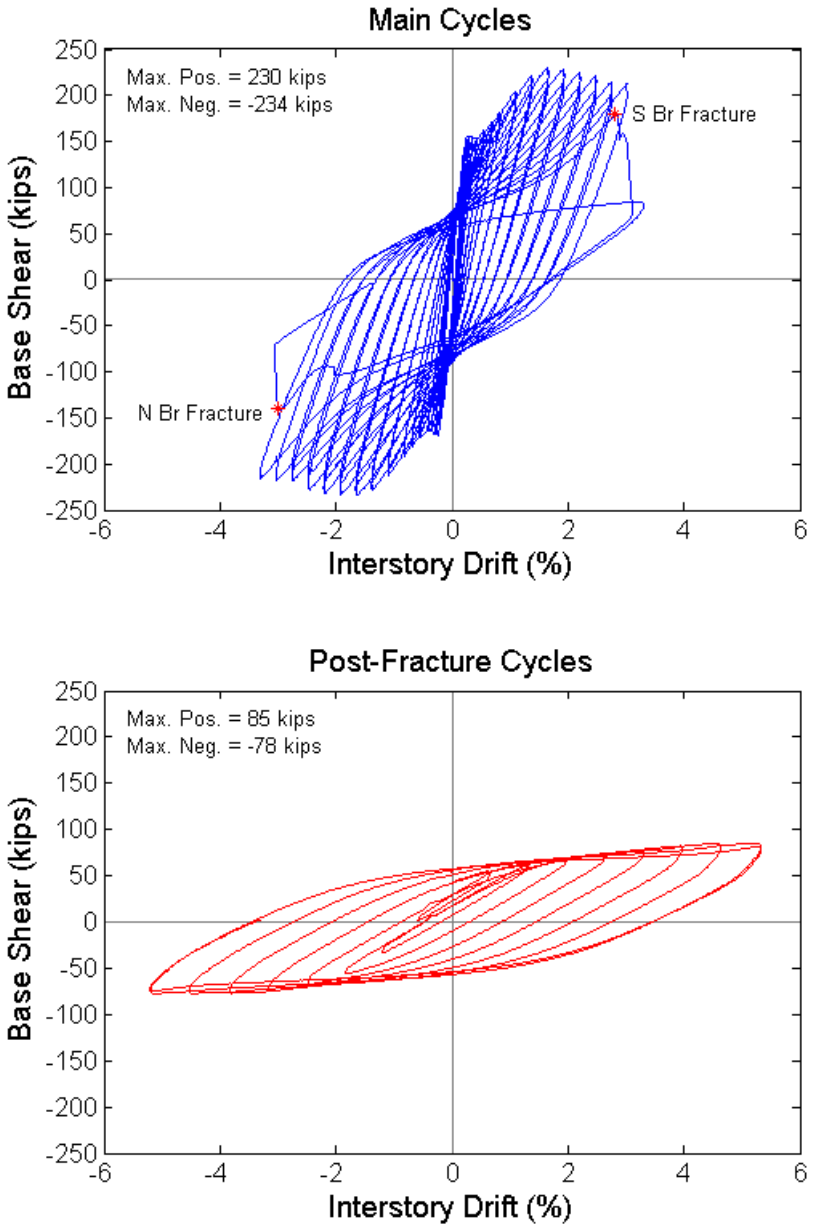

Figure 4.5: Chevron 1 Hysteresis

Table 4.11 Chevron 1 Performance States

		Low Drift									Moderate Drift				High Drift				
	Cycle	1-2	3-4	5-6	7-8	9-10	11-12	13-14	15-16	17-18	19-20	21-22	23-24	25-26	27-28	29-30	31-32	33-34	35-36
	Drift (+/-)(%)	0.088	0.138	0.207	0.276	0.344	0.413	0.551	0.689	0.827	1.102	1.378	1.654	1.929	2.205	2.480	2.756	3.031	3.307
	Drift Range (%)	0.18	0.28	0.41	0.55	0.69	0.83	1.10	1.38	1.65	2.20	2.76	3.31	3.86	4.41	4.96	5.51	6.06	6.61
	South Brace				B1						B2			B3-BC			B3-BT	B4-BF	
	North Brace				B1						B2				B3-BC		B3-BT		B4-BF
SE Corner	**South Column**											Y1		Y2	LB1		Y3		
SE Corner	**GP-Column Weld**															WT1			
SE Corner	**Brace-GP Weld**															WT1			
SE Corner	**Gusset Plate***							Y1					Y2						
NE Corner	**North Column**											Y1		Y2	LB1		Y3		LB2
NE Corner	**GP-Column Weld**															WT1		WT2	WT3
NE Corner	**Brace-GP Weld**															WT1			
NE Corner	**Gusset Plate***							Y1					Y2						
Mid-Span Gusset	**GP-Beam Weld (N)**													WT1		WT2			WT3
Mid-Span Gusset	**GP-Beam Weld (S)**																WT1	WT2	
Mid-Span Gusset	**Brace-GP Weld (N)**													PC1					
Mid-Span Gusset	**Brace-GP Weld (S)**																		
Mid-Span Gusset	**GP-Stiffener Weld (N)**															PC1			
Mid-Span Gusset	**GP-Stiffener Weld (S)**															PC1			
Mid-Span Gusset	**Gusset Plate (N)***						Y1					Y2							
Mid-Span Gusset	**Gusset Plate (S)***						Y1					Y2							
Mid-Span Gusset	**Beam**																		
	North Shear Tab										Y1								
	South Shear Tab										Y1								BF

*Estimate based on the results of Chevron 2 and 3

4.2.2 Low Drift (Story drift < 1%)

The frame remained elastic until a drift range of 0.55%. The following significant events occurred at low drifts:

- The North brace began to buckle (B1) on the first cycle at 0.28% drift and
- The South brace began to buckle (B1) on the first cycle at -0.28% drift.
- The gusset plates began to yield (Y1) at ±0.7% drift.

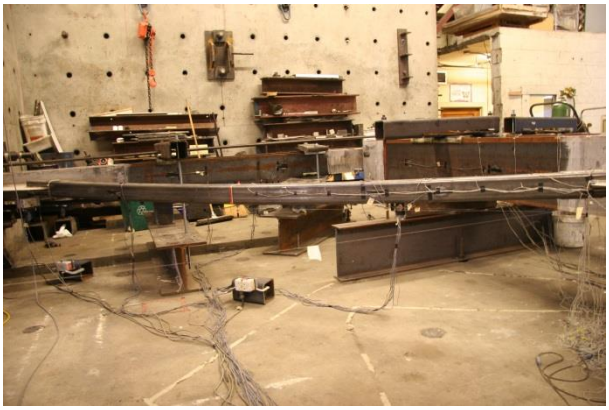

Figure 4.6: S brace buckling at -0.28% drift (B1).

Figure 4.7: N brace buckling at +0.7% drift (B1).

4.2.3 Moderate Drift (1% < Story drift < 2%)

Significant events during the moderate drift cycles included:

- At ±1.1% story drift, the braces buckled out of plane more than twice the depth of the brace (B2)
- At ±1.1% story drift, the shear plates began to yield (Y1)
- At ±1.4% story drift the columns began to yield (Y1) in the plastic hinge region
- At -1.65% story drift, tears initiated at the toes of the south brace-to-mid-span gusset plate welds (WT1)
- At ±1.9% story drift the columns experience moderate yielding (Y2) in the plastic hinge region
- At +1.9% story drift, cracks initiated in the gusset plate at the toes of the north brace-to-mid-span gusset plate welds (PC1)
- At +1.9% story drift, a tear initiated in the north toe of the mid-span gusset-to-beam weld (WT1)
- At -1.9% story drift, slight cupping was observed at mid-span of the south brace (B3-PH)

Figure 4.9: N brace buckling at +1.1% drift (B2).

Figure 4.10: Initial shear tab yielding at -1.1% drift (Y1).

Figure 4.11: N col. initial yielding at +1.4% drift(Y1).

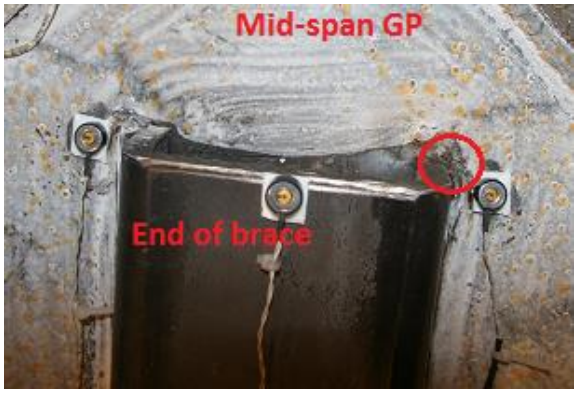

Figure 4.12: GP crack at N brace-to-gusset weld (PC1).

Figure 4.13: N col. moderate yielding at +1.9% drift (Y2-PH).

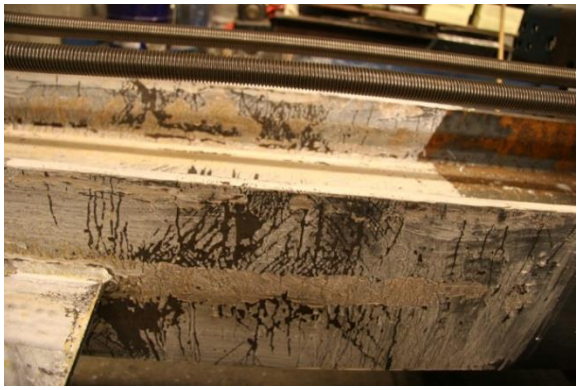

Figure 4.14: S col. moderate yielding at -1.9% drift (Y2-PH).

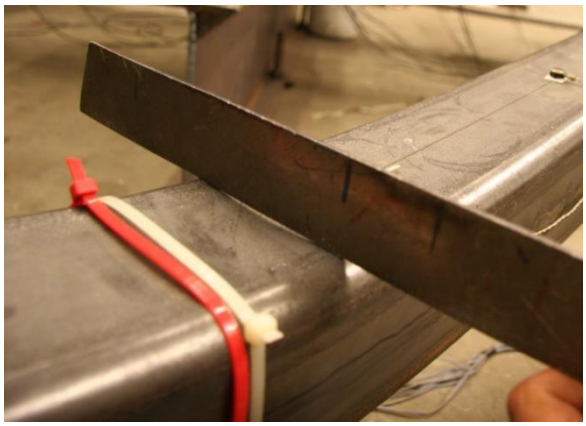

Figure 4.15. S brace initial cupping at -1.9% drift (B3-PH).

Figure 4.16: Initial tear N mid-span GP-to-beam weld at +1.9% drift (WT1).

4.2.4 High Drift (Story drift > 2%)

At high story drifts there was tearing at the toe of all gusset-to-column and gusset-to-beam welds. Table 4.10 shows the progression of damage to these welds throughout the higher drift cycles. In addition to weld tearing, the following significant events occurred:

- At +2.2% story drift, slight cupping was observed in the center of the North brace (B3-PH)
- At ±2.2% story drift, the columns sustained initial local buckling of the flanges in the plastic hinge region (LB1-IF/OF) (Fig. 4.17)
- At ±2.48% drift, plate cracking was observed at both the North and South mid-span gusset-to-stiffener weld (PC1)
- At ±2.76% drift, the columns experienced severe yielding (Y3) in the plastic hinge region

- At the second cycle at ±2.76% story drift, striation lines were observes at the center of both the North and South brace (B3-BT)
- At ±3.0% drift, the columns sustained initial local buckling of the web in the plastic hinge region (LB1-W)
- At the second cycle of +3.0% drift, the South brace fractured completely (B4-BF)
- At the second cycle of +3.0% drift, the top bolt in the South shear plate fractured (FB)
- At -3.3% drift the North column experienced moderate local buckling in the flanges (LB2-OF/IF)
- At the second cycle of -3.31% drift, the North brace fractured completely (B4-BF)

Table 4.12 Chevron 1 Weld crack propagation

Half Cycle #	Drift (%)	N mid-span gusset-to-beam	S mid-span gusset-to-beam	NE gusset-to-column	SE gusset-to-column
49	1.93	1/4”	-	-	-
53	2.2	1”	-	-	-
57	2.48	2”	-	2”	-
58	-2.48	2”	-	2”	1/4”
60	-2.48	2”	-	2”	1/2”
61	2.76	2-3/4”	-	3-1/4”	1/2”
63	2.76	2-3/4”	-	3-1/2”	1/2”
64	-2.76	2-3/4”	7/8”	3-1/2”	1/2”
65	3.03	3”	7/8”	4”	1/2”
66	-3.03	3”	1-1/2”	4”	1/2”
67	3.03	3-1/2”	1-1/2”	4-1/2”	1/2”
69	3.31	4”	1-1/2”	5”	1/2”

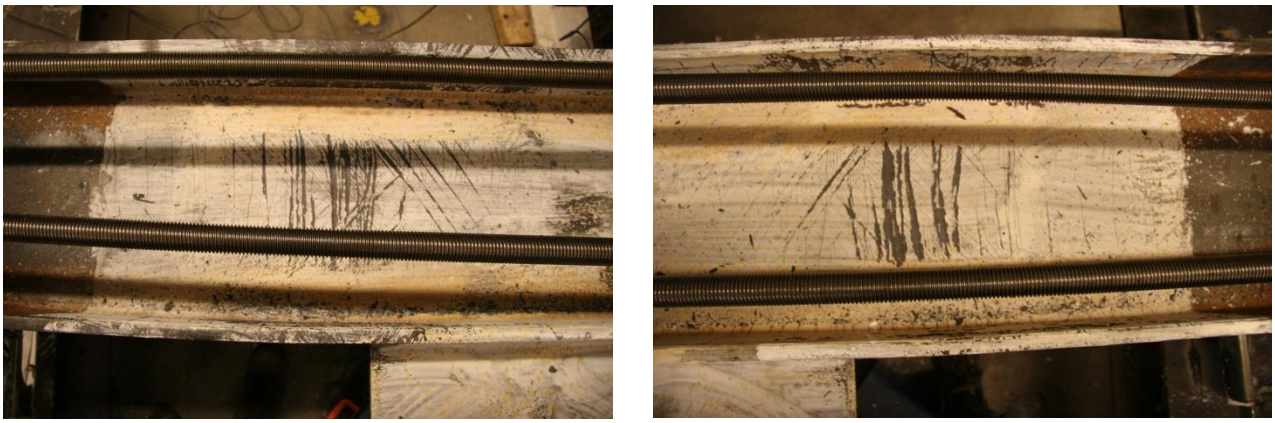

Figure 4.17: Initial local buckling in N (left) and S (right) column flanges at +2.2% drift (LB1-OF/IF).

Figure 4.18: Crack propagation in N toe of mid-span gusset-to-beam weld (WT1,2).

Figure 4.19: Crack propagation in NE corner gusset-to-column weld (WT1,2,3).

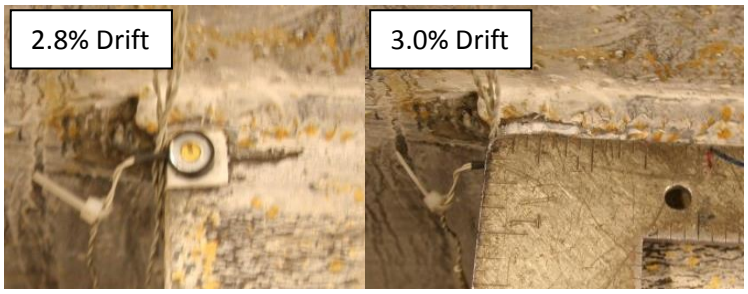

Figure 4.20: Crack propagation in S mid-span gusset-to-beam weld (WT1).

Figure 4.21: Plate cracking at S (left) and N (right) gusset-to-stiffener welds (PC1).

Figure 4.22: Severe yielding in N col. (left) and S col. (right) at 2.76% drift (Y3-PH).

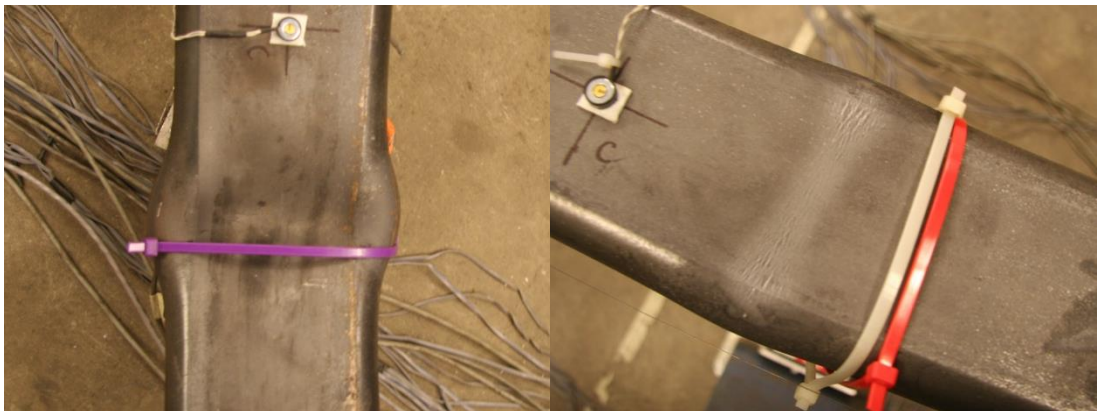

Figure 4.23: Severe local cupping of N brace (left) and initial tearing of S brace (right) at +3.0% drift.

Figure 4.24: S brace fracture at second cycle of +3.0% drift (B4-BF).

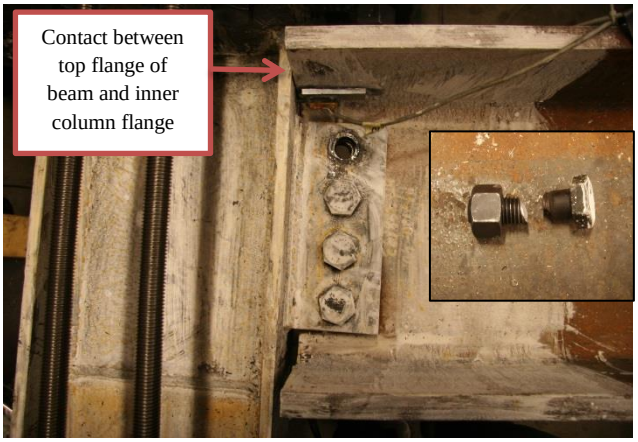

Figure 4.25: S shear tab bolt fracture at +3.0% drift (FB).

Figure 4.26: N column moderate local buckling at -3.3% drift (LB2-IF).

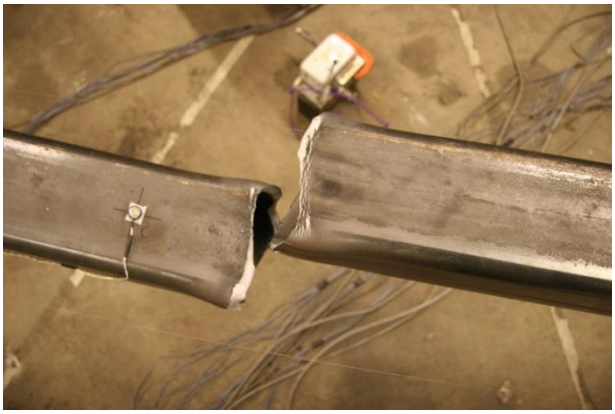

Figure 4.27: N brace fracture on second cycle at -3.3% drift (B4-BF).

4.2.5 Post-Fracture Cycles

The frame was cycled to ±5% drift after both braces had fractured. The columns continued to yield and undergo local buckling, reaching the performance state of severe local buckling (LB3). After the test the frame was disassembled and it was noted that bolt hole elongation had occurred in the beam web, as shown in Figures 4.28 and 4.29.

Figure 4.28: S beam web bolt hole elongation.

Figure 4.29: N beam web bolt hole elongation.

4.3 Chevron 2

Chevron 2, shown in Figure 4.30, was tested on November 21, 2016. The purpose of this test was to investigate the effect of a weak beam on the cyclic behavior of chevron SCBFs. Chevron 2 had identical frame geometry, column size, brace size, and connection details as Chevron 1 but utilized a W14x61 beam instead of a 14x120 beam. The W14x61 beam had a DCR of 1.72 for the AISC requirement to develop the unbalanced load from the braces, as described in Section 3.2.3. All other components and welds met seismic code requirements (AISC 2010a).

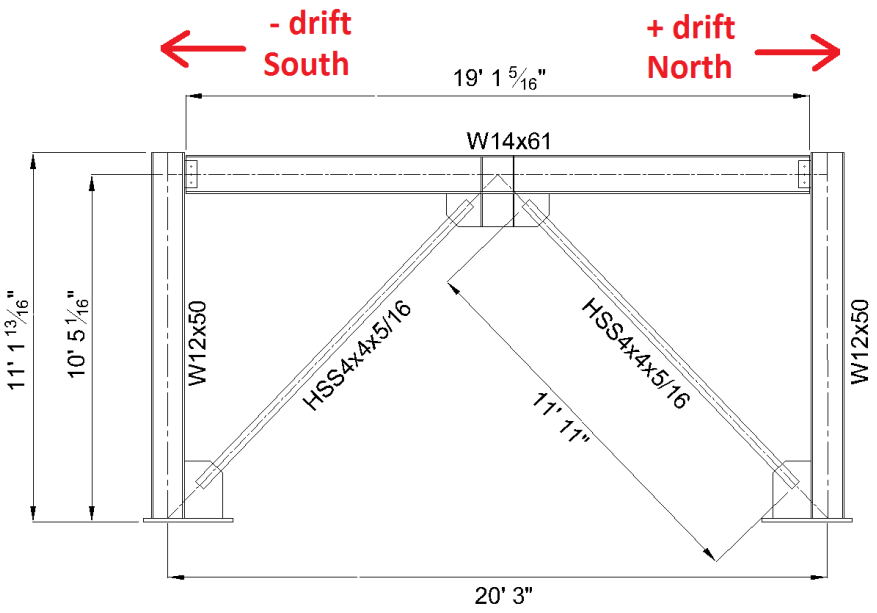

Figure 4.30: Chevron 2 drawing.

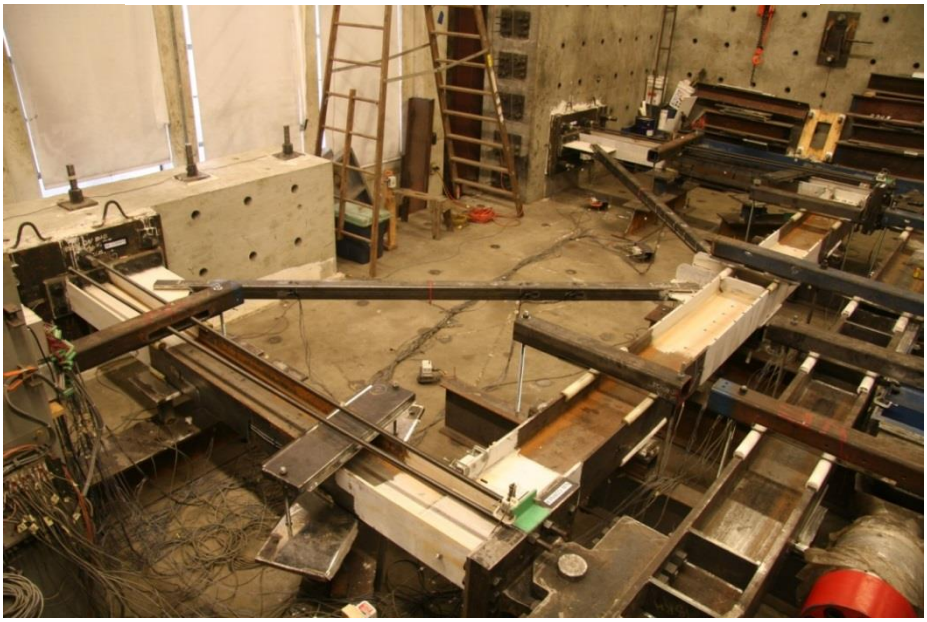

Figure 4.31: Chevron 2 photo.

4.3.1 Overview of Performance

Chevron 2 reached a maximum drift range of 6.6% and had a maximum lateral resistance of 207 kips, as shown in Figure 4.32. The beam experienced slight yielding (Y1) and had a maximum deflection of 1.8 inches. The failure mode was brace fracture; the south brace fractured first at the first +3.3% drift cycle, and the north brace fractured at the second -3.3% drift cycle. The braces began to buckle OOP at ±0.28% drift, and sustained progressively larger OOP buckling deformations each cycle, leading to plastic hinge formation in the center of the braces. The braces began to deform locally at mid-span as a result of plastic hinge formation, eventually leading to tearing and fracture of the braces. Connection damage included plate yielding, plate cracking, and weld tearing. The columns sustained yielding and local buckling in the plastic hinge region. Table 4.11 shows the drift at which performance states were observed.

After both braces had fractured, post-fracture cycles were run to determine the residual lateral resistance from frame action. The frame was cycled to ±4.5% drift; the force-drift response is shown in Figure 4.32. The columns sustained more severe yielding and local bucking at high drift ranges, but no other damage was observed.

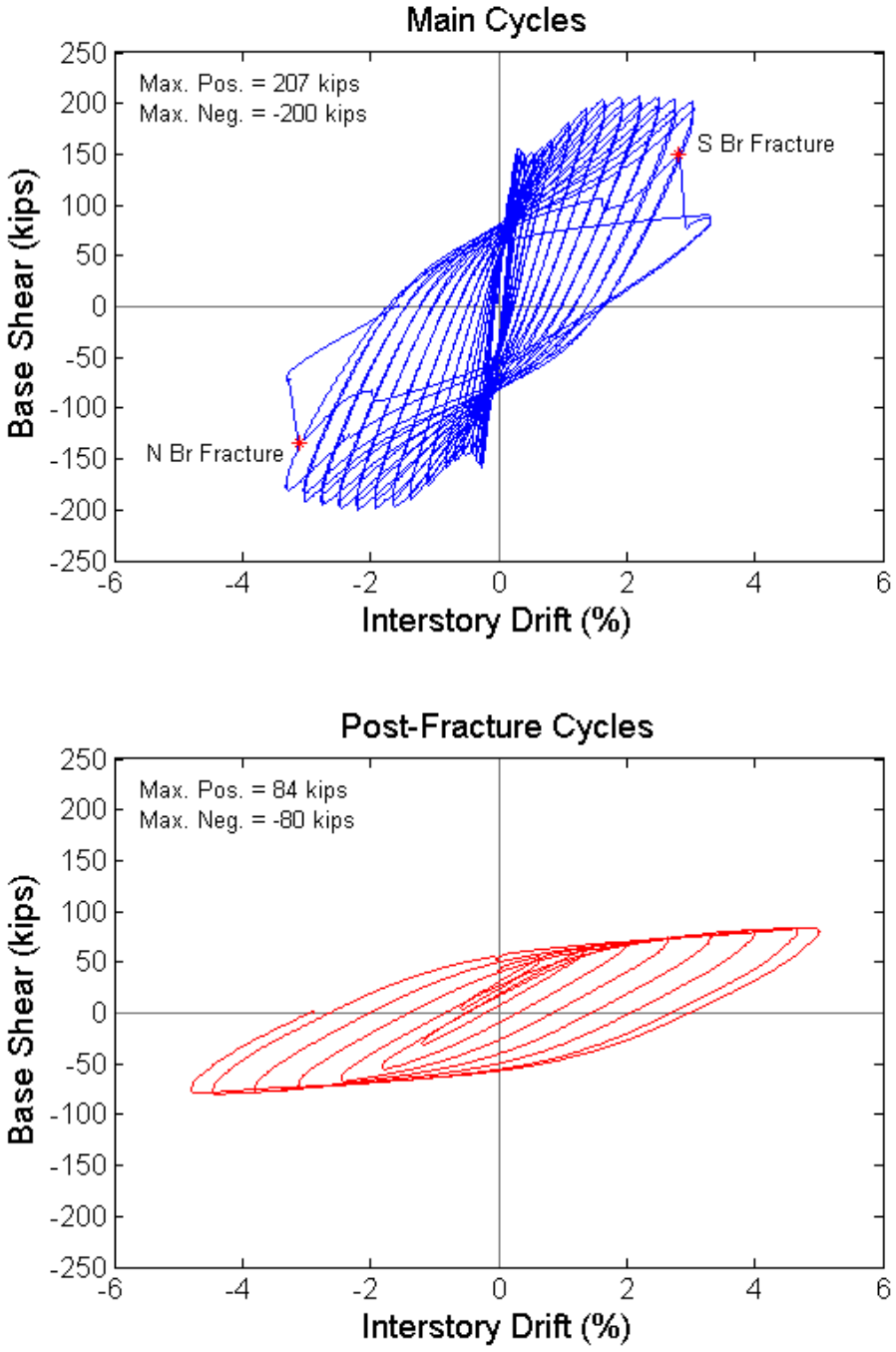

Figure 4.32: Chevron 2 Hysteresis

Table 4.13 Chevron 2 Performance States

		Low Drift									Moderate Drift				High Drift				
	Full Cycle #	1-2	3-4	5-6	7-8	9-10	11-12	13-14	15-16	17-18	19-20	21-22	23-24	25-26	27-28	29-30	31-32	33-34	35-36
	Drift (+/-)(%)	0.088	0.138	0.207	0.276	0.344	0.413	0.551	0.689	0.827	1.102	1.378	1.654	1.929	2.205	2.480	2.756	3.031	3.307
	Drift Range (%)	0.18	0.28	0.41	0.55	0.69	0.83	1.10	1.38	1.65	2.20	2.76	3.31	3.86	4.41	4.96	5.51	6.06	6.61
	South Brace				B1						B2				B3-BC			B3-BT	B4-BF
	Noth Brace				B1						B2				B3-BC			B3-BT	B4-BF
SE Corner	South Column											Y1		Y2	LB1		Y3		
SE Corner	GP-Column Weld														WT1	WT2			
SE Corner	Brace-GP Weld															WT1			
SE Corner	Gusset Plate							Y1					Y2						
NE Corner	North Column											Y1		Y2	LB1		Y3		
NE Corner	GP-Column Weld															WT1		WT2	
NE Corner	Brace-GP Weld																WT1		
NE Corner	Gusset Plate							Y1					Y2						
Mid-Span Gusset	GP-Beam Weld (N)												WT1	WT2		WT3			
Mid-Span Gusset	GP-Beam Weld (S)												WT1		WT2			WT3	
Mid-Span Gusset	Brace-GP Weld (N)														PC1				
Mid-Span Gusset	Brace-GP Weld (S)														PC1				
Mid-Span Gusset	GP-Stiffener Weld (N)															PC1			
Mid-Span Gusset	GP-Stiffener Weld (S)															PC1			
Mid-Span Gusset	Gusset Plate (N)						Y1					Y2							
Mid-Span Gusset	Gusset Plate (S)						Y1					Y2							
Mid-Span Gusset	Beam											Y1-OF		Y1-IF					
	North Shear Tab						Y1												
	South Shear Tab						Y1												

4.3.2 Low Drift (Story drift < 1%)

Significant events during the low drift cycles included:

- The North brace began to buckle (B1) on the first cycle at 0.28% drift.
- The South brace began to buckle (B1) on the first cycle at -0.28% drift.
- The mid-span gusset and the shear plates began to yield (Y1) at ±0.4% drift.
- The corner gusset plates began to yield at ±0.55% drift.

Figure 4.33: Initial yielding in N shear tab at +0.4% drift (Y1).

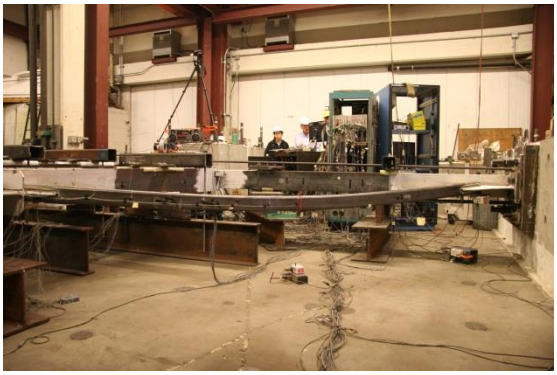

Figure 4.34: N brace buckling at 0.41% drift (Y1).

Figure 4.35: Shear tab yielding at 0.83% drift (Y1).

Figure 4.36: Mid-span GP yielding at -0.83% drift.

4.3.3 Moderate Drift (1% < Story drift < 2%)

Significant events during the moderate drift cycles included:

- At ±1.1% drift, the braces buckled out of plane more than twice the depth of the brace (B2)
- At +1.4% drift, the beam began to yield in the outer flange in the plastic hinge region (Y1-OF)
- At ±1.4% drift, the columns began to yield (Y1) in the plastic hinge region
- At +1.65% drift, a tear initiated at the North edge of the mid-span gusset-to-beam weld (WT1)
- At -1.65% drift, a tear initiated at the South edge of the mid-span gusset-to-beam weld (WT1)
- At +1.93% drift, the beam began to yield in the inner flange in the plastic hinge region (Y1-IF)
- At ±1.93% drift, the columns experienced moderate yielding in the plastic hinge region (Y2)
- At ±1.93% drift, cracks appeared in the mid-span gusset plate at the toe of the brace-to-mid-span gusset welds (PC1)
- At +1.93% drift, the crack at the North edge of the mid-span gusset-to-beam weld grew to 3 inches (WT2)

Figure 4.37: N brace buckling at +1.1% drift (B1).

Figure 4.38: Beam OF initial yielding at 1.4% drift (Y1-OF).

Figure 4.39: N col. initial yielding at +1.4% drift (Y1-OF).

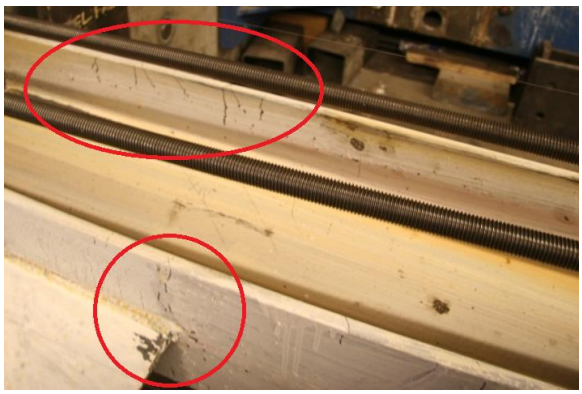

Figure 4.40: S col. initial yielding at +1.4% drift (Y1-OF).

Figure 4.41: GP yielding at 1.7% drift (Y1).

Figure 4.42: Beam IF initial yielding at 1.9% drift (Y1-IF).

Figure 4.43: S col. moderate yielding at 1.9% drift (Y1-OF/IF).

Figure 4.44: N col. moderate yielding at 1.9% drift (Y1-OF/IF).

4.3.2.3 High Drift (Story drift > 2%)

At high story drifts there was tearing at the edge of all gusset-to-column and gusset-to-beam welds. Table 4.12 shows the progression of tearing in these welds throughout the higher drift cycles. In addition to weld tearing, the following significant events occurred:

- At ±2.2% drift, slight cupping was observed in the center of the both the North and South brace (B3-PH)
- At ±2.2% drift, the columns underwent initial local buckling of the flanges in the plastic hinge region (LB1-OF/IF)
- At -2.48% drift, cracks initiated at the end of the SE corner brace-to-gusset welds (WT1)
- At ±2.48% drift, plate cracking was observed at both the North and South mid-span gusset-to-stiffener welds (PC1)
- At 2.76% drift, cracks initiated at the end of the NE corner brace-to-gusset welds (WT1)
- At 3.0% drift, striation lines appeared in the center of each brace (B3-BT)
- At the first cycle of 3.31% drift, the South brace fractured completely (B4-BF)
- At the second cycle of -3.31% drift, the North brace fractured completely (B4-BF)

Table 4.14 Chevron 2 Weld crack propagation

Half Cycle #	Drift (%)	N mid-span gusset-to-beam	S mid-span gusset-to-beam	NE gusset-to-column	SE gusset-to-column
45	1.38	1-1/2”	-	-	-
46	-1.38	1-1/2”	1/2”	-	-
49	1.93	3”	1/2”	-	-
50	-1.93	3”	1”	-	-
54	-2.21	3”	2-1/2”	-	1/4”
57	2.48	4”	2-1/2”	1/4”	1/4”
58	-2.48	4”	3-1/2”	1/4”	1-1/2”
61	2.76	5”	3-1/2”	3/4”	1-1/2”
62	-2.76	5”	3-1/2”	3/4”	2”
65	3.03	5”	3-1/2”	2-1/4”	2”
66	-3.03	5”	4”	2-1/4”	3-1/2”
69	3.31	5-1/2”	4”	3”	3-1/2”

Figure 4.45: Initial col. local buckling at 2.2% drift (LB1-OF/IF).

Figure 4.46: Brace buckling at 2.5% drift (B1).

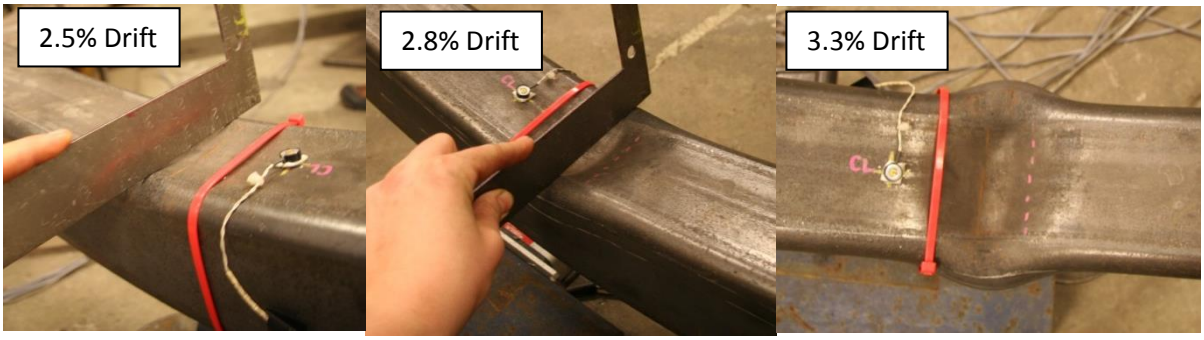

Figure 4.47: Progression of local cupping in S brace (B3-PH).

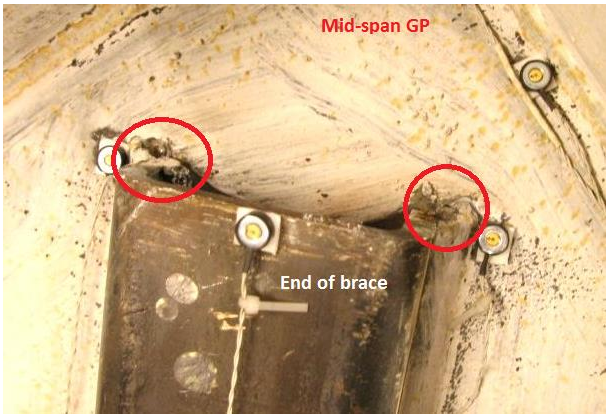

Figure 4.48: Plate cracking at toe of brace-to-mid-span gusset weld (PC1).

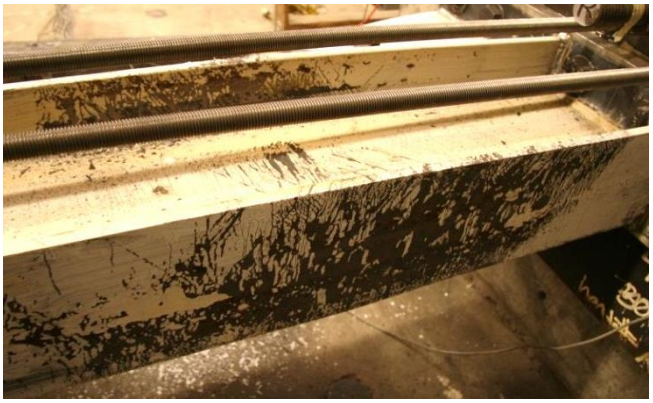

Figure 4.49: S col. severe yielding at 2.8% drift (Y3-OF/IF).

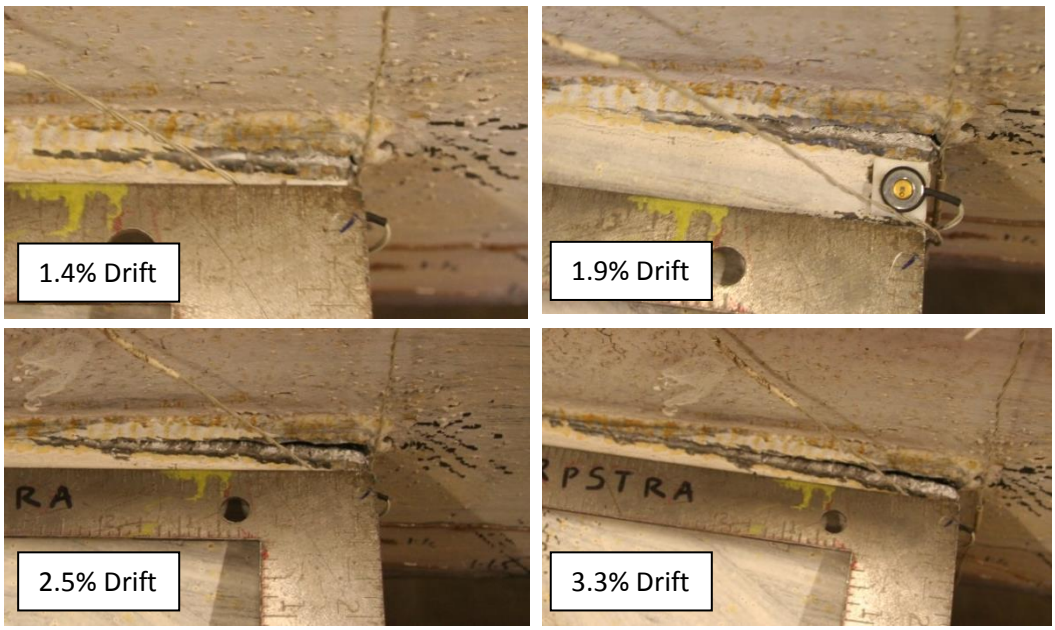

Figure 4.50: Progression of N mid-span gusset-to-beam weld crack (WT1/2).

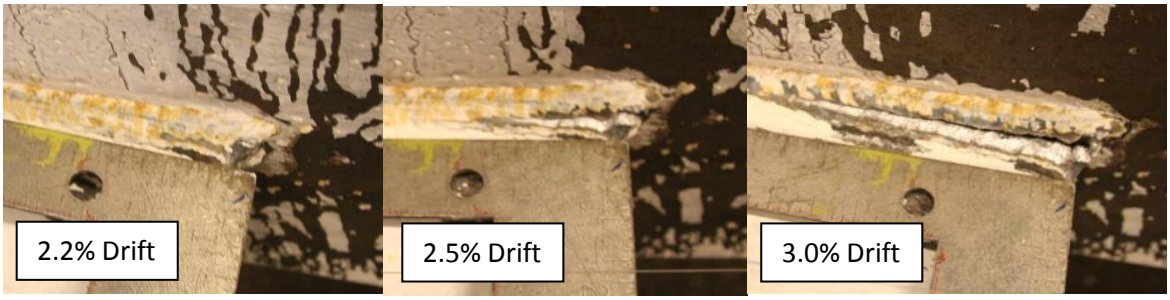

Figure 4.51: Progression of SE corner gusset-to-column weld crack (WT1/2).

Figure 4.52: S brace fracture 1st cycle at 3.3% drift (B4-BF).

Figure 4.53: N brace buckling at 3.3% drift (B3-PH).

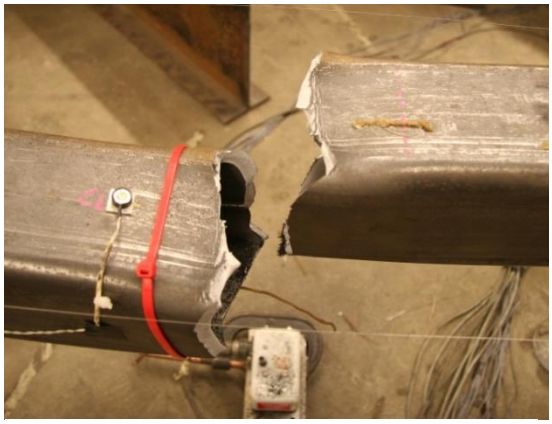

Figure 4.54: N brace fracture at -3.3% drift (B4-BF).

Figure 4.55: Extent of beam yielding at end of test (Y1-OF/IF).

4.3.5 Post-Fracture Cycles

The frame was cycled to ±4.5% drift after both braces had fractured. The columns continued to yield and undergo local buckling, reaching the performance state of severe local buckling (LB3). After the test the frame was disassembled and it was noted that slight bolt hole elongation had occurred the top and bottom bolt holes in the beam web, as shown in Figure 4.56 and 4.57.

Figure 4.56: S beam web bolt hole elongation.

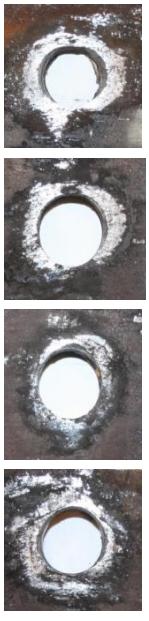

Figure 4.57: N beam web bolt hole elongation.

4.4 Chevron 3

Chevron 3, shown in Figure 4.59, was tested on February 6, 2017. The purpose of this test was to investigate the effect of a weak beam on the cyclic behavior of chevron SCBFs. Chevron 3 had identical frame geometry, column size, brace size, and connection details as Chevron 1 and 2 but utilized a different beam size than the previous tests. The W14x38 beam used in Chevron 3 had a DCR of 2.67 for the AISC requirement to develop the unbalanced load from the braces, as described in Section 3.2.3. All other components and welds met seismic code requirements (AISC 2010a).

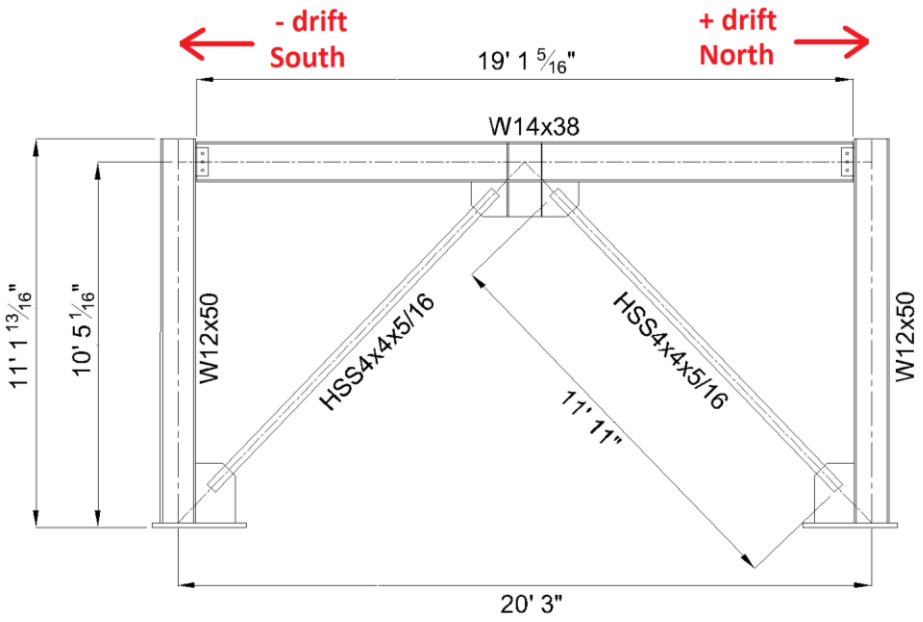

Figure 4.58: Chevron 3 drawing.

Figure 4.59: Chevron 3 photo.

4.4.1 Overview of Performance

Chevron 3 reached a maximum drift range of 7.2% and had a maximum lateral resistance of 172 kips, as shown in Figure 4.60. The beam underwent moderate yielding and had a maximum deflection of 3.0 inches. The failure mode was brace fracture; the north brace fractured first at the first -3.6% drift cycle, and the north brace fractured at the second -3.6% drift cycle. The braces began to buckle OOP at ±0.28% drift, and sustained progressively larger OOP buckling deformations each cycle, leading to plastic hinge formation in the center of the braces. The brace began to deform locally at mid-span as a result of plastic hinge formation, eventually leading to tearing and fracture of the braces. Connection damage included plate yielding, plate cracking, and weld tearing. The columns sustained yielding and local buckling in the plastic hinge region. Table 4.13 shows the progression of damage in the frame throughout the test.

After both braces had fractured, post-fracture cycles were run to determine the residual lateral resistance from frame action. The frame was cycled to ±5% drift, as shown in Figure 4.60. The columns sustained more severe yielding and local bucking in the plastic hinge region at high drifts, but no other damage was observed.

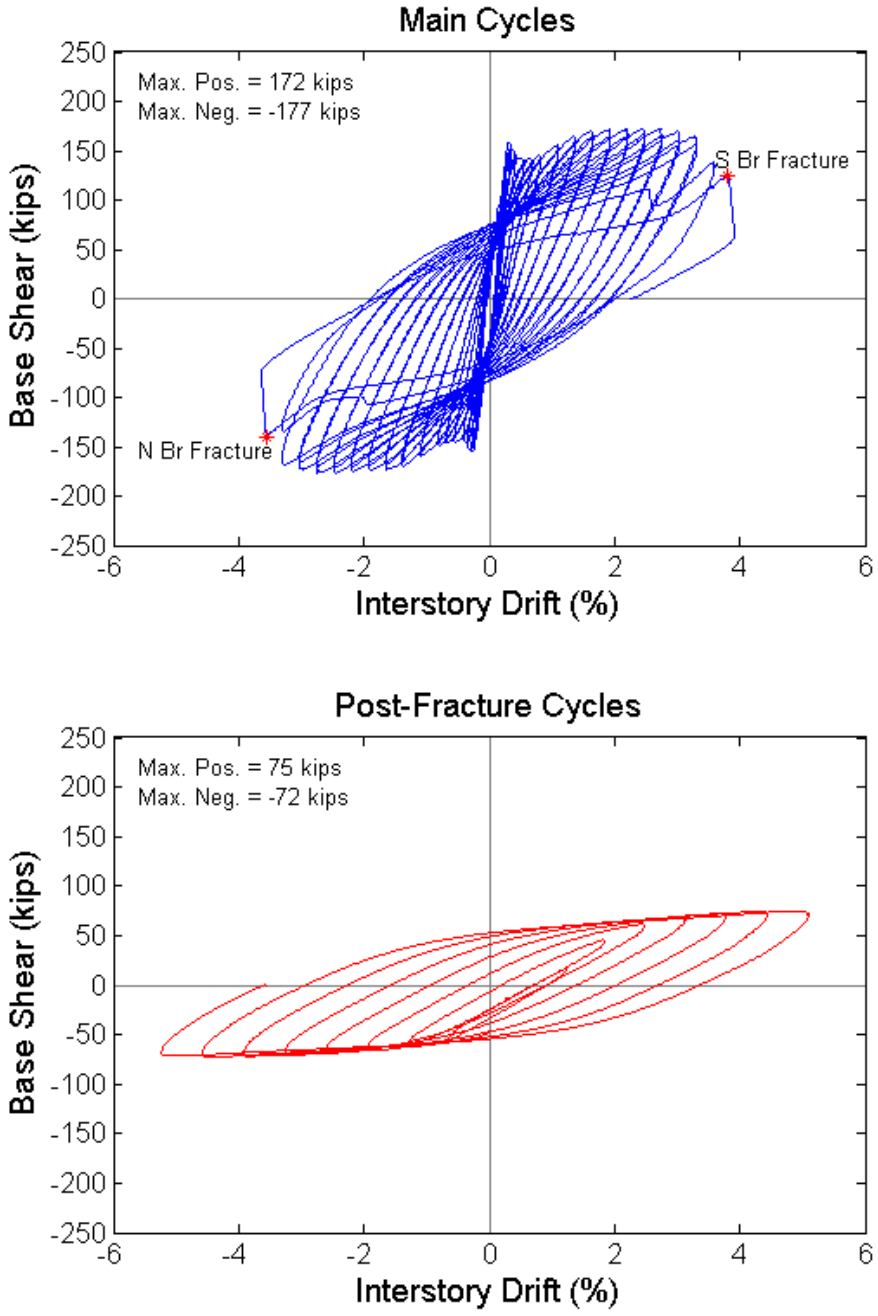

Figure 4.60: Chevron 3 Hysteresis

Table 4.15 Chevron 3 Performance States

		Low Drift									Moderate Drift				High Drift					
	Cycle	1-2	3-4	5-6	7-8	9-10	11-12	13-14	15-16	17-18	19-20	21-22	23-24	25-26	27-28	29-30	31-32	33-34	35-36	37-38
	Drift (+/-)(%)	0.088	0.138	0.207	0.276	0.344	0.413	0.551	0.689	0.827	1.102	1.378	1.654	1.929	2.205	2.480	2.756	3.031	3.307	3.583
	Drift Range (%)	0.18	0.28	0.41	0.55	0.69	0.83	1.10	1.38	1.65	2.20	2.76	3.31	3.86	4.41	4.96	5.51	6.06	6.61	7.17
	South Brace				B1					B2				B3-BC					B3-BT	B4-BF
	Noth Brace				B1					B2				B3-BC					B3-BT	B4-BF
SE Corner	South Column											Y1		Y2	LB1		Y3	LB1	LB2	
SE Corner	GP-Column Weld														WT1				WT2	
SE Corner	Brace-GP Weld															WT1				
SE Corner	Gusset Plate							Y1					Y2							
NE Corner	North Column											Y1		Y2	LB1		Y3			
NE Corner	GP-Column Weld																WT1		WT2	
NE Corner	Brace-GP Weld															WT1				
NE Corner	Gusset Plate							Y1					Y2							
Mid-Span Gusset	GP-Beam Weld (N)														WT1		WT2			
Mid-Span Gusset	GP-Beam Weld (S)														WT1					
Mid-Span Gusset	Brace-GP Weld (N)															PC1				
Mid-Span Gusset	Brace-GP Weld (S)															PC1				
Mid-Span Gusset	GP-Stiffener Weld (N)															PC1			PC2	
Mid-Span Gusset	GP-Stiffener Weld (S)															PC1			PC2	
Mid-Span Gusset	Gusset Plate (N)						Y1					Y2								
Mid-Span Gusset	Gusset Plate (S)						Y1					Y2								
Mid-Span Gusset	Beam					Y1												Y2		
	North Shear Tab					Y1												Y2		
	South Shear Tab					Y1												Y2		

4.4.2 Low Drift (Story drift < 1%)

The following significant events occurred at low story drifts:

- The braces began to buckle at ±0.28% drift (B1)
- At ±0.34% drift , the shear plates began to yield (Y1) near the top bolt
- At ±0.34% drift , both the top and bottom flange of the beam began to yield in the plastic hinge region (Y1-OF and Y1-IF)
- At ±0.41% drift , the mid-span gusset plate began to yield (Y1)
- At ±0.55% drift , the corner gusset plates began to yield (Y1)
- At ±0.83% drift, the braces buckled out of plane more than twice the depth of the brace (B2)

Figure 4.61: S shear tab initial yielding at 0.41% drift (Y1).

Figure 4.62: N brace buckling at 0.7% drift (B1).

Figure 4.63: Mid-span GP initial yielding at 0.4% drift (Y1).

Figure 4.64: Initial yielding in beam IF at 0.41% drift (Y1-IF).

Figure 4.65: Beam yielding at 0.83% drift (Y1-OF).

Figure 4.66: S shear tab yielding at -0.83% drift (Y1).

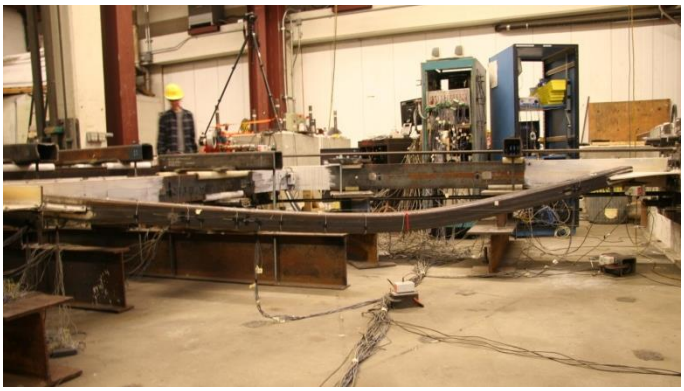

Figure 4.67: N brace buckling at +0.83% drift (B2).

4.4.3 Moderate Drift (1% < Story drift < 2%)

During the moderate drift cycles, the beam yielding continued to spread in the top and bottom flanges but did not reach the moderate yielding performance state. Other significant events during the moderate drift cycles included:

- At +1.4% drift, the columns began to yield in the plastic hinge region (Y1-OF)
- At ±1.4% drift and after, it was noted that at the center of the beam the top flange of the beam was not in contact with the center out-of-plane restraint at the peak displacements
- At ±1.93% drift, the columns experienced moderate yielding in the plastic hinge region (Y2-PH)
- At ±1.93% drift, very slight cupping began at the center of each brace (B3-PH)
- At -1.93% drift, a crack initiated in the toe of the SE corner brace-to-gusset weld (WT1)

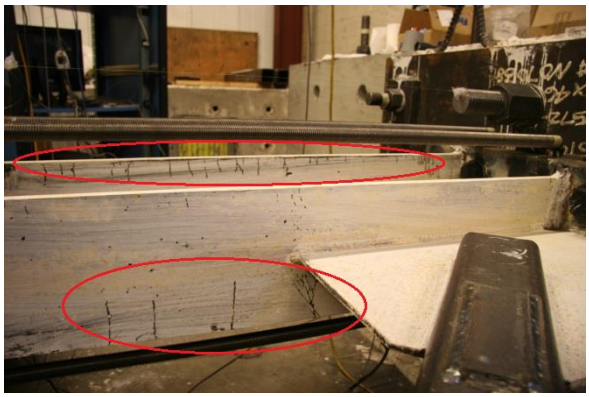

Figure 4.68: N col. initial yielding at 1.4% drift (Y1-OF/IF).

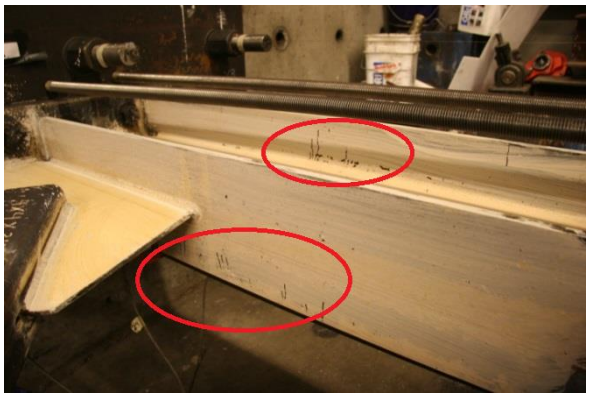

Figure 4.69: S col. initial yielding at 1.4% drift (Y1-OF/IF).

Figure 4.70: N col. moderate yielding at 1.9% drift (Y2-PH).

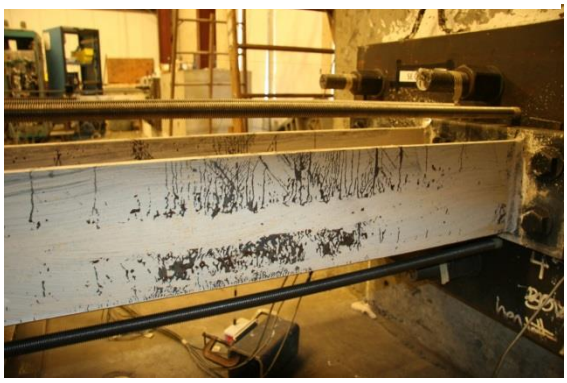

Figure 4.71: S col. moderate yielding at 1.9% drift (Y2-PH).

Figure 4.72: Beam OF yielding at 1.9% drift (Y1-OF).

Figure 4.73: Beam IF yielding at 1.9% drift (Y1-OF).

4.4.4 High Drift (Story drift > 2%)

At high story drifts there was tearing at the edge of all gusset-to-column and gusset-to-beam welds. Table 4.14 shows the progression of damage to these welds throughout the higher drift cycles. In addition to weld tearing, the following significant events occurred:

- At ±2.2% drift, the columns underwent initial local buckling of the flanges in the plastic hinge region (LB1-IF/OF)
- At ±2.48% drift, plate cracking was observed at both the North and South mid-span gusset-to-stiffener welds (PC1)
- At ±2.48% drift, slight cracking was observed at the toes of all brace-to-gusset welds (WT1 and PC1)
- At ±2.76% drift, the columns experienced severe yielding in the plastic hinge region (Y3-PH)
- At +3.03% drift, the South column experienced moderate local buckling (LB2-IF)
- At ±3.31% drift, the plate cracks at both the North and South mid-span gusset-to-stiffener welds went through the whole plate thickness (PC2)
- At ±3.31% drift, striation lines appeared in the center of each brace (B3-BT)
- At the first cycle of -3.31% drift, a 1” crack developed in the center of the North brace at the top inside corner (B3-BT)

- At the second cycle of -3.31% drift, the North brace tore 3/4 of the way through the cross-section, leaving only the bottom face of the brace intact (B3-BT)
- At the second cycle of -3.31% drift the North column experienced moderate local buckling (LB2-OF)
- At the second cycle of -3.31% drift the South column experienced severe local buckling in the outer flange (LB3-OF)
- At the first cycle of 3.58% drift, the South brace tore 3/4 of the way through the cross-section, leaving the bottom face of the brace intact (B3-BT)
- At the first cycle of -3.58% drift, the North brace fractured completely (B4-BF)
- At the second cycle of 3.58% drift, the South brace fractured completely; the frame was pushed to 3.9% drift to incite fracture (B4-BF)

Table 4.16 Chevron 3 Weld Crack Propagation

Half Cycle #	Drift (%)	N mid-span gusset-to-beam	S mid-span gusset-to-beam	NE gusset-to-column	SE gusset-to-column
53	2.21	1/2”	-	-	-
54	-2.21	1/2”	<1/4”	-	<1/4”
57	2.48	3/4”	<1/4”	-	<1/4”
61	2.76	1-1/4”	<1/4”	<1/4”	<1/4”
65	3.03	1-1/4”	<1/4”	1/4"	<1/4”
66	-3.03	1-1/4”	1/4"	1/4"	1”
69	3.31	2-1/2”	1/4"	1-1/2”	1”
70	-3.31	2-1/2”	1/4"	1-1/2”	2”
73	3.58	3”	1/4"	2-1/4”	2”

Figure 4.74: Initial S col. local buckling at +2.2% drift (LB1-IF/OF).

Figure 4.75: Initial N col. local buckling at 2.2% drift (LB1-OF/IF).

Figure 4.76: N col. severe yielding at 2.8% drift (Y3-PH).

Figure 4.77: S col. severe yielding at 2.8% drift (Y3-PH).

Figure 4.78: S brace cupping at 3.0% drift (B3-PH).

Figure 4.79: S col. moderate local buckling 3.0% drift (LB2-OF/IF).

Figure 4.80: Plate crack at N mid-span gusset-to-stiffener weld at 3.3% drift (PC2).

Figure 4.81: N brace crack/striations at -3.3% drift.

Figure 4.82: S col. severe local buckling at -3.3% drift (LB3-OF).

Figure 4.83: N brace ¾ tear at -3.3% drift (B3-BT).

Figure 4.84: N col. moderate local buckling at -3.3% drift (LB2-OF/IF).

Figure 4.85: S brace ¾ tear at 3.6% drift (B3-BT).

Figure 4.86: Shear tab moderate yielding at +3.3% drift (Y2).

Figure 4.87: Beam top flange moderate yielding at +3.3% drift (Y3-OF).

Figure 4.88: N brace fracture at -3.6% drift (B4-BF).

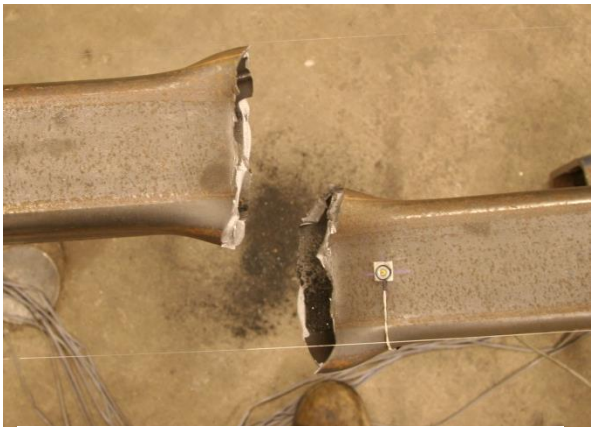

Figure 4.89: S brace fracture at +3.6% drift (B4-BF).

4.4.5 Post-Fracture Cycles

The frame was cycled to ±5% drift after both braces had fractured. The columns continued sustain yielding and local buckling, reaching the performance state of severe local buckling (LB3). After the test the frame was disassembled and it was noted that slight bolt hole elongation had occurred in the top and bottom holes in the beam web, as shown in Figure 4.90 and 4.91.

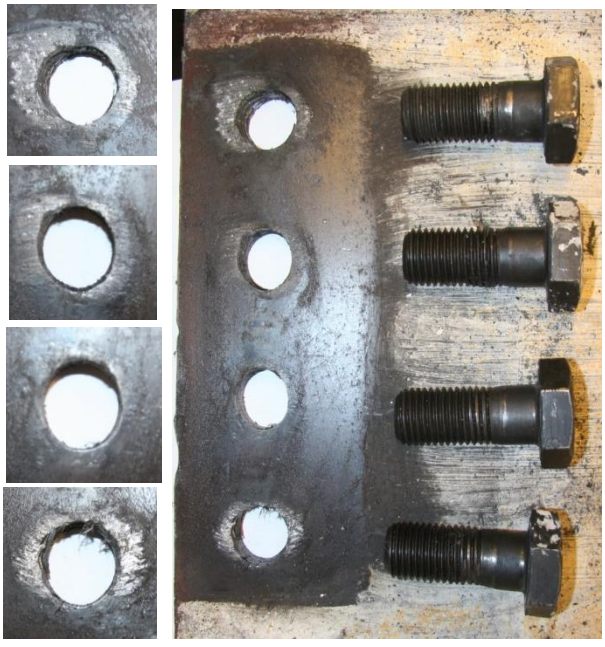

Figure 4.90: S beam web bolt hole elongation.

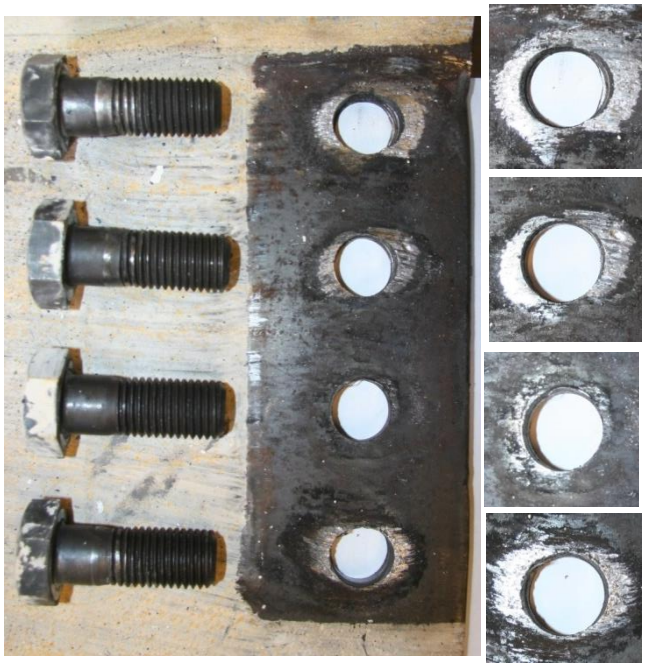

Figure 4.91: N beam web bolt hole elongation.

4.5 Specimen Comparisons

4.5.1 Comparison at ±1.4% Drift

Table 4.16 provides a comparison of the performance of the 3 specimens at 1.4% drift (2.8% drift range).

Behavior	Chevron 1	Chevron 2	Chevron 3
Max. Lateral Resistance	222 kips	195 kips	170 kips
Max. Beam Deflection	1.0 in.	1.2 in.	1.6 in.
Beam Performance State	n/a	Y1 	Y1 
Brace Performance State	B2 	B2 	B2 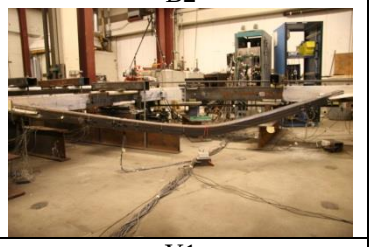
Column Performance State	Y1 	Y1 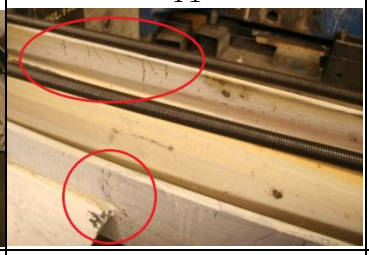	Y1 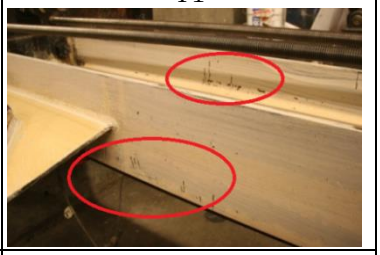
Gusset Plate Performance State	Corner - Y1* Mid-span – Y2* No picture	Corner - Y1 Mid-span – Y2 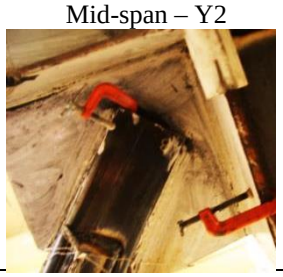	Corner - Y1 Mid-span – Y2 
Shear Tab Performance State	Y1 	Y1 	Y1 

Weld Crack Length	N mid-span GP-beam	--	1-1/2”	--
	S mid-span GP-beam	--	--	--
	N corner GP-column	--	--	--
	N corner GP-column	--	--	--

4.5.2 Comparison at ±2.5% Drift

Table 4.17 provides a comparison of the performance of the 3 specimens at 2.5% drift (5% drift range).

Behavior	**Chevron 1**	**Chevron 2**	**Chevron 3**
Max. Lateral Resistance	221 kips	206 kips	177 kips
Max. Beam Deflection	1.1 in.	1.7 in.	2.6 in.
Beam Performance State	n/a	Y1 	Y1 
Brace Performance State	B3-BC 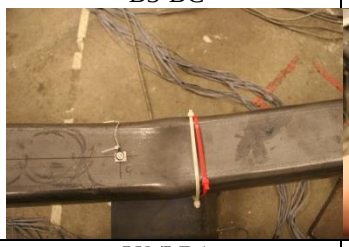	B3-BC 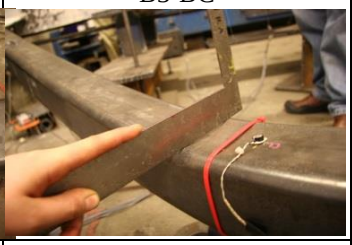	B3-BC 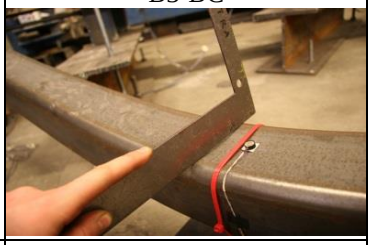
Column Performance State	Y2/LB1 	Y2/LB1 	Y2/LB1 
Gusset Plate Performance State	Corner – Y2* Mid-span – Y2*	Corner – Y2 Mid-span – Y2	Corner – Y2 Mid-span – Y2

		No picture		No picture
Shear Tab Performance State		Y1 	Y1 	Y1 
Weld Crack Length	N mid-span GP-beam	2”	4”	3/4”
	S mid-span GP-beam	--	2-1/2”	1/8”
	N corner GP-column	2”	1/4”	--
	S corner GP-column	1/2”	1/4”	1/8”

4.5.3 Comparison at End of Test

Table 4.17 provides a comparison of the performance of the 3 specimens at the end of each test. Note that this is a drift range of 6.3%, 6.6%, and 7.2%, for Chevron 1, 2, and 3, respectively.

Behavior	**Chevron 1**	**Chevron 2**	**Chevron 3**
Max. Lateral Resistance	233 kips	207 kips	177 kips
Max. Beam Deflection	1.1 in.	1.8 in.	3.0 in.
Beam Performance State	n/a	Y1 	Y2 
Brace Performance State	B4-BF 	B4-BF 	B4-BF 
Column Performance	Y3/LB2	Y3/LB1	Y3/LB3

State				
Gusset Plate Performance State		Corner – Y2* Mid-span – Y2*	Corner – Y2 Mid-span – Y2	Corner – Y2 Mid-span – Y2
Shear Tab Performance State		Y1 	Y1 	Y2 
Weld Crack Length	N mid-span GP-beam	4”(WT3)	5-1/2”(WT3)	3” (WT2)
	S mid-span GP-beam	1-1/2”(WT2)	4”(WT3)	1/4” (WT1)
	N corner GP-column	5”(WT3)	3”(WT2)	2-1/4” (WT2)
	S corner GP-column	1/2”(WT1)	3-1/2”(WT2)	2”(WT2)

Chapter 5

Data Analysis

5.0 Introduction

This chapter describes the processing and analysis of the data collected during the experiments. The results of this analysis are used to gain a deeper understanding of the behavior of the specimens. The specimen performance is compared for both global and local behaviors. Section 5.1 describes the processing of raw data obtained from the instruments. A comparison of the overall force-drift behavior of the specimens is presented in Section 5.2. The performance of the braces, beams, columns, and connections is discussed in Sections 5.3 through 5.6. Finally the energy dissipation capacity of the specimens is compared in Section 5.7. These results are used in Chapter 6 to develop conclusions and recommendations for future work on chevron beam strength.

5.1 Processing Raw Data

5.1.2 Processing LabView Data

Data was collected from the actuator, potentiometers, and strain gauges using the National Instruments Data Acquisition System and LabView software. The instruments were continuously sampled with a frequency of 1 Hertz, including during the periods where loading was paused for several minutes at the peak displacements to document damage. This resulted in very large data sets which included some erroneous spikes. A Matlab script (Ballard, 2015) was used to filter out the spikes in the data and to remove data during test holds. Figure 5.1 compares the raw LabView data to the processed LabView data.

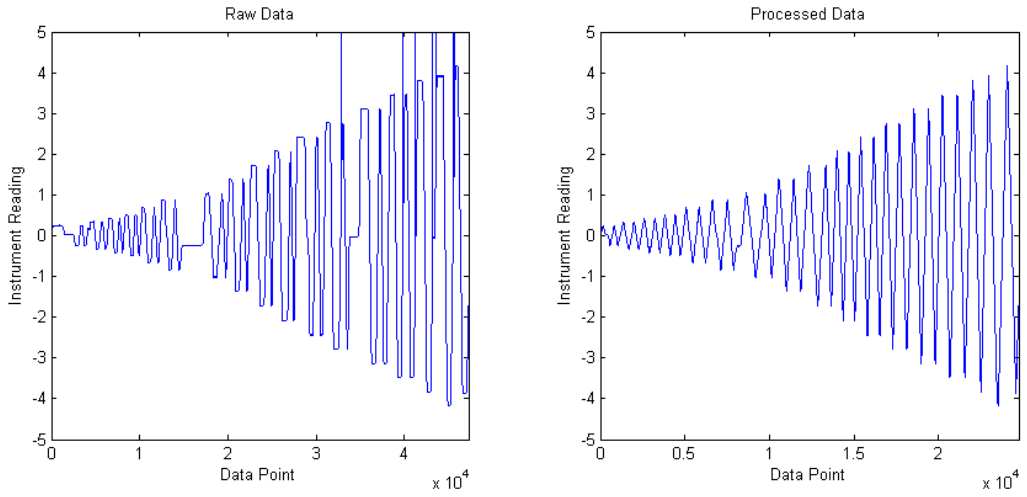

Figure 5.1: Raw vs processed LabView data.

5.1.2 Processing Optotrak Data

The Northern Digital Inc. First Principles software was used to collect the Optotrak data. The x-,y-,and z-displacement of each LED marker was recorded based on an arbitrary Cartesian coordinate system. The data was transformed into a relevant Cartesian coordinate system with the x-axis oriented along the beam bottom flange. Figure 5.2 shows the original and transformed x-y coordinate systems. Details of the coordinate system transformation can be found in Ballard (2015).

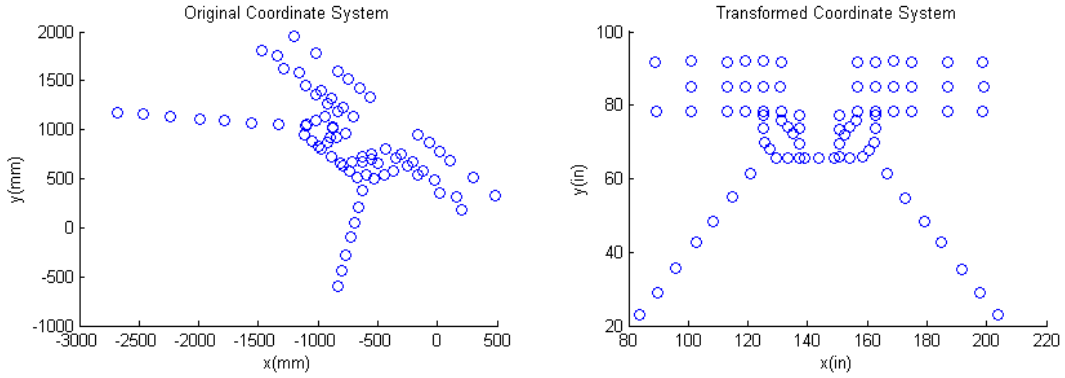

Figure 5.2: Original vs transformed Optotrak coordinate system.

In an attempt to match the LabView data, Optotrak measurements were taken at a 1 Hertz frequency and data collection was started at the exact same time for both programs. Despite these measures, the unreduced Optotrak data did not match up in time with the unreduced LabView data because the sampling

rate was slightly faster in the Optotrak system. A Matlab script was used to remove the necessary number of points from the raw OptoTrak data so that it matched the raw LabView data. The Matlab script is provided in Appendix 3. Figure 5.3 shows a comparison of a measurement from the two data sets before and after removing points from the Optotrak data.

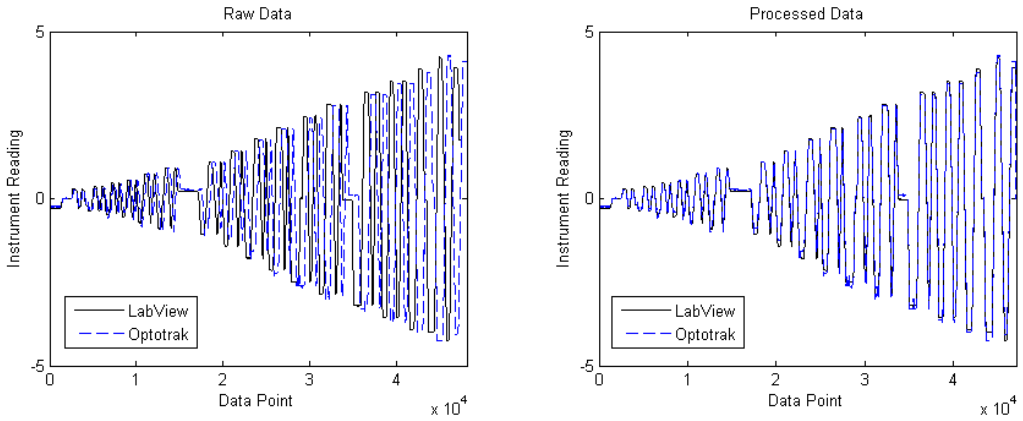

Figure 5.3: OptoTrak and LabView data matching.

5.1.3 Comparing Optotrak and LabView Data

In order to verify the accuracy of the instruments, Optotrak readings were compared to LabView readings for displacements that were captured by both systems. Figure 5.4 show a comparison of frame lateral displacement versus time for the Optotrak and LabView systems. The LabView displacement was taken from one of the two string potentiometers used to measure frame drift. The Optotrak displacement was taken from a marker on the mid-span gusset plate. The measurements match well, giving confidence to both the LabView and Optotrak lateral displacement measurements.

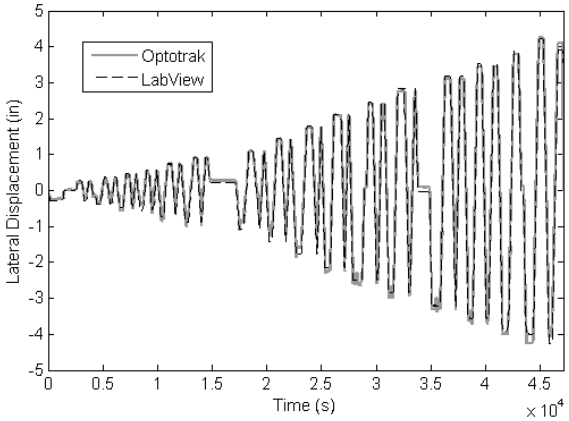

Figure 5.4: OptoTrak and LabView frame lateral displacement comparison.

The vertical beam deflection at mid-span was also compared, as shown in Figure 5.5. The LabView displacement came from a string potentiometer connected to the bottom edge of the midspan gusset plate in line with the center of the beam. The Optotrak displacement came from a marker on the mid-span gusset plate right next to where the string potentiometer was attached. Both measurements were plotted versus drift from potentiometer data.

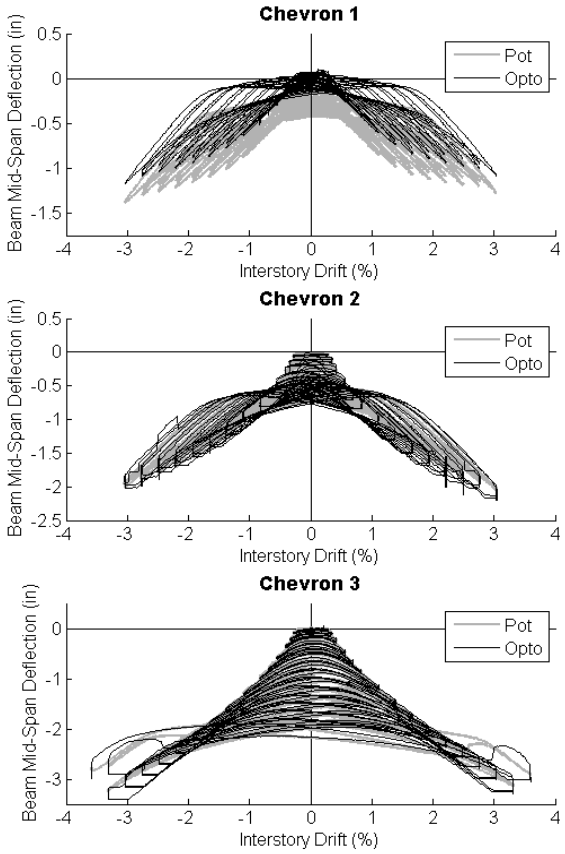

Figure 5.5: Optotrak vs Potentiometer Beam Deflection

For Chevron 2 and 3 the measurements match well, however for Chevron 1 there is a consistent discrepancy of around 1/4 inch. It is not clear which measurement is more accurate for Chevron 1. The potentiometers have a greater potential for error than the Optotrak data because they are attached to stands which can be nudged inadvertently during testing and are attached to the computer via long wires that can be stepped on or pulled. However there were indications from other measurements that suggest the potentiometer deflection could be correct. As mentioned in Section 3.3.2, column shortening was not directly measured for Chevron 1 but was likely to have occurred because there was loss of tension in the rods used to post-tension the columns. In Chevron 2 and 3, column shortening was directly measured and found to average 0.3 inches by the end of each test, and is assumed to be of a similar magnitude for

Chevron 1. This extra 0.3 inches of beam vertical deflection due to column shortening would be captured in the beam vertical deflection measurements pictured in Figure 5.4, however the Optotrak measurement for Chevron 1 shows a maximum residual deflection of only 0.2 inches. For this reason, the beam deflection data from the string potentiometer is used in the beam deflection plots in Section 5.4.

5.1.4 Verification of Member Forces

In order to verify that the forces determined from the strain gauge data were correct, various equilibrium checks were made. Appendix 3 contains the results of these studies. Forces measured by multiple sets of strain gauges were compared and found to match well with one exception - the total vertical load on the beam in Chevron 3. The vertical component of the braces forces was found to be 40% higher than the vertical load on the beam measured from the beam strain gauges. As discussed in Section 5.4.1, the higher vertical force measured by the brace strain gauges is more consistent with the observed behavior of the beam in Chevron 3.

5.2 Force-Drift Behavior

Frame interstory drift was calculated using readings from two string potentiometers attached to the outside flanges of the columns at the beam centerline, as described in Section 3.3.2. The displacement from the string potentiometers was averaged and then divided by the distance from the beam centerline to the base of the columns to calculate frame interstory drift. This measurement was also corroborated Optotrak data as described in the previous section.

$$\Delta_{interstory} = \frac{\delta_{lateral}}{H_{story}}$$

Where

$\delta_{lateral}$ = x-direction displacement measured at beam centerline

H_{story} = story height measured from beam centerline to base of column

The base shear was determined from the actuator's internal load cell, which had been calibrated just before the first test. Figure 5.6 shows a comparison of the force-drift hystereses for the three specimens and Figure 5.7 shows a comparison of the backbone curves for the force-drift behavior. The lateral force is normalized by the design strength of the frames, taken as twice the horizontal component of the expected brace buckling load, $2P_{cr}\cos\theta$. Figure 5.8 shows the force-drift behavior for the post-fracture cycles, also normalized by the design strength. Table 5.1 records key values from the force-drift hysteresis.

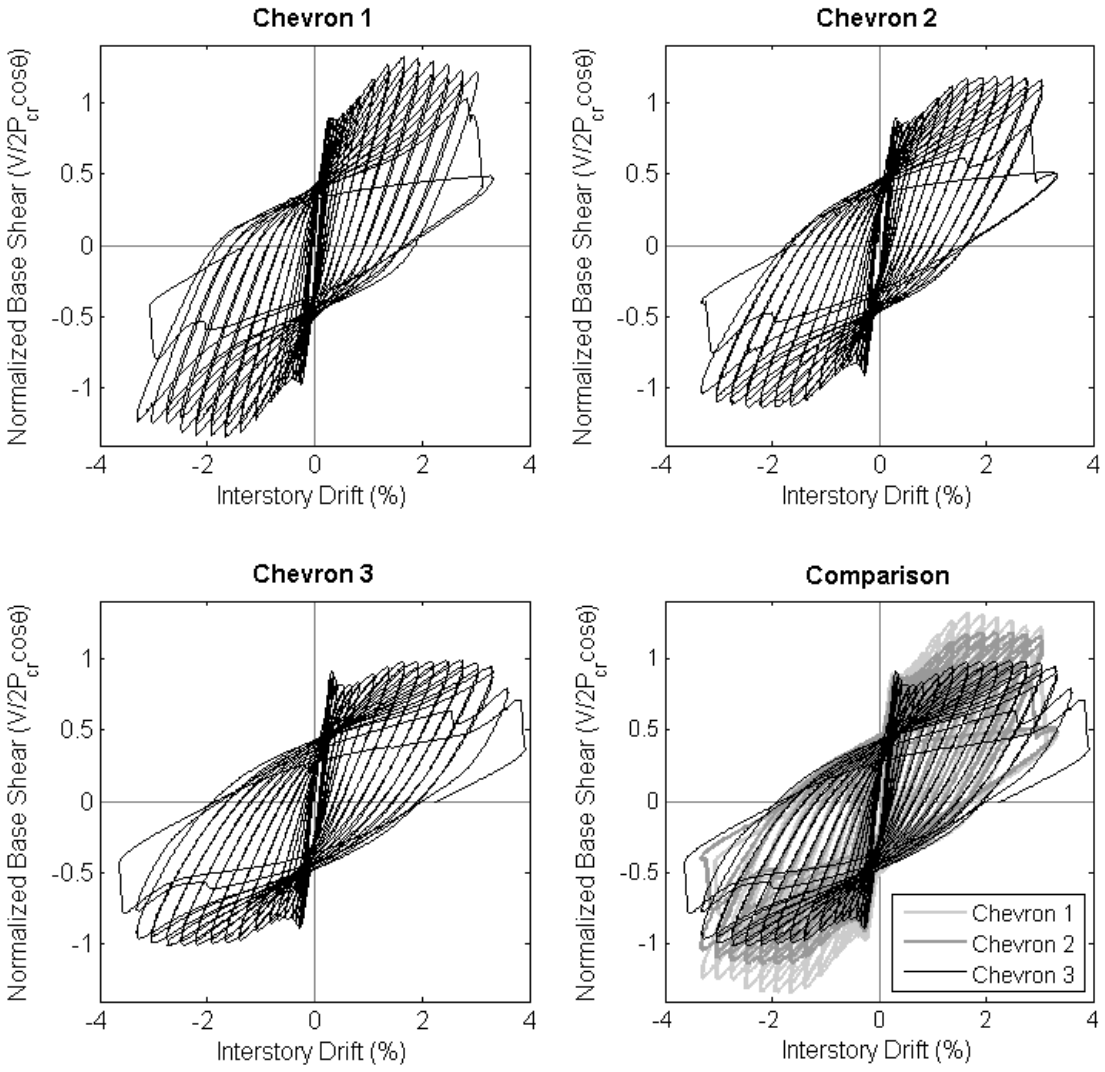

Figure 5.6: Base shear-drift hystereses for main cycles.

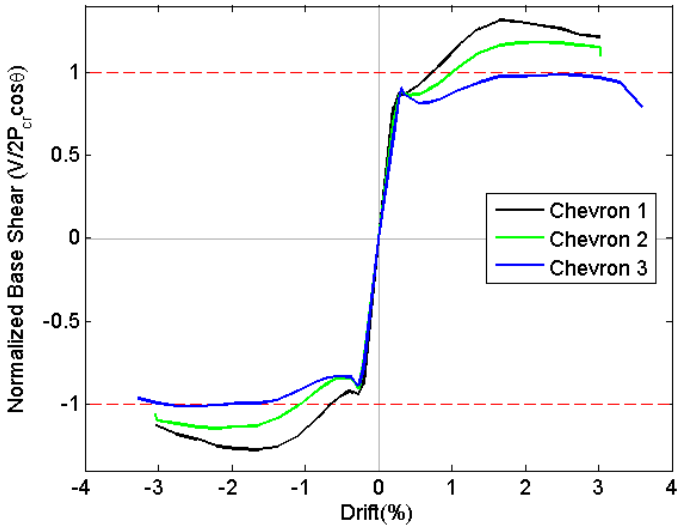

Figure 5.7: Base shear-drift backbone curve comparison.

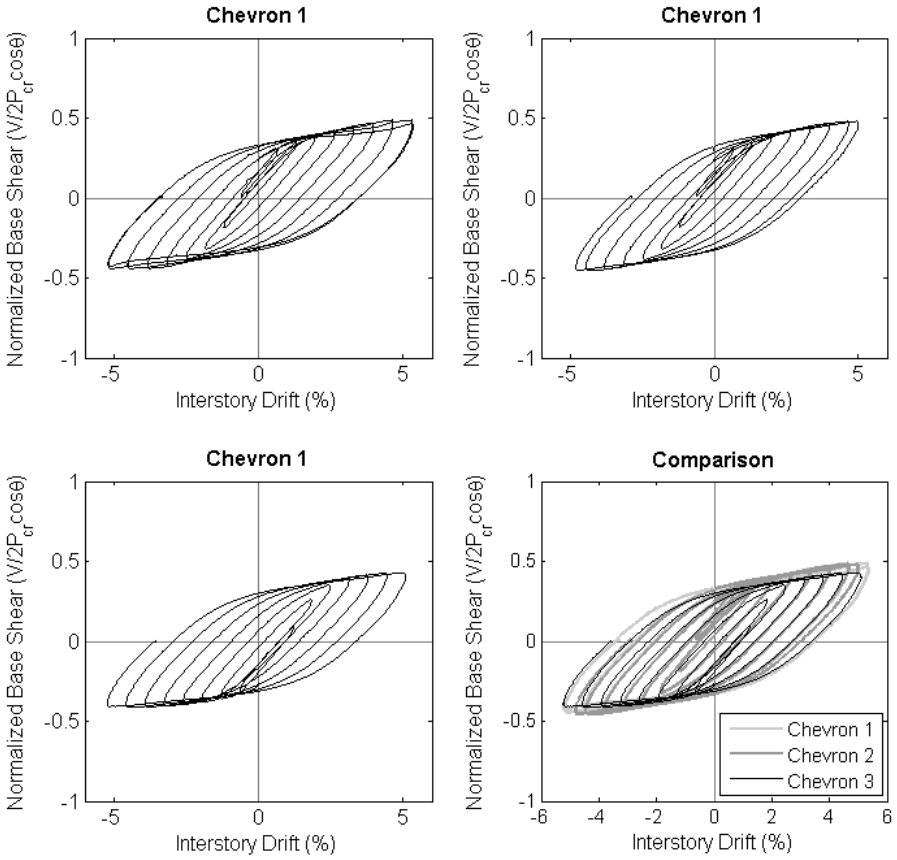

Figure 5.8: Base shear-drift hystereses for post-fracture cycles.

Table 5.1 Force-Drift Response Summary

Specimen	Beam DCR	Max. Lateral Resistance/ $2P_{cr}\cos\theta$	Drift at 1st Brace Fracture	Drift at 2nd Brace Fracture	Max. Drift Range	Initial Stiffness*	Brace lateral stiffness $2(AE/L)\cos^2\theta$
Chevron 1	0.83	1.34	3.0%	-3.3%	6.3%	513 k/in.	800 k/in.
Chevron 2	1.72	1.18	3.3%	-3.3%	6.6%	448 k/in.	800 k/in.
Chevron 3	2.67	1.01	-3.6%	3.6%	7.2%	376 k/in.	800 k/in.

*Calculated from the force and displacement at the first peak

Decreasing beam strength was associated with decreased strength and stiffness of the frames; however all of the frames reached or exceeded the design strength. Chevron 3 had a maximum resistance of almost exactly $2P_{cr}\cos\theta$, while Chevron 1 and 2 had a maximum resistance 33% and 18% larger than $2P_{cr}\cos\theta$, respectively. This difference in resistance is due to the fact that the weaker beams could not develop as much tensile force in the braces, as discussed in Section 5.4.

All of the frames exhibited high ductility and were able to achieve the expected failure mode of brace fracture without any significant drops in lateral resistance. The specimens with non-compliant beams exhibited greater ductility than the full strength specimen. Chevron 3 had a maximum drift range of 7.2% compared to 6.6% in Chevron 2 and 6.3% in Chevron 1. This is also a result of the weaker beams not developing as much tensile force and strain in the braces. Severe local deformation at the center of the brace during out of plane buckling eventually leads to tearing and fracture of the brace in tension. Although a weaker beam may cause earlier concentration of deformation at the center of the braces due to increased beam deflection, the weaker beam is unable to develop enough tensile force in the brace to cause fracture until higher drifts. This phenomenon was exemplified in Chevron 3, where both braces tore through ¾ of the cross section at the second cycle of ±3.3% drift but were able to make it through another tension cycle before finally fracturing at ±3.6% drift.

The force-drift behavior of the frames in the post-fracture cycles was quite similar. Due to the use of pinned beam-column connections, the lateral resistance after brace fracture was primarily provided by the columns. The same columns were used in each frame and were subjected to the same displacement history, so they provided a similar magnitude of lateral resistance at a given drift level.

5.3 Brace Performance

5.3.1 Brace Out-of-Plane Deformation

The brace out-of-plane (OOP) deflection was taken from Optotrak LEDs placed on the top half of each brace. In each test, some of the LED markers near the center of one of the braces moved outside of the viewing range of the Optotrak camera. In those instances the brace OOP deflection at mid-span had to be extrapolated from the visible markers as shown in Figure 5.9. Note that the applied correction is only accurate for a linear brace deflected shape. However the markers only went out of range at relatively high drifts, after the brace had begun to form a plastic hinge at the center and deflected in a roughly linear shape as shown in Figure 5.10. Figure 5.11 compares the brace deflected shape in the 3 tests, and Figure 5.12 shows a backbone curve of the brace OOP deflection at mid-span versus drift. For these figures, the one brace that had all LED markers in view throughout the entire test was used.

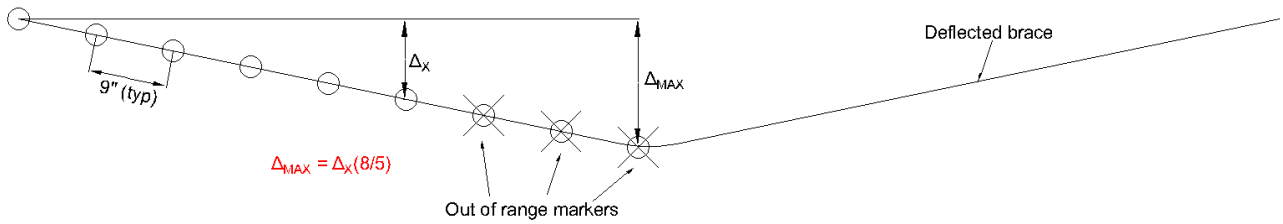

Figure 5.9: Brace OOP deformation extrapolation for out of range markers.

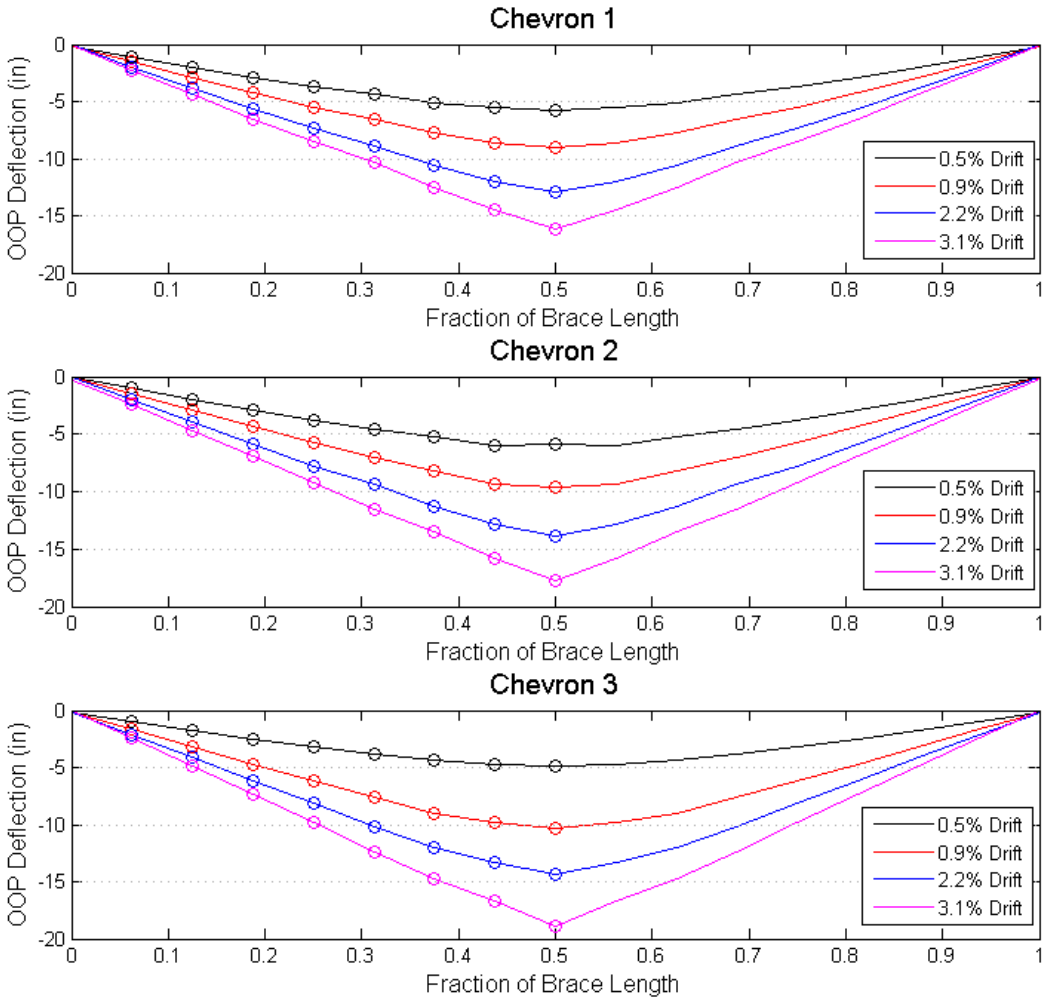

Figure 5.10: Brace deflected shape at 0.5, 0.9, 2.2 and 3.1% drift.

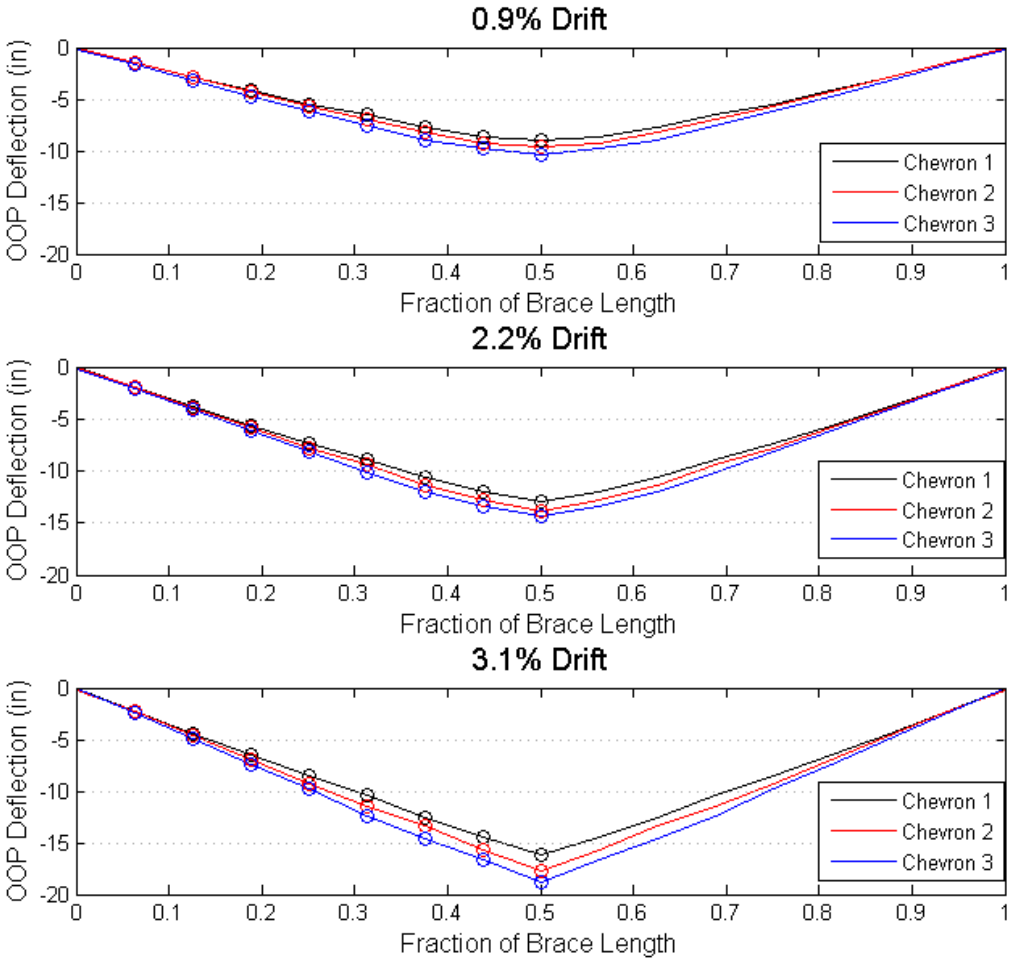

Figure 5.11: Brace deflected shape comparison.

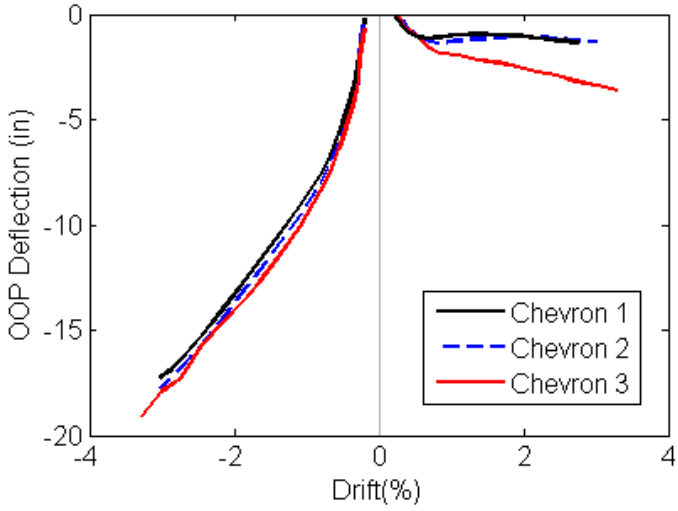

Figure 5.12: South brace OOP deflection at mid-span vs. drift.

Table 5.2 Brace out-of-plane deformation summary.

Specimen	Max. brace out of plane deformation
Chevron 1	-17.3 in.
Chevron 2	-17.8 in.
Chevron 3	-19.6 in.

The braces deflected farther out of plane with decreasing beam strength. This is consistent with the increased beam deflection observed in Chevron 2 and 3, as described in Section 5.4.1. Deformation compatibility requires that increased beam deflection be correlated with greater shortening of the compressive brace and less elongation of the tensile brace. Table 5.2 shows the maximum brace OOP deformation at mid-span of the brace. The braces in Chevron 3 reached a significantly higher maximum out-of-plane deformation than the braces in Chevron 1 and 2, however this did not result in earlier brace fracture – Chevron 3 reached the largest drift levels of the three specimens. As shown in the positive drift portion of Figure 5.11, the braces in Chevron 3 did not straighten out as much during the tension cycles as in Chevron 1 and 2. This was also a result of the larger beam deflections observed in Chevron 3.

5.3.2 Brace Axial Force vs Elongation

The brace axial elongation was determined from string potentiometers attached in line with the brace, as shown in Figure 5.14. One potentiometer was connected directly to the brace ends while the other was attached to the beam and column flanges parallel to the brace, as shown in Figure 5.12. The potentiometer attached directly to the brace ends rotated with the brace due to how it was connected, which introduced an error in the measurement during out of plane buckling. For this reason, the string potentiometers attached to the framing members were used for the brace axial elongation. Note that this measurement includes any elongation or shortening contributed by the gusset plates, however this is expected to be small relative to the contribution from the braces.

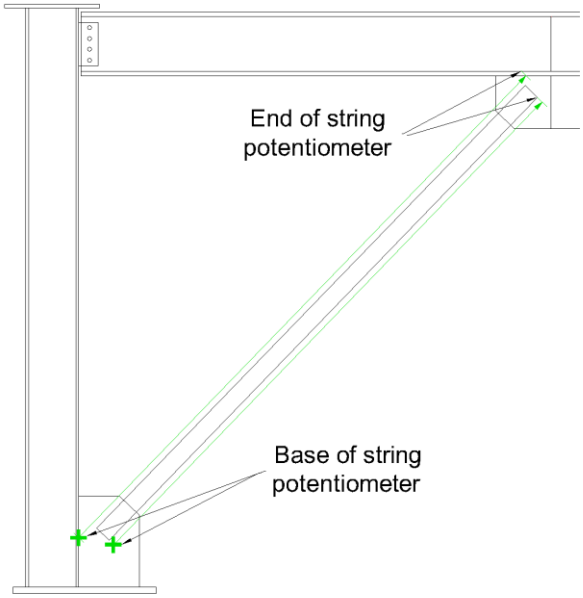

Figure 5.13: Brace elongation potentiometers.

Brace axial force was determined using 3 sets of strain gauges on each brace. Each set comprised of 4 gauges – one on each wall of the brace. There was yielding at some gauge locations, so the strain history from each gauge was run through a bilinear hysteretic material model to determine the stress history at each gauge location. The stresses determined from the 4 gauges in the set were then averaged to find the net axial force on the cross-section. The net axial forces from each of the 3 sets of gauges were averaged to get the brace axial force. The brace forces were compared with the expected tensile and compressive strength determined from coupon tests of the brace material. Figure 5.14 and 5.15 show the axial force-elongation hystereses for the South and North brace, respectively, normalized by the brace buckling strength. Figures 5.16 and 5.17 show backbone curves for the same behaviors. Table 5.3 documents the minimum and maximum axial force and elongation values through first brace fracture.

Table 5.3 Brace Axial Force and Elongation Summary

Specimen	Brace	Max. Tensile Force	Max. Tensile Elongation	Max. Compressive Force	Max. Compressive Shortening
Chevron 1	S	249 kips	1.7 in.	-137 kips	-3.7 in.
	N	242 kips	1.6 in.	-133 kips	-3.6 in.
Chevron 2	S	192 kips	0.97 in.	-134 kips	-4.1 in.
	N	187 kips	0.90 in.	-124 kips	-4.1 in.
Chevron 3	S	128 kips	0.41 in.	-116 kips	-5.3 in.
	N	123 kips	0.36 in.	-132 kips	-5.1 in.

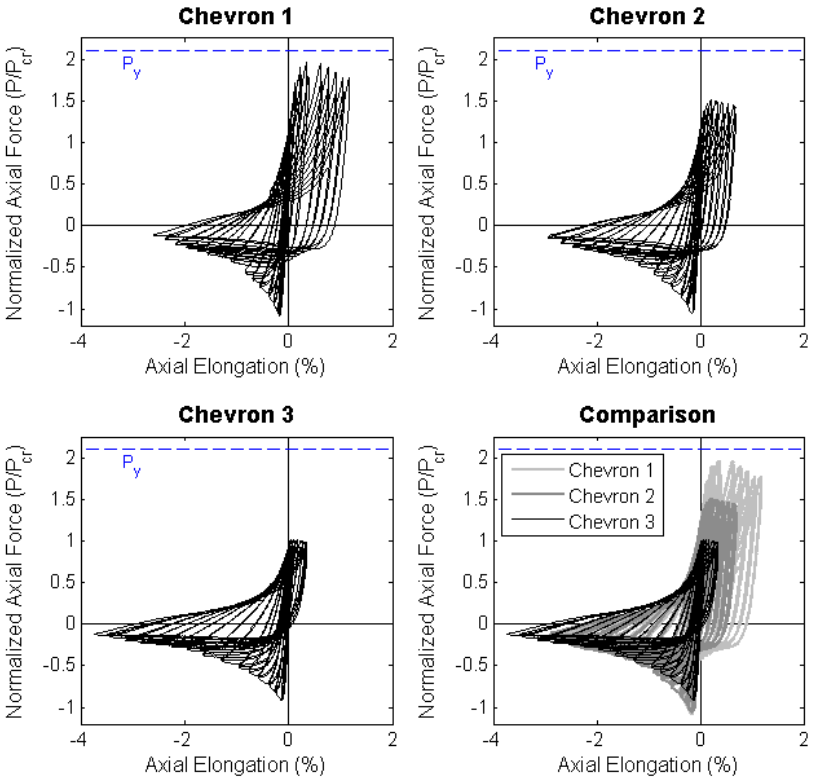

Figure 5.14: South brace axial elongation vs axial force.

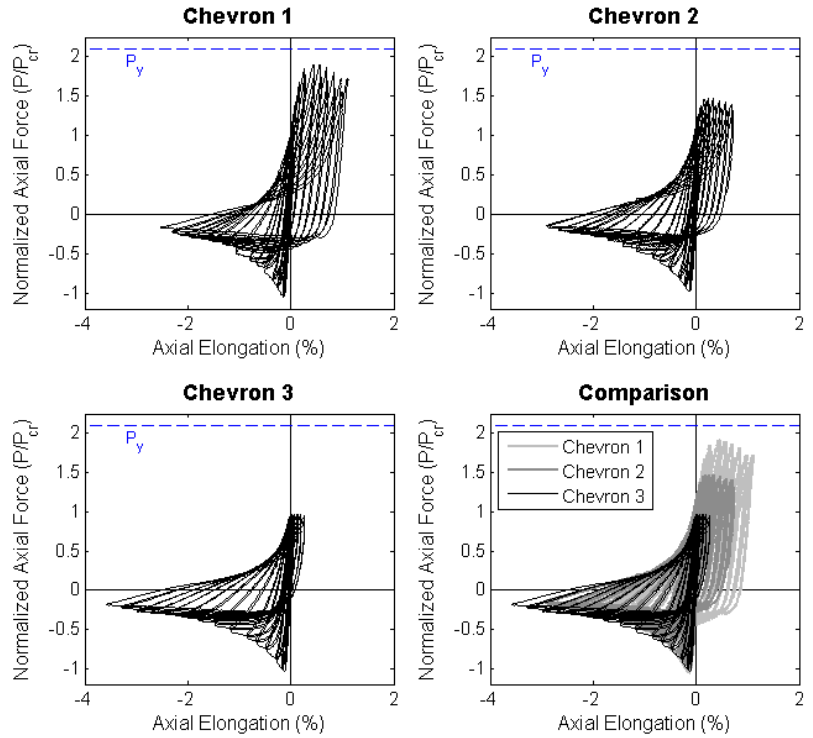

Figure 5.15: North brace axial elongation vs axial force.

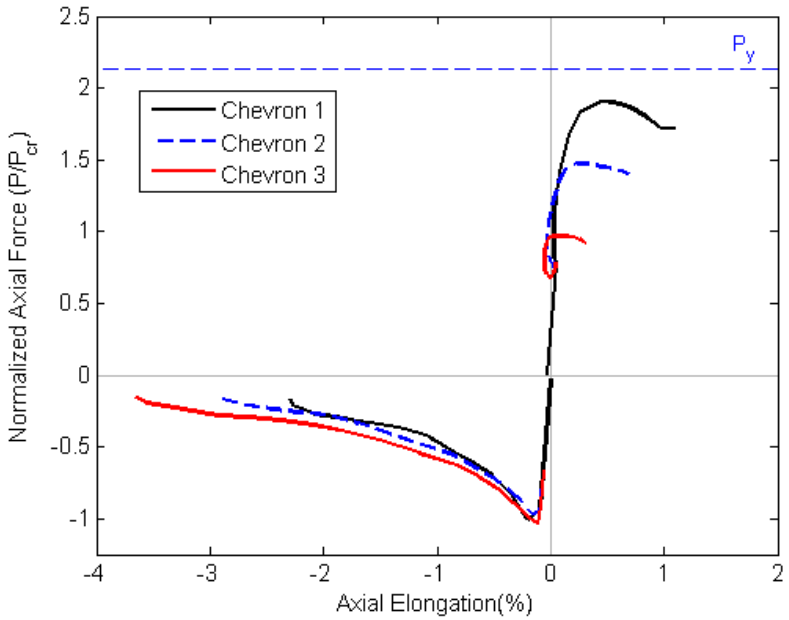

Figure 5.16: South brace axial elongation vs axial force backbone curve.

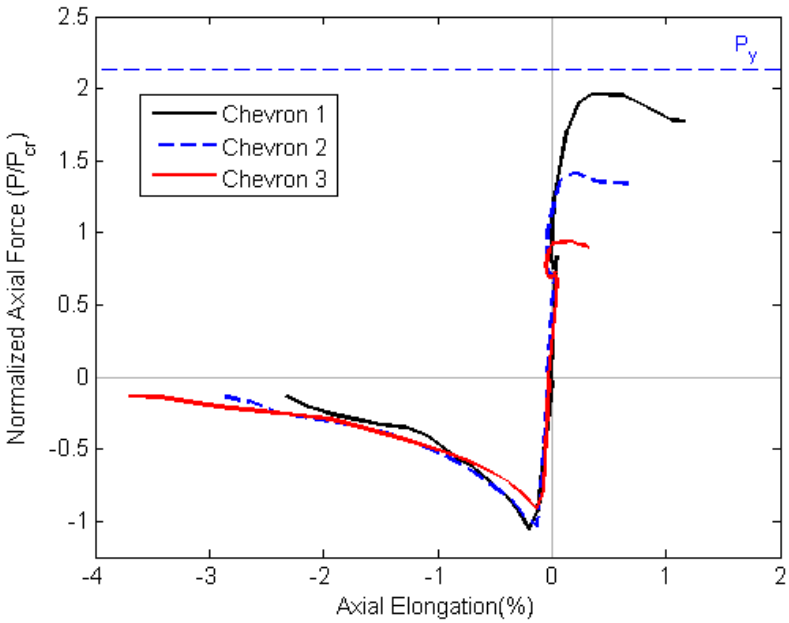

Figure 5.17: North brace axial elongation vs axial force backbone curve.

The use of weaker beams led to more compression-dominated brace behavior. The braces shortened more in compression and elongated less in tension due to the increased beam deflection observed in Chevron 2 and 3. In each test, the compressive brace strength degraded to even less than $0.3P_{cr}$, the strength used for the compression brace when computing the unbalanced load. The tensile force in the braces tended to peak relatively quickly and then remained stable for the remainder of the test. The braces did not reach their expected yield strength in tension, even in the full strength specimen; however this does not mean tensile yielding did not occur in the braces. There were individual strain gauges that did reach the yield strain, but the gross section did not yield at any of the sets of strain gauges. There were no gauges located at the middle of the brace where gross section yielding might have occurred.

5.4 Beam Performance

5.4.1 Beam Shear, Axial, and Flexural Demand

Four pairs of strain gauges were used to compute the shear, flexural, and axial demand on the beam as shown in Figure 5.18.

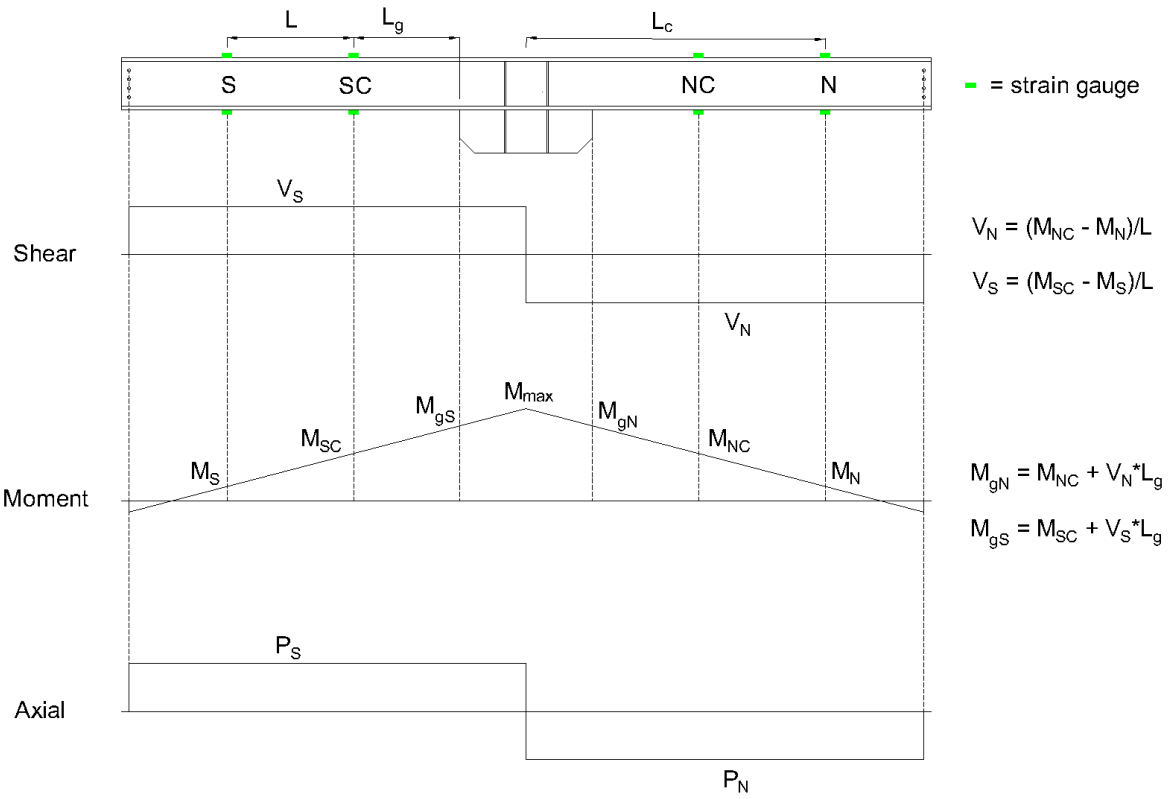

Figure 5.18: Beam shear, moment, and axial force determination.

There was no yielding at any of the beam gauge locations, thus the stress at a gauge was determined by simply multiplying the strain by the elastic modulus. The axial load and moment at each pair of gauges was found using the following equations:

$$P = A\left(\frac{\sigma_i + \sigma_j}{2}\right)$$

$$M = S_x\left(\frac{\sigma_i - \sigma_j}{2}\right)$$

where

P = Axial force at a strain gauge pair

M = Bending moment at a strain gauge pair

$\sigma_{i,j}$ = The stresses determined from the gauges on the top and bottom flange, respectively

S_x = elastic section modulus

Figure 5.19 shows the shear demand on each half of the beam versus interstory drift. Note that the sign of the shear force for the north half of the beam is reversed to make it easier to compare the magnitude of the shear force on each half of the beam. The shear is not distributed exactly equally to each half of the beam; when the frame is being pushed to the North (positive drift), the North half of the beam tends to take slightly more of the total force. The reciprocal is true for negative drifts. This corresponds with the side of the beam in tension taking more force than the side of the beam in compression.

Figure 5.20 shows the total vertical unbalanced load on the beam, calculated by adding the shear on each half of the beam. The vertical load is normalized by design unbalanced vertical load of 165 kips, which was not reached in any of the tests. This is consistent with the beam being unable to develop the tensile yield force in the brace. The weaker beams were able to develop significantly less force in the braces and thus there was a drop in shear demand in Chevron 2 and 3. Consistent with the pattern in brace forces, the shear demand on the beam tends to peak by ±1% drift and then plateau for the remainder of the test.

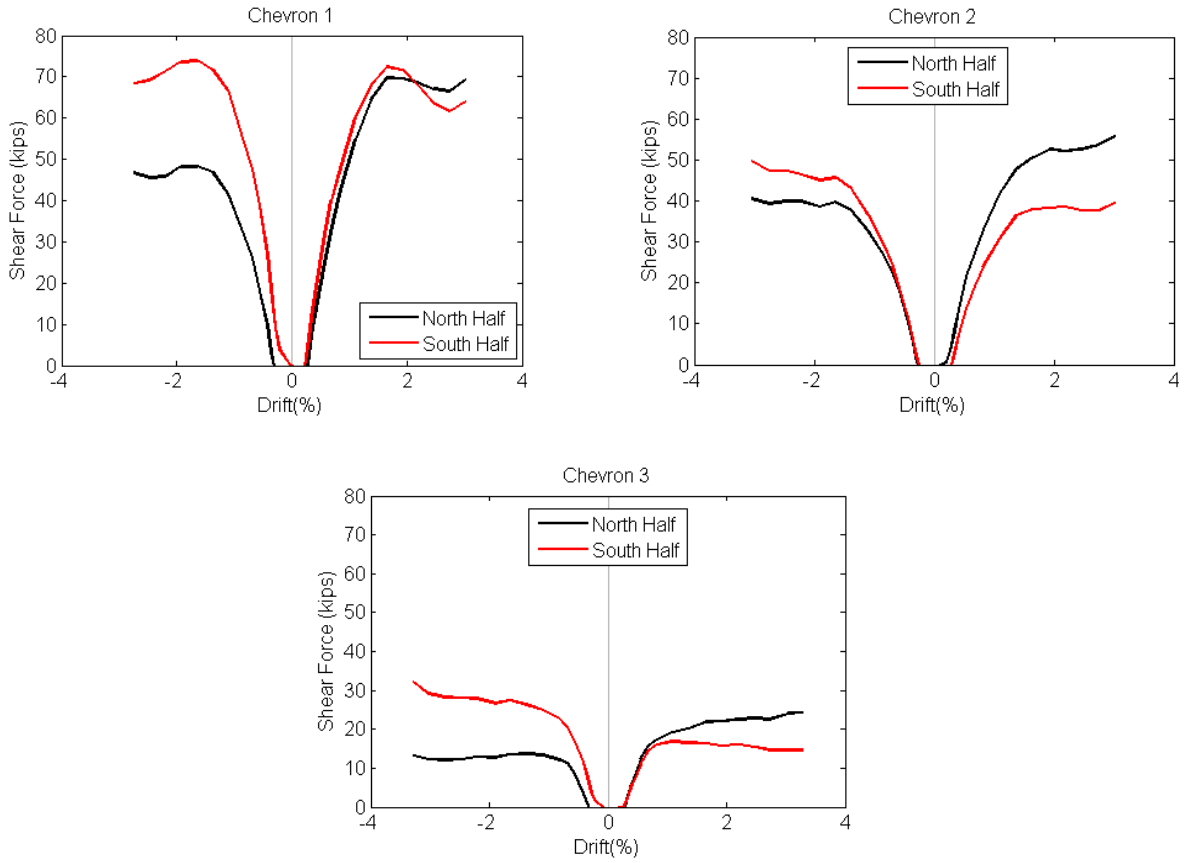

Figure 5.19: Shear force on North and South half of beam.

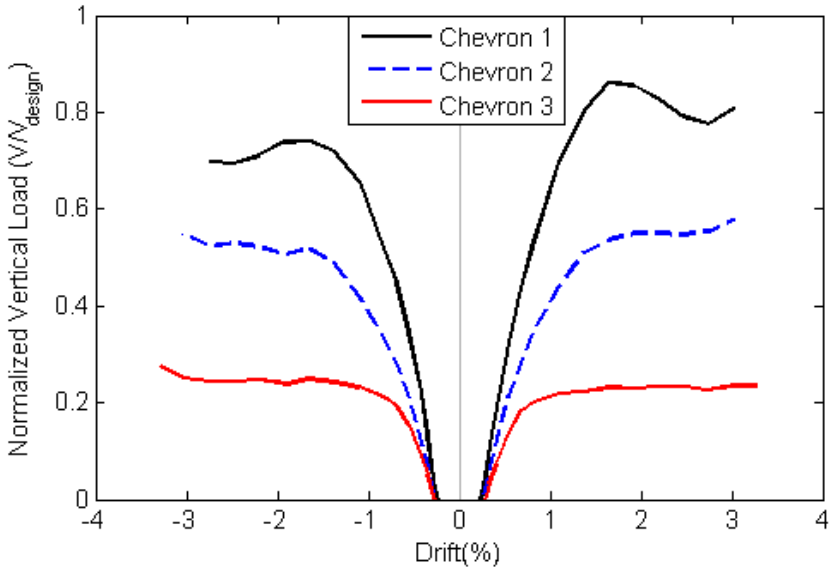

Figure 5.20: Normalized total beam vertical load.

Figure 5.21 shows the axial demand on each half of the beam versus drift. Consistent with the shear force distribution, the force demand tends to concentrate on the tension side of the beam. Figure 5.22 shows the total horizontal load on the beam versus drift, normalized by the horizontal component of the design unbalanced load of 211 kips. The maximum measured axial load in the beam was used to compute a reduced beam plastic moment capacity, M_p*, by rearranging the interaction equations used to design the beam:

(a) When $\frac{P}{P_c} \geq 0.2$

$$M_p^* = \left((1.0 - \frac{P}{P_c})\frac{9}{8}\right) M_p \qquad \text{Eq. 5.1a}$$

(b) When $\frac{P}{P_c} < 0.2$

$$M_p^* = \left(1.0 - \frac{P}{2P_c}\right) M_p \qquad \text{Eq. 5.1b}$$

Where

P = measured maximum axial load in beam

P_c = axial capacity of beam from measured material properties

M_p = plastic flexural capacity of beam from measured material properties

A reduced yield moment, M_y*, was also computed using the axial stress in the beam:

$$M_y^* = (\sigma_y - \frac{P}{A})S_x \qquad \text{Eq. 5.2}$$

The moment in the beam at the North and South edge of the mid-span gusset plate is plotted versus interstory drift in Figure 5.23. The moment is normalized by the reduced plastic moment capacity, M_p*. As shown in the figures, the plastic moment capacity of the beam was not reached in any of the tests according to the beam strain gauge data, and the reduced yield moment was barely reached in Chevron 2 and 3. This is inconsistent with the level of observed yielding during the tests. As mentioned in Section 5.1.4, the total vertical load on the beam in Chevron 3 determined from the axial forces in the braces was significantly higher than the total vertical load on the beam calculated by adding the shear on each half of the beam. Figure 5.25 shows a comparison of the beam flexural demand at the edge of the mid-span gusset calculated with the beam and brace data. The moments calculated using the brace vertical force are more consistent with the level beam yielding observed during the test, so it assumed that the flexural demand calculated based on the brace data is more accurate. The beam in Chevron 2 reached M_y* at approximately 1.5% drift and reached M_p* by the end of the test. The beam in Chevron 3 reached M_y* at approximately 1.25% drift and reached M_p* by 2% drift.

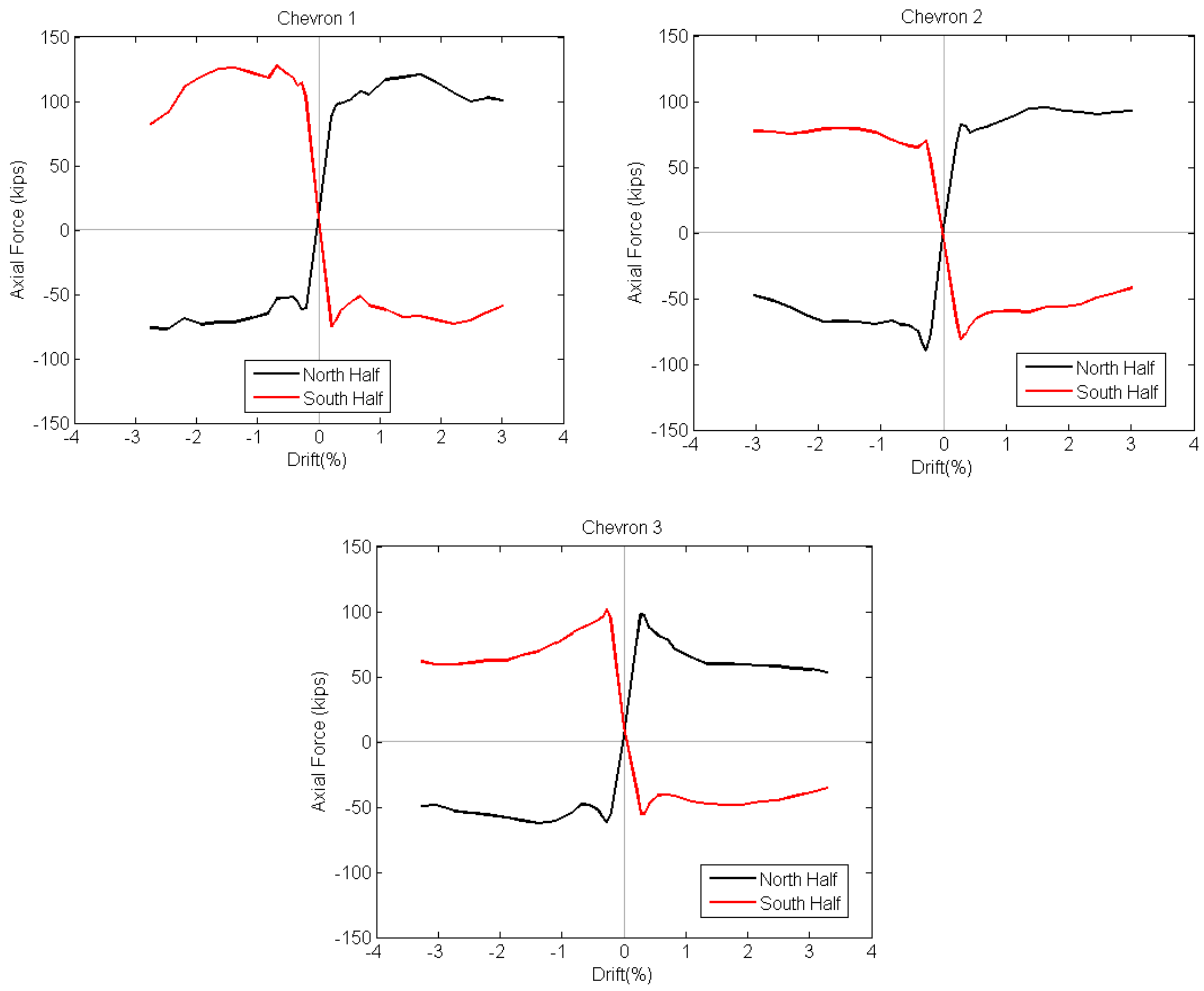

Figure 5.21 Beam axial demand on N and S side vs. interstory drift.

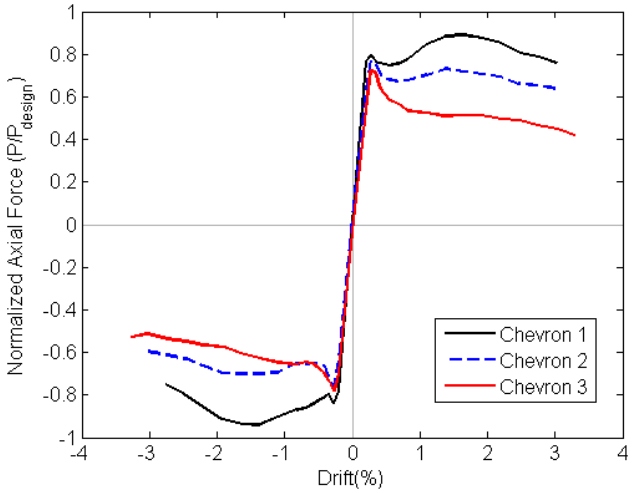

Figure 5.22. Normalized beam total horizontal force versus drift.

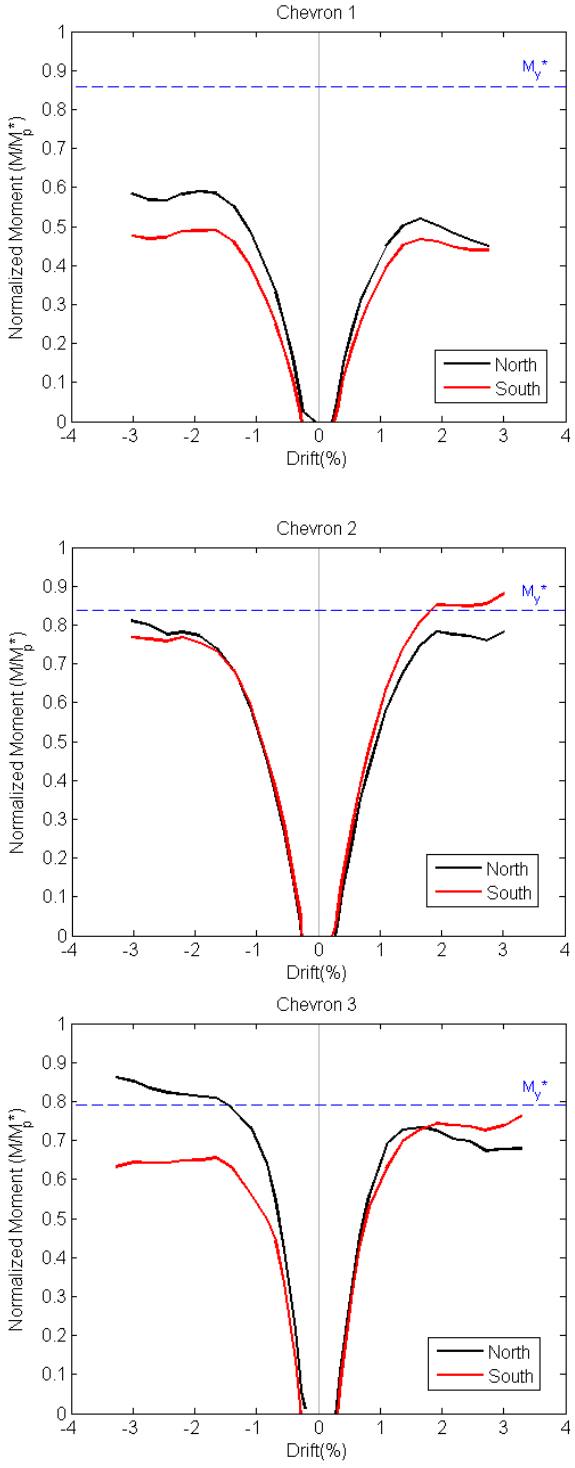

Figure 5.23: Beam flexural demand at N and S edge of mid-span gusset plate calculated from beam gauges.

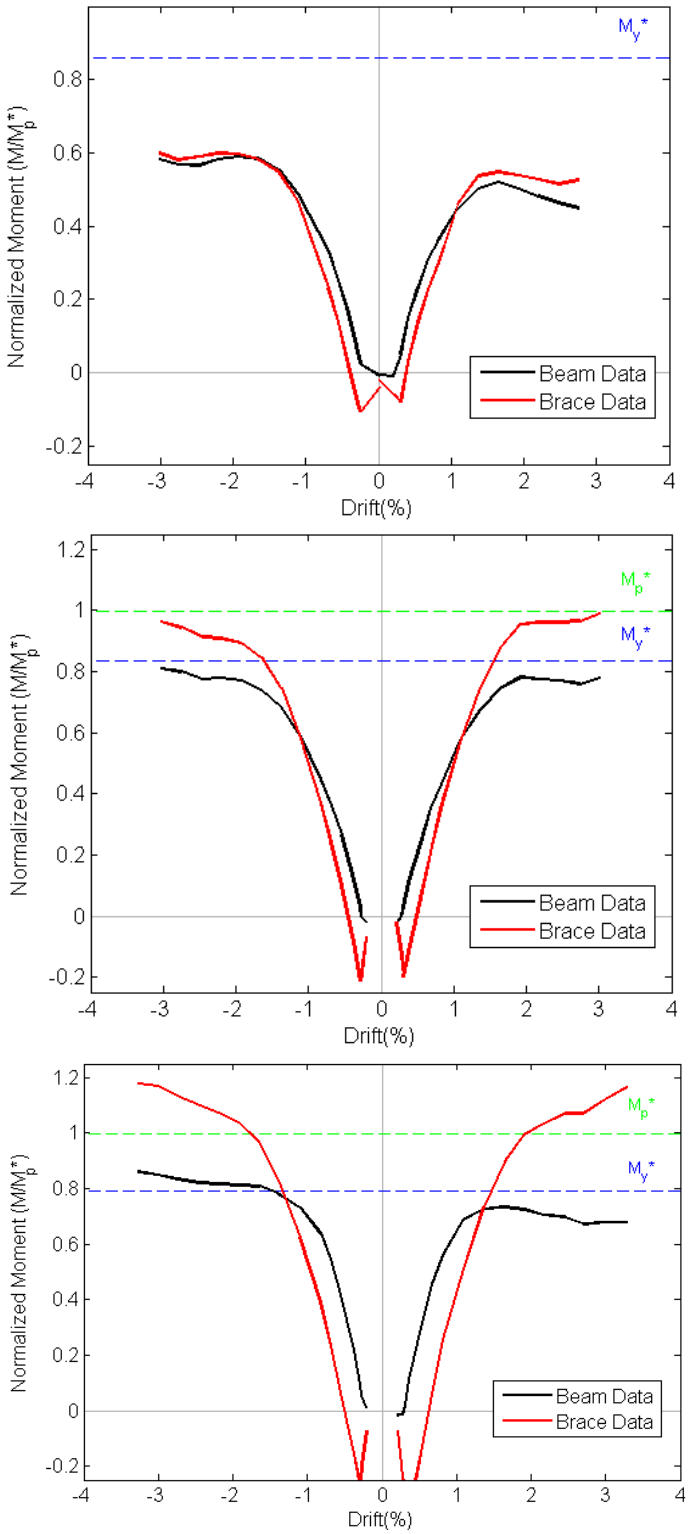

Figure 5.24: Comparison of beam flexural demand at edge of GP from brace and beam data.

Table 5.4 Beam shear, axial, and flexural demand summary.

Behavior	Design Value	Chevron 1	Chevron 2	Chevron 3
Max. total vertical force	165 kips	150 kips	104 kips	46 kips
Max. total horizontal force	211 kips	194 kips	168 kips	170 kips
Max moment in beam*	630 kip-ft	580 kip-ft	470 kip-ft	290 kip-ft

*calculated based on vertical component of brace axial forces

5.4.2 Beam Deflection

Beam deflection was measured using both a string potentiometer and Optotrak LED markers. As discussed in Section 5.1.3, the Optotrak and string potentiometer measurements matched well for Chevron 2 and 3 but were inconsistent for Chevron 1. For the plots in this section, only the string potentiometer deflection is used. The string potentiometer deflection measurement was corrected to exclude deflection due to column shortening, as shown in Figure 5.24. For Chevron 2 and 3 the column shortening was measured directly using string potentiometers attached to the top of each column. A correction was applied to the beam deflection in Chevron 1 by assuming the same magnitude of column shortening occurred as in Chevron 2 and 3 at a given drift level.

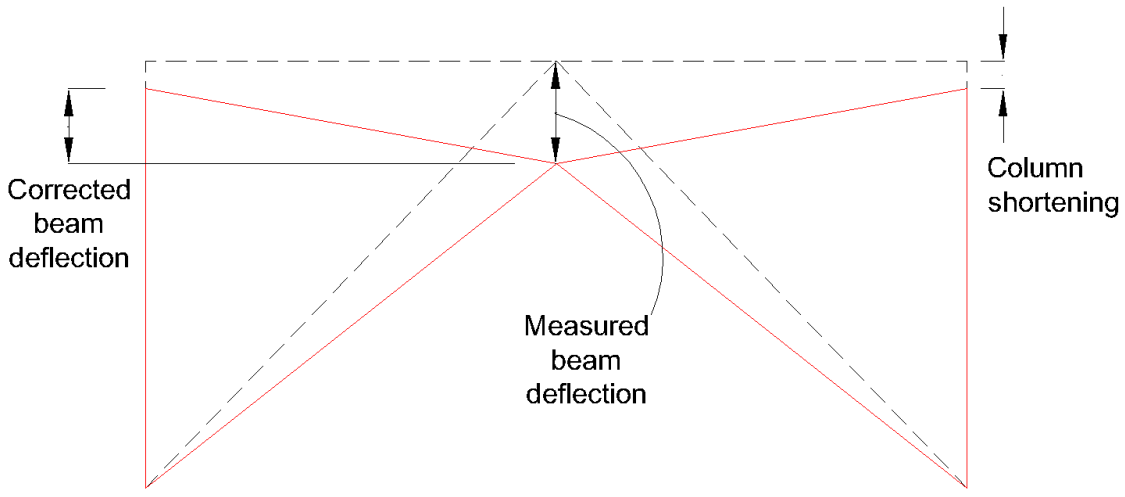

Figure 5.25: Beam deflection correction for column shortening.

Figure 5.26 shows a backbone curve of the beam mid-span deflection at the peaks of each cycle, plotted until the first brace fracture occurred. Figure 5.27 shows the beam deflection during points of zero frame lateral force, which correlates to the beam residual deflection if the earthquake were to stop at that point in the displacement history. Table 5.5 summarizes the maximum and residual beam deflections for each specimen.

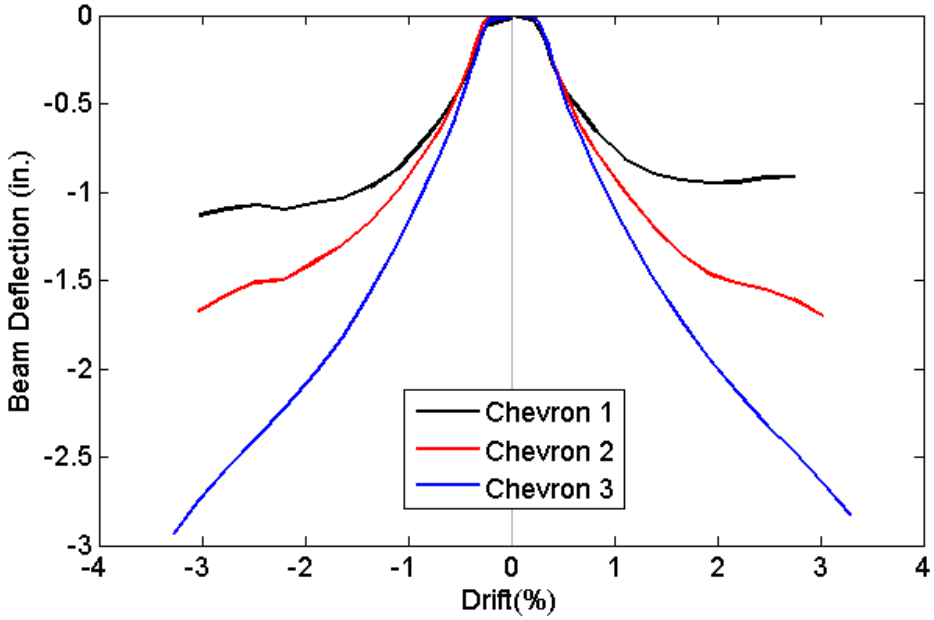

Figure 5.26: Peak beam deflection vs. interstory drift backbone curve.

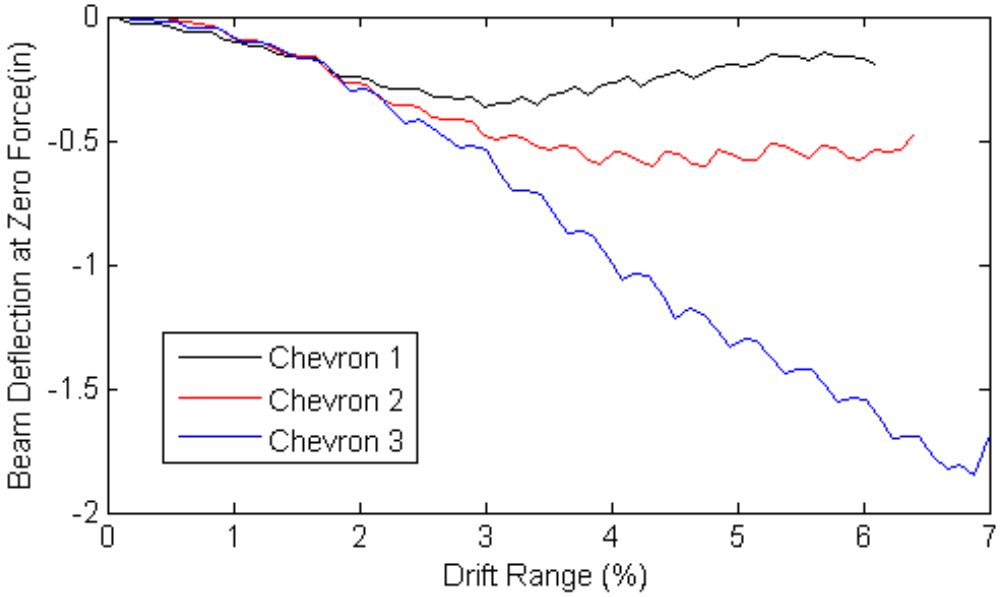

Figure 5.27: Beam deflection at zero lateral force.

Table 5.5 Beam deflection summary

Specimen	Beam DCR	Max. Beam Deflection	Max. Beam Residual Deflection
Chevron 1	0.83	-1.1 in.	-0.2 in.
Chevron 2	1.72	-1.8 in.	-0.5 in.
Chevron 3	2.67	-3.0 in.	-1.7 in.

As expected, the beams deflected more with decreasing beam strength. The beam deflection curve flattens out for Chevron 1, which is consistent with the observed plateau in the beam shear and flexural demand. In Chevron 2 and 3, the beam deflection continues to increase at higher drift cycles despite the observed plateau in shear and flexural demand. This is due to the accumulation of plastic deformation over the course of the test, as the yield moment was reached relatively early in the Chevron 2 and 3 tests. The accumulation of plastic deformation is also responsible for the significantly higher residual deflection observed in Chevron 3 at high drifts. The beam residual deflection is similar for the three specimens until a drift range of 2% (±1% story drift), after which the yielding beams begin to sustain larger residual deflections.

5.5 Column Performance

5.5.1 Column Shear, Flexural, and Axial Demand

Two sets of strain gauges were used to compute the shear, flexural, and axial demand on the each column, as shown in Figure 5.28. Each set contained 4 gauges – two on the outer flange and 2 on the inner flange. The moment and axial load from each set of gauges was determined in the same way as for the beam gauges, described in the previous section. Figures 5.29 and 5.30 show the column flexural demand at the edge of the corner gusset plate, where a plastic hinge formed in the columns. The flexural demand is normalized by the reduced plastic moment capacity, M_p^*. M_p^* is calculated with Equation 5.1a, using the average initial axial load in the columns to reduce the plastic moment capacity. Figure 5.31 shows the axial demand on each column versus interstory drift.

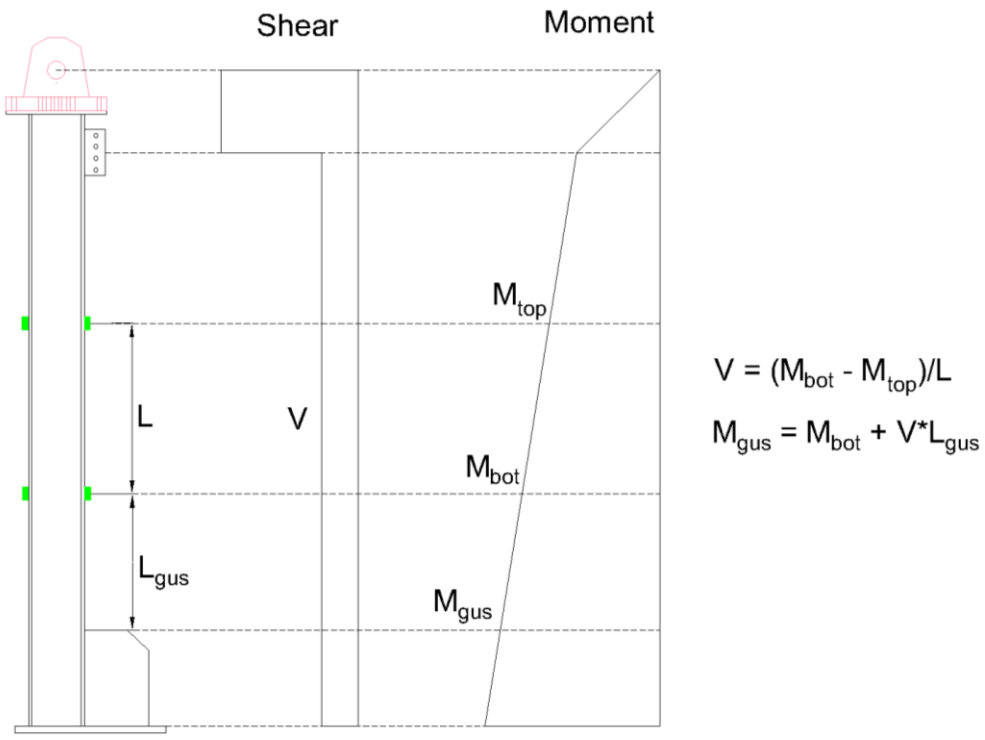

Figure 5.28: Column force determination.

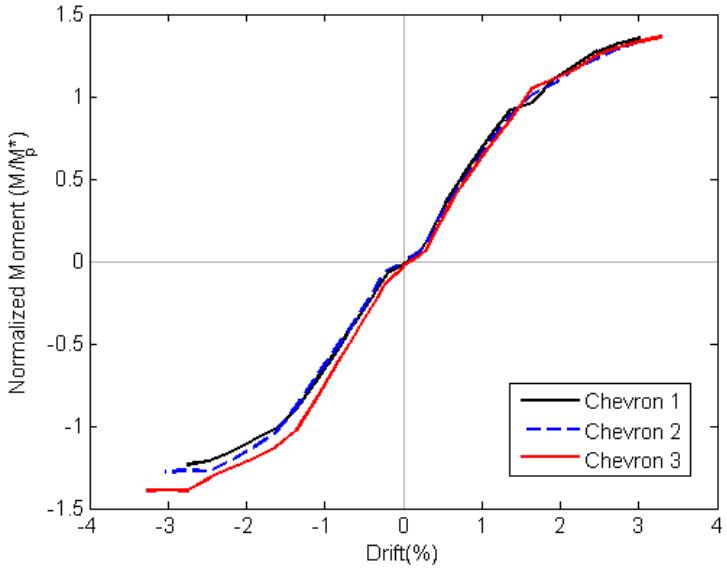

Figure 5.29: N column moment at top edge of corner gusset plate.

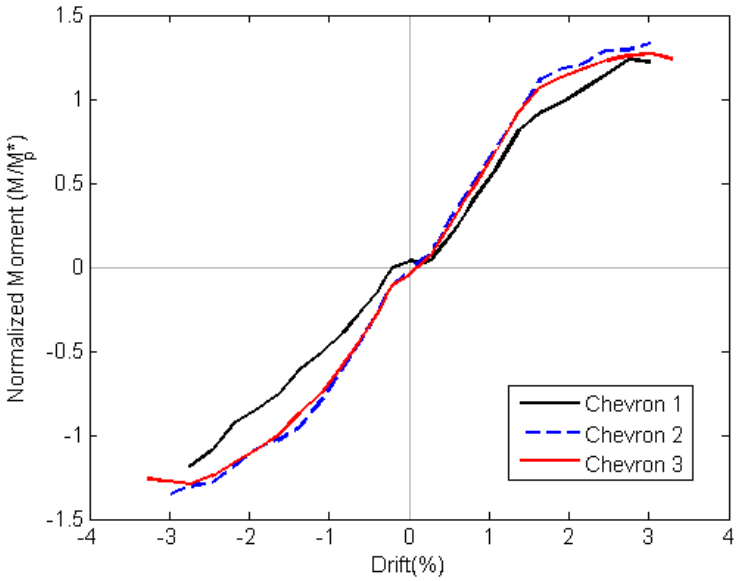

Figure 5.30: S column moment at top edge of corner gusset plate.

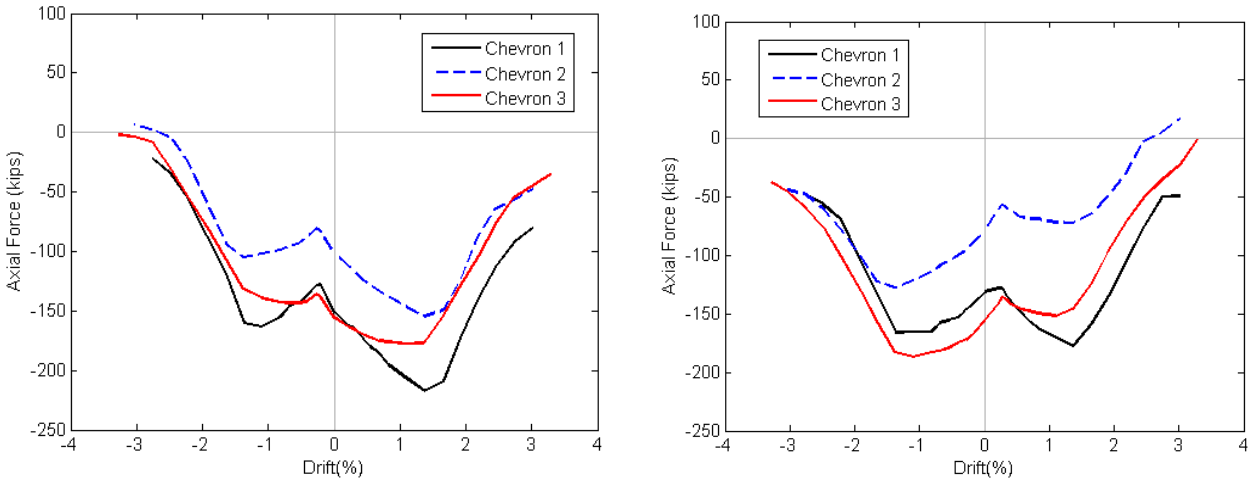

Figure 5.31: N (right) and S (left) column axial force.

The columns behaved similarly in all 3 tests as they experienced the same displacement history in each test. All of the columns exceeded their expected plastic moment capacity, M_p, from measured material properties. This was consistent with the observed local yielding and buckling in the plastic hinge region of the column. The column axial load began to decrease after around 1.75% drift in each test, which is when the columns started to shorten according to the string potentiometers used to measure axial deformation of the column. Note that the initial axial load in the columns in Chevron 2 was lower due to

an error when post-tensioning the columns. The columns contributed the same amount of lateral resistance in each test, however they contributed a greater proportion of the total lateral resistance in Chevron 2 and 3 because the total base shear was lower. Figure 5.32 shows the contribution to the total base shear contributed by the columns over the course of the test. At the beginning of the test, the columns do not provide a significant amount of lateral resistance to the frame. The column contribution becomes more significant at higher drifts, and comprises 20%, 30%, and 40% of the total base shear by the end of the test for Chevron 1, 2, and 3 respectively.

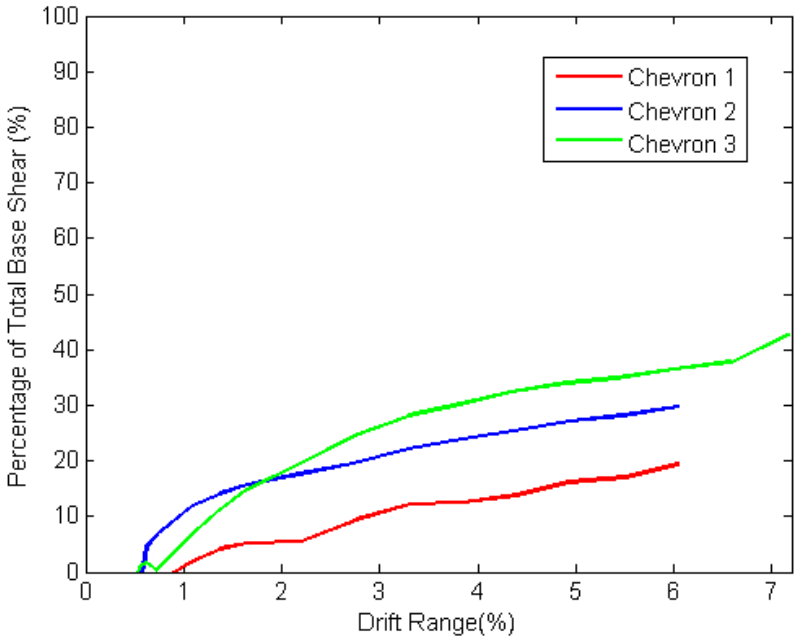

Figure 5.32: Column contribution to total lateral resistance.

5.6 Connection Performance

5.6.1 Gusset Plate Out-of-Plane Deformation

Out-of-plane deformation of the mid-span gusset plate was determined using Optotrak markers located on the edge of the mid-span gusset plate. Figure 5.33 shows the out of plane deformation of the mid-span gusset plate versus drift. The gusset plate out-of-plane deformation demand was not significantly impacted by the changing beam size. The gusset plate did not straighten out as much in the tension cycles in Chevron 3 which is consistent with the brace behavior as discussed in Section 5.3.2.

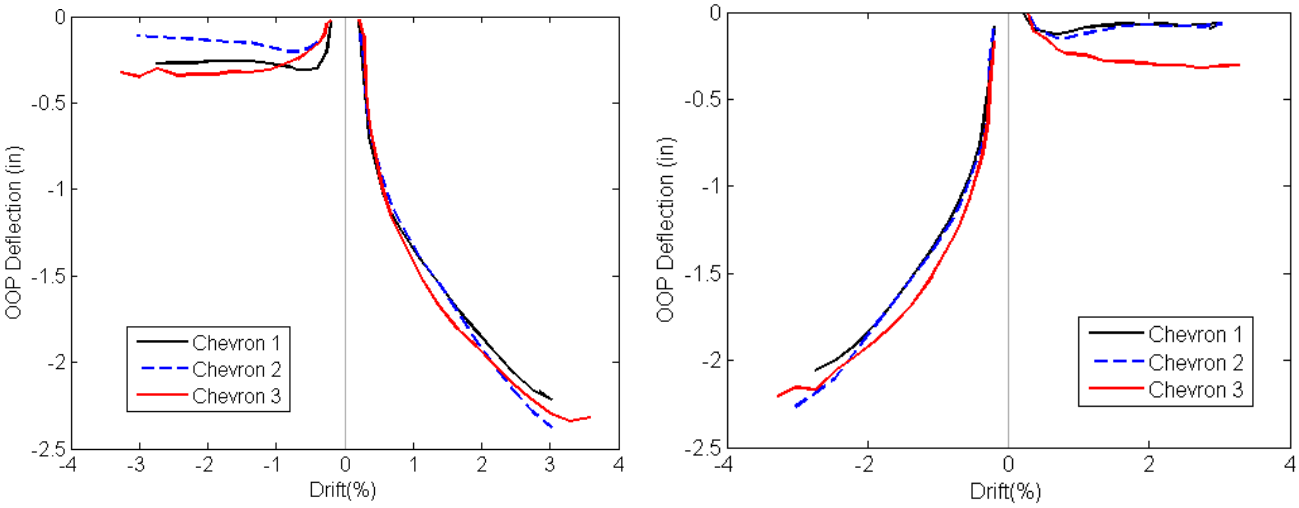

Figure 5.33: OOP deflection of N (right) and S (left) edges of mid-span gusset.

5.6.2. Weld Crack Propagation

The length of each weld crack was measured with a ruler at each peak displacement. The crack length was only measured on the top face of the weld; it should be notes that the crack length may have been different on the bottom face of the weld. Figure 5.34 shows the weld crack propagation as a function of drift range for each test. The weld cracking was less severe in Chevron 3 than in Chevron 1 and 2, however in all 3 test weld cracking did not lead to a significant drop in lateral resistance in the frame.

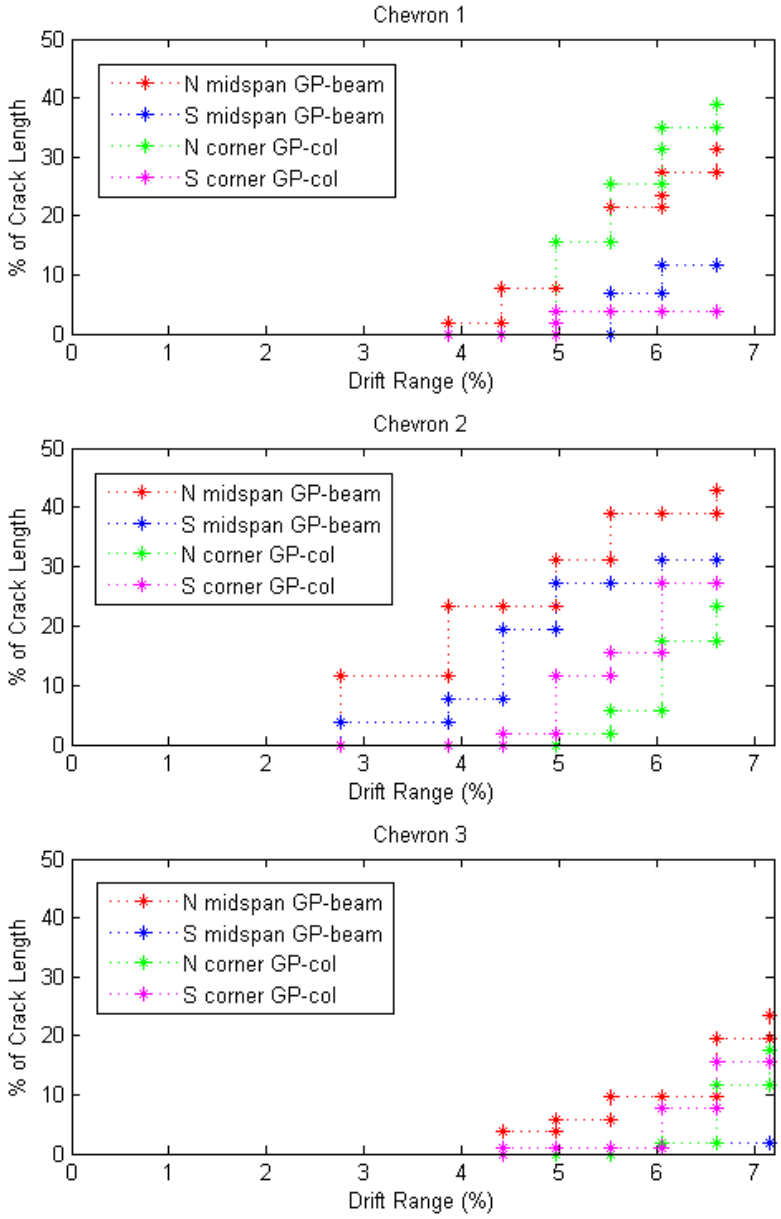

Figure 5.34: Weld crack propagation versus drift range.

5.7 Energy Dissipation Capacity

Energy dissipation capacity is another way of comparing frame performance as braced frames must be able to effectively dissipate energy through inelastic deformation during an earthquake. The following equation shows the general form of the energy dissipation equation:

$$W = \int F \, d\Delta$$

If you compute this integral over a full cycle of force-displacement behavior, only the dissipated energy is returned. A cumulative trapezoidal numerical integration was performed in Matlab, described by the following equation:

$$W = \sum_{i=1}^{n} \frac{F_i + F_{i-1}}{2} (\Delta_i - \Delta_{i-1})$$

where

W is the cumulative work done on the system or component

F is the force applied to the system or component

Δ is the displacement of the system or component

n is the number of data points

Energy dissipation was calculated for the system as a whole and also for the braces, beam, and columns individually. Table 5.6 shows the force and displacement measurements used to compute energy dissipation for each component. Note that energy dissipation contributed by the connections is not directly calculated, but is included in the total system energy dissipation. Figure 5.35 shows the energy dissipation from each component of the frames compared with the total system energy dissipation. The difference between the system energy dissipation and the sum of the contribution from the beam, columns, and braces is a combination of slight error in the measurements and energy dissipated by the connections.

Table 5.6 Measurements used in energy dissipation calculation

Component	F	Source of F	Δ	Source of Δ
System	Total base shear	Actuator load cell	Frame lateral displacement	Potentiometers
Braces	Brace axial force	Strain gauges	Brace axial elongation	Potentiometers
Beam	Beam shear	Strain gauges	Beam vertical deflection	Potentiometers
Column	Column moment at gusset plate	Strain gauges	Column rotation at gusset plate	Potentiometers

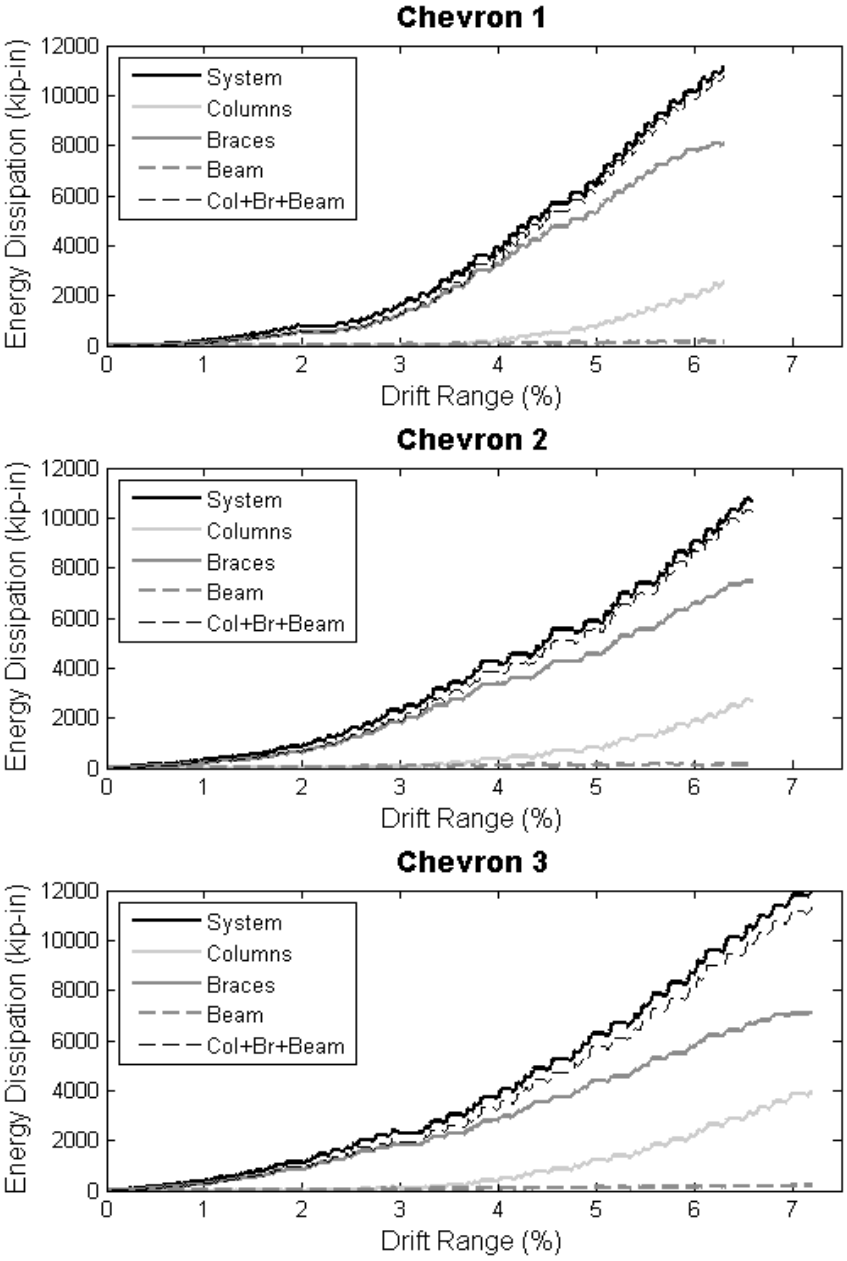

Figure 5.35: Cumulative energy dissipation.

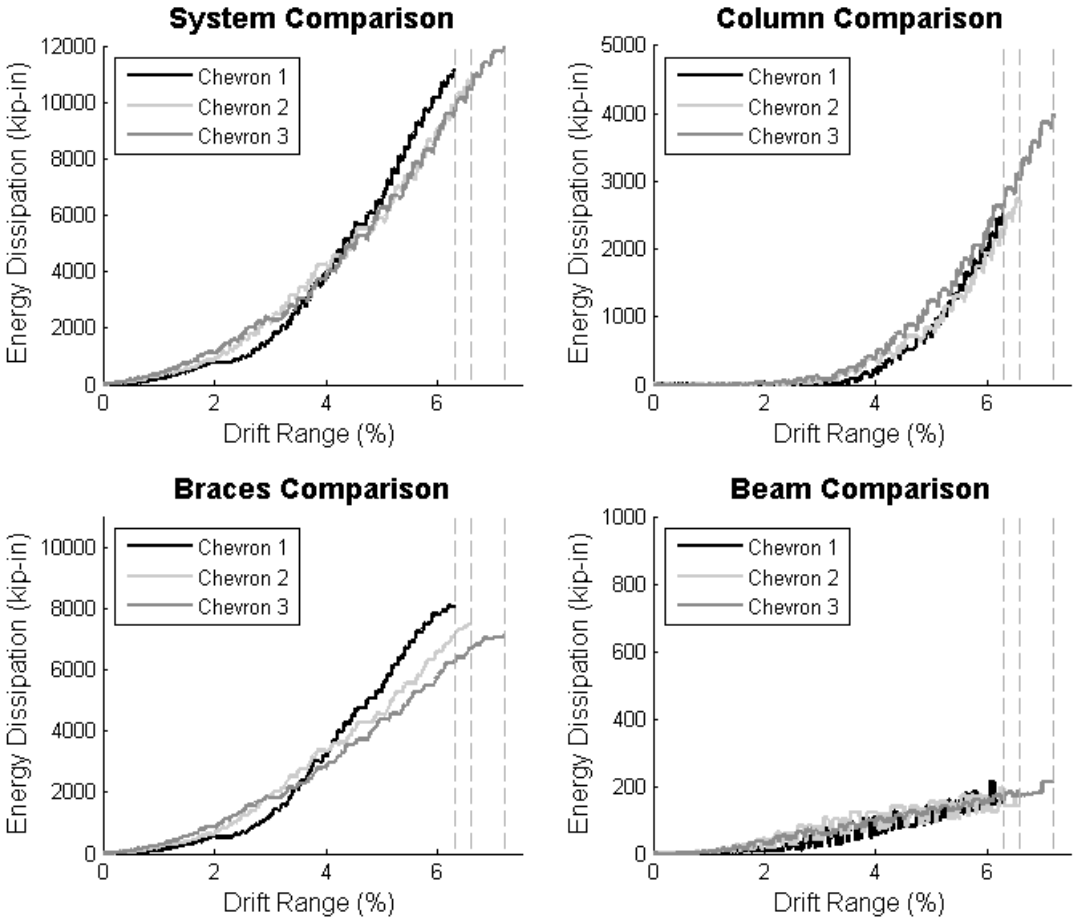

Figure 5.36: Comparison of energy dissipation by component.

Table 5.7 Cumulative energy dissipation summary

Specimen	Total energy dissipated by end of test (kip-in.)						
	System	Braces		Columns		Beam	
		Value	% of total	Value	% of total	Value	% of total
Chevron 1	11174	8073	73	2580	23	154	1.4
Chevron 2	10629	7458	70	2642	25	142	1.3
Chevron 3	11964	7137	60	3985	33	213	1.8

Figure 5.36 compares the energy dissipation of each component in each test, and Table 5.7 summarizes the cumulative energy dissipated by each component. Chevron 3 had the highest energy dissipation capacity due to the fact that it reached a higher drift than the other two specimens and consequently went through more displacement cycles. At 6.3% drift, the end of the Chevron 1 test, Chevron 1 had dissipated more energy than Chevron 2 and 3 due to the higher lateral forces reached during the test. The columns dissipated similar amounts of energy at a given drift range due to the identical displacement history experienced by the columns in each test. Because Chevron 3 reached a higher drift it had significantly more total energy dissipated by the columns. With weaker beams, the columns contributed a larger percentage of the total energy dissipation and the braces contributed a lower percentage. Chevron 1 dissipated the most energy through the braces due to the significantly higher tensile forces developed in the braces in that test. Chevron 2 and 3 were able to dissipate less energy through tension in the braces and more energy through compression in the braces as seen in the brace axial force-elongation plots in Section 5.3.2. The beam did not contribute significantly to the energy dissipation of the frame in any of the 3 tests.

Chapter 6

Conclusion

6.0 Introduction

Section 6.1 will provide a brief summary of the three tests conducted as part of this thesis. Section 6.2 discusses conclusions drawn based on the results of the tests. This is followed by recommendations for future work on chevron beam strength.

6.1 Summary

To investigate the effect of beam strength on the seismic performance of chevron SCBFs, three experimental specimens were designed and tested in the UW SRL. Each specimens consisted of a full-scale, single-bay, single-story chevron braced frame with square HSS braces. The three frames were identical except for the beam strength and stiffness in order to isolate its effect on frame performance. The frames were designed to be compliant with the 2010 AISC Seismic Provisions (AISC 2010a), except the beams in Chevron 2 and 3 which did not comply with the requirement to develop the unbalanced load that results from one brace at its tensile capacity and one brace at a 30% of its compressive capacity. The specimens were subjected to a quasi-static symmetric cyclic displacement history; the key response characteristics of each frame are summarized in Table 6.1. In each test the failure mode was fracture of both braces. In Chevron 2 and 3 there was yielding observed in the top and bottom flanges at the center of the beam. In all three tests, the columns underwent yielding and local buckling in the plastic hinge region at high drifts. There was yielding observed in the shear tab and gusset plate connections and weld

cracking in the gusset plate to framing member welds, but this did not affect the overall lateral resistance of the frame. After both braces fractured, the frames were subjected to additional displacement cycles to measure the residual lateral resistance from frame action.

Table 6.1 Specimen Response Summary

Behavior	Chevron 1	Chevron 2	Chevron 3
Beam Interaction DCR	0.83	1.71	2.67
Max. Lateral Resistance	234 kips	206 kips	177 kips
Max. Lateral Resistance/$2P_{cr}\cos\theta$	1.34	1.18	1.01
Max. Drift Range	6.3%	6.6%	7.2%
Max. beam deflection	1.1 in.	1.8 in.	3.0 in.
Max. brace OOP deflection	17.3 in.	17.8 in.	19.6 in.

6.2 Conclusions

Chevron CBFs with yielding beams employ a different plastic mechanism than those with beams designed to develop the brace unbalanced load. In code compliant frames, inelastic deformation is limited to brace yielding and buckling, while in frames with beam DCRs greater than 1 plastic deformation of the beam also occurs. The test results show that chevron SCBFs with beam DCRs of up to 2.67 exhibit similar performance histories in terms of component yielding and damage. Based on the performance of the three specimens, the following conclusions can be drawn about the effect of beam strength on chevron SCBF performance:

Lateral resistance: The frames with yielding beams had decreased lateral resistance due to a decrease in tensile force developed in the braces. However the lateral resistance did not drop below the frames' expected strength of twice the lateral component of the brace critical buckling load.

Deformation capacity: All three of the specimens achieved high ductility, with the Chevron 2 and 3 reaching progressively larger drift levels than Chevron 1. Each specimen reached a drift range greater than 6%, which is higher than that typically achieved by SCBFs. SCBFs with connections designed according the BDP have been shown to reach a mean drift range of 4.5%

(Roeder et al. 2012). A1085 HSS braces were utilized instead of the more commonly specified A500 braces, and the different brace material may be partially responsible for the high deformation capacity of the test specimens. The ASTM A1085 material specification has tighter tolerances for the corner radius and wall thickness of the tube, which may serve to increase the fracture life of the A1085 braces over ASTM A500 braces.

Beam Performance: Decreasing beam strength led to increased plastic deformation of the beam. The beam in Chevron 1 did not yield and underwent only elastic deflections. The beam in Chevron 2 reached its yield moment at 1.5% drift and reached its plastic capacity by the end of the test (3.3% drift). The beam in Chevron 3 reached its flexural yield capacity at 1.25% drift and reached its plastic capacity by 2% drift. The beam deflections were similar at drifts of less than 1%, but at higher drifts the deflections in the yielding beam frames became more significant. Chevron 3 had a residual beam deflection of 1 inch at a story drift of 2% and 1.7 inches by the end of the test (3.6% drift).

Brace Performance: Beam strength affected the brace behavior and fracture life. The yielding beams deflected more, leading to less tensile elongation and more compressive shortening of the braces. As a result the braces developed lower tensile forces in the frames with yielding beams, which resulted in a corresponding reduction in lateral resistance of the frames. The lower tensile forces were also responsible for extending the fracture life of the braces, because the beam was unable to develop enough tension in the braces to fully yield the brace in tension and this delayed fracture until larger frame drifts.

Connection Performance: The connection performance was not significantly affected by the changes in beam strength. The gusset plates underwent similar levels of yielding and weld cracking. The shear tabs reached the moderate yielding performance state in Chevron 3 due to greater end rotation of the beam.

Column Performance: The columns provided similar amounts of lateral resistance in each test and exhibited yielding and local bucking at the same drift levels. The third specimen reached a

higher drift range than the first two specimens, which resulted in more yielding and local buckling in the columns by the end of the third test.

Energy Dissipation Capacity: The system energy dissipation capacity was similar in each of the three specimens. At a given drift level, the yielding beam specimens exhibited slightly lower energy dissipation due to the lower lateral resistance; however by the end of the test the yielding beam specimens had dissipated more energy than the full strength specimen because they underwent additional cycles before failure. The beam was not a significant source of energy dissipation in any of the tests; the majority of the energy dissipation was provided by the braces, and the column contribution became significant at higher drifts.

6.3 Recommendations for Future Research

The following recommendations for future research are proposed based on limitations in the research presented in this report and new questions raised by the present research.

Experimental studies:

- Investigation of the performance of chevron SCBFs with beams of lower strength and stiffness than the ones tested. These results suggest that chevron SCBFs still perform well with beam DCRs up to 2.67, however there may be a limit at which the beam is too weak to achieve adequate strength and ductility of the frame. The third specimen reached a lateral resistance equal to the design strength, and it is likely that use of a smaller beam would result in lateral resistance lower than the design strength.
- Exploration of the effect of chevron beam strength with different beam end conditions. In a multi-story frame, the beams on the lower floors would have gusset plates welded to the top flange at the beam-column connections. The effect of this additional restraint of beam end rotation should be studied. Some chevron frames utilize fully restrained beam-column connections and the effect of beam strength on these dual-system frames is also important to determine.
- Investigation of chevron beam strength considering the contribution of composite action. The inclusion of additional beam strength and stiffness due to composite action when

designing chevron SCBFs varies from firm to firm. The 1981 U.S.-Japan tests showed a loss of composite action due to excessive beam deflection, and while there was no indication of this in subsequent tests of chevron CBFs with composite slabs it is worthy of further study.

- Investigation of the effect of beam strength on the system performance of multi-story chevron SCBFs. Multiple tests have shown a tendency for chevron CBFs to concentrate damage in one or two stories. The effect of beam strength on this soft story behavior should be studied.
- Study of chevron SCBFs using A500 braces instead of A1085 braces. A500 HSS sections are commonly specified, so it is worth studying whether the high ductility achieved by the frames was a result of the A1085 brace material.

Numerical studies:

- Development of an accurate finite element model of yielding-beam chevron frames in order to perform parametric studies on the effect of:
    - Variations in beam strength
    - Multi-story frame with yielding beams
    - Variations in column strength
    - Effect of brace compactness and slenderness ratios
    - Dynamic time-history analyses

Design

- Development of a model to predict chevron SCBF frame resistance based on relative strength and stiffness of the beam and braces. While FE models can be developed to determine this, it is useful for practicing engineers to be able to accurately estimate frame strength without a computational model.
- Development of a design methodology for chevron SCBFs with a beam yielding mechanism
    - Application of this methodology to seismic evaluation and retrofit. Many older CBFs have non-compliant beams, so extension of yielding-beam chevron SCBF design theory would be useful.

References

AISC (1997). “Seismic provisions for structural steel buildings." AISC 341-97, American Institute of Steel Construction, Chicago, IL.

AISC (2010a). “Seismic provisions for structural steel buildings." AISC 341-10, American Institute of Steel Construction, Chicago, IL.

AISC (2010b). “Specification for structural steel buildings." AISC 360-10, American Institute of Steel Construction, Chicago, IL.

AISC (2010c). “Steel construction manual." American Institute of Steel Construction, Chicago, IL.
Roeder, C.W., (1989) Seismic behavior of a concentrically braced frame, Journal of Structural Division, ASCE, Vol. 115, No. 8, New York, pgs 1837-56.

ASTM A370-17. “Standard Test Methods and Definitions for Mechanical Testing of Steel Products.” ASTM International, West Conshohocken, PA, 2017.

Foutch, D. A., Goel, S. C., and Roeder, C. W. (1987). Seismic testing of full-scale steel building - part I." *Journal of Structural Engineering*, 113(11), 2111-2129.

Fukuta, T., Nishiyama, I., Yamanouchi, H., and Kato, B. (1989). “Seismic performance of steel frames with inverted v braces." *Journal of Structural Engineering*, 115(8), 2016-2028.

Khatib, I. F., Mahin, S. A., and Pister, K. S. (1988). “Seismic behavior of concentrically braced steel frames." *PEER Report 1988/01*, Pacific Earthquake Engineering Research Center, Berkeley,CA.

Lehman, D. E., Roeder, C. W., Herman, D., Johnson, S., and Kotulka, B. (2008). “Improved seismic performance of gusset plate connections." *Journal of Structural Engineering*, 134(6), 890-901.

Lumpkin, E. J. (2009). “Enhanced seismic performance of multi-story special concentrically braced frames using a balanced design procedure." M.S. thesis, University of Washington, Seattle.

Lumpkin, E. J., Hsiao, P. C., Roeder, C. W., Lehman, D. E., Tsai, C. Y., Wu, A. C., Wei, C. Y., and Tsai, K. C. (2012). Investigation of the seismic performance of three-story special concentrically braced frames." *Journal of Constructional Steel Research*, 77, 131-144.

Okazaki et al. (2013) "Dynamic Response of a Chevron Concentrically Braced Frame." *Journal of Structural Engineering* 139.4. 515-25.

Roeder, C. W., Lumpkin, E. J., and Lehman, D. E. (2011b). “A balanced design procedure for special concentrically braced frame connections." *Journal of Constructional Steel Research*, 67(11), 1760{1772.

Roeder, C. W., Lumpkin, E. J., Lehman, D. E. (2012). “Seismic Performance Assessment of Concentrically Braced Steel Frames.” *Earthquake Spectra*, 28(2), 709-727.

Uriz, P. and Mahin, S. A. (2008). “Toward earthquake-resistance design of concentrically braced steel-frame structures." *PEER Report 2008/08*, Pacific Earthquake Engineering Research Center,Berkeley, CA.

Appendix 1

Test Setup Drawings

A1.1 Reaction blocks

For both blocks all bars were #5.

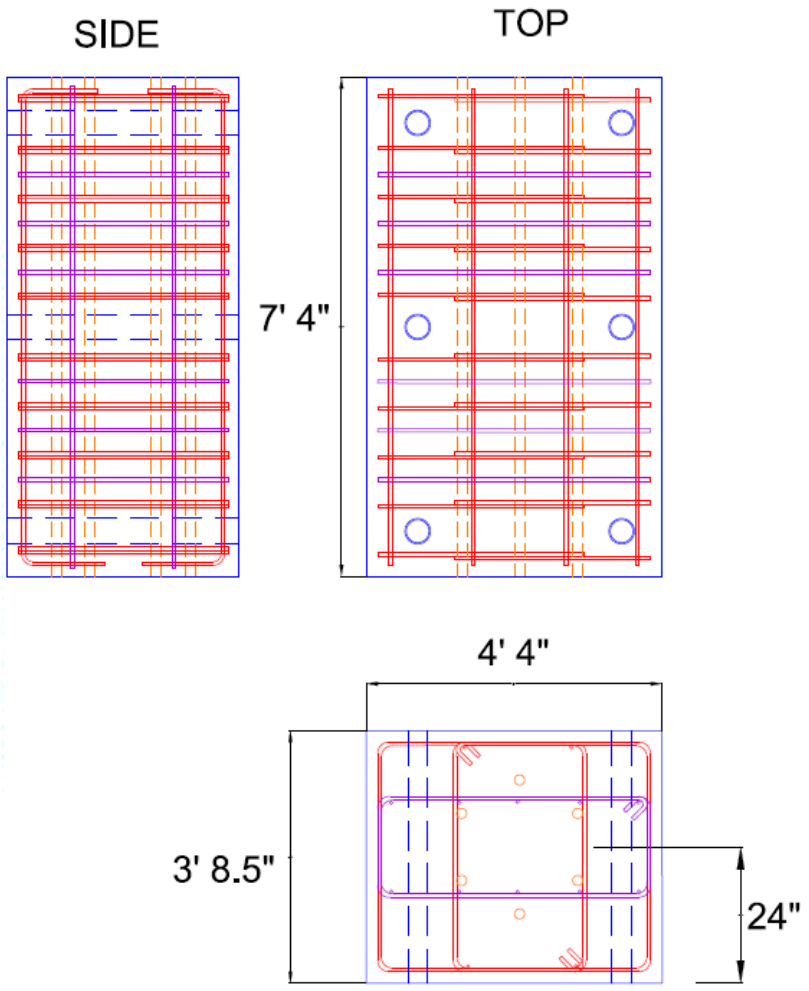

Figure A1.1: Dimensions and rebar layout for actuator anchorage block.

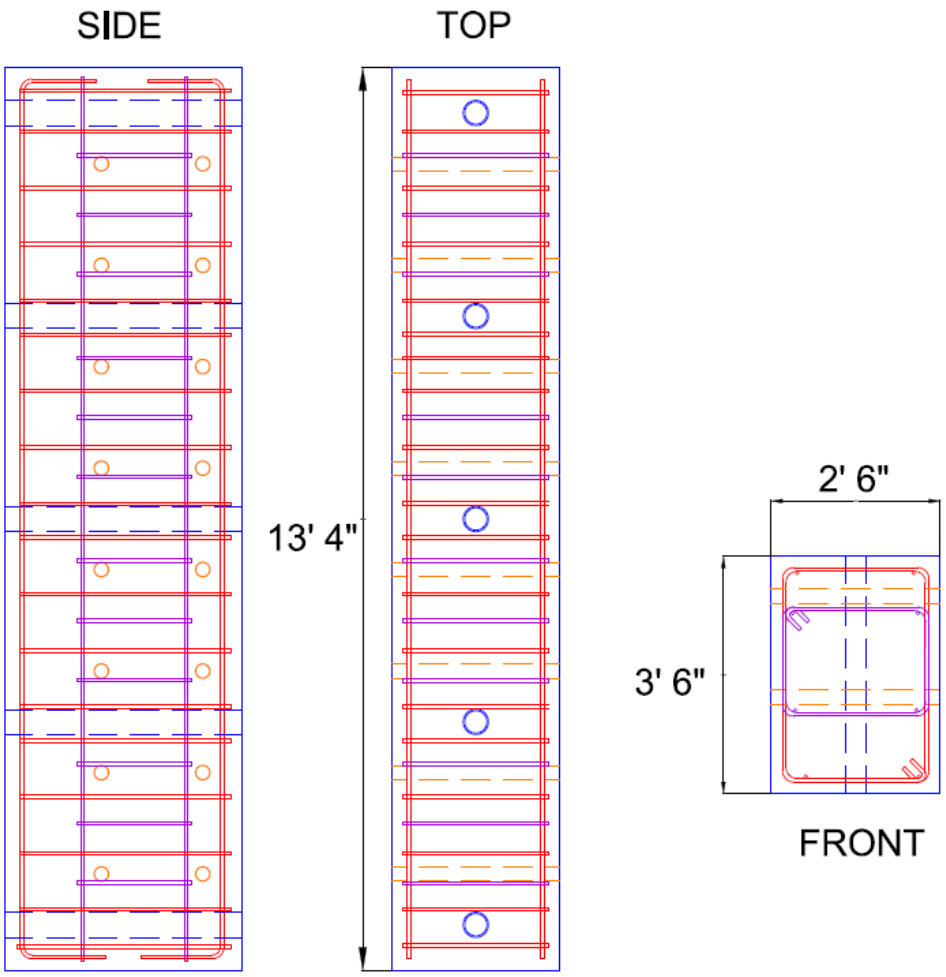

Figure A1.2: Dimensions and rebar layout for column anchorage block.

A1.2 Load Spreader Beam

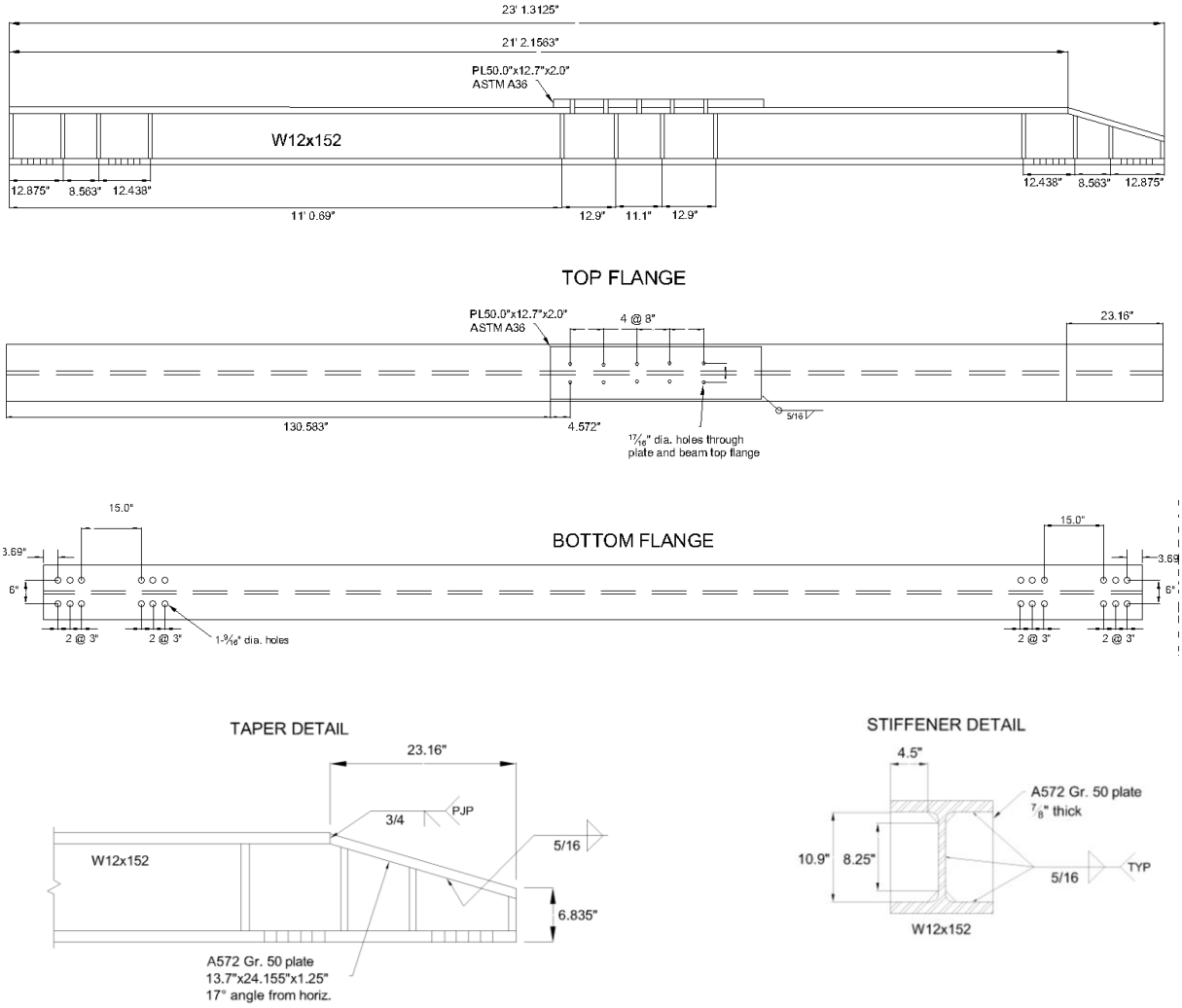

Figure A1.3: Load spreader beam details.

Appendix 2

Sample Calculations

A2.1 Brace Selection

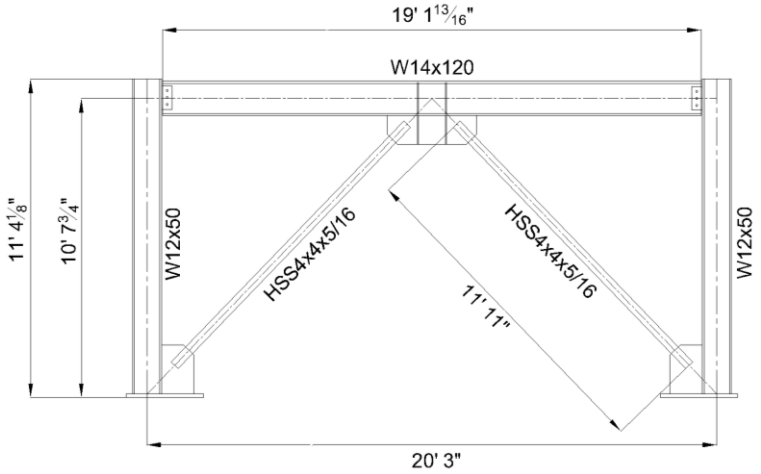

Figure A2.1: Specimen geometry and member sizes.

Actuator capacity = 500 kips compression, 450 kips tension

Use A1085 Gr. 50 brace. Try HSS4x4x5/16:

Brace tensile capacity

$P_t = R_y F_y A_g = 1.25(50\text{ ksi})(4.1\text{ in.}^2) =$ **256 kips**

Brace compressive capacity

$$F_e = \frac{\pi^2 E}{\left(\frac{KL}{r}\right)^2} = \frac{\pi^2(29000\text{ ksi})}{\left(\frac{143\text{ in.}}{1.49\text{ in.}}\right)^2} = 31.1\text{ ksi}$$

$$\frac{R_y F_y}{F_e} = 2.0 < 2.25$$

$$F_{cr} = \left(0.658^{R_y F_y / F_e}\right) R_y F_y = \left(0.658^{1.25(50\text{ ksi})/(31.1\text{ ksi})}\right)(1.25)(50\text{ ksi}) = 27.0\text{ ksi}$$

$P_c = 1.14 F_{cr} A_g = 1.14(27.0\text{ ksi})(4.1\text{ in.}^2) =$ **126 kips**

Expected lateral resistance
Braces alone:
$F_{brace} = (P_t+P_c)\cos\theta = (256+126)\cos(46.1°) = 265$ kips
Assume columns contribute 30% of the maximum lateral resistance:
$F_{total} = 1.3F_{brace} =$ **344 kips**

Demand-to-capacity ratio for actuator
$DCR = \frac{344}{450} = \mathbf{0.76}$ → Safe

A2.2 Beam Design

Demand
Both braces at maximum capacity:
Vertical - $V = (P_c - P_t)\sin\theta = (126 - 256)\sin 46.1° = -93.7$ kips
Horizontal - $H = (P_c + P_t)\cos\theta = 265$ kips

Post-buckling unbalanced load:
Vertical - $V = (0.3P_c - P_t)\sin\theta = (0.3(126) - 256)\sin 46.1° = -157.2$ kips
Horizontal - $H = (0.3P_c + P_t)\cos\theta = (0.3(126)+ 256)\cos(46.1°) = 203.7$ kips

Maximum Moment
Assume beam remains rigid over gusset plate region and plastic hinges form at the edge of the gusset plate:

Both braces at maximum capacity:
$VL_a\alpha = 2\alpha M_P$
$M_p = \frac{VL_a}{2} = \frac{93.7 \text{ kips}(96 \text{ in.})}{2} =$ **375 k-ft**

Post-buckling unbalanced load:
$VL_a\alpha = 2\alpha M_P$
$M_p = \frac{VL_a}{2} = \frac{157.2 \text{ kips}(96 \text{ in.})}{2} =$ **629 k-ft**

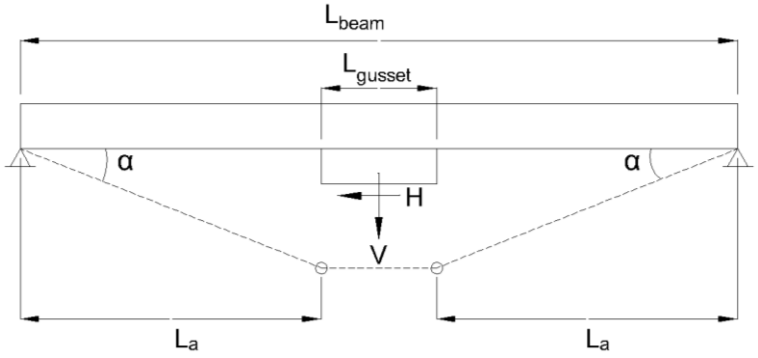

Figure A2.2: Assumed collapse mechanism.

Demand-to-Capacity Ratio
W14x120 (braced against flexural and lateral-torsional buckling):
$\phi M_p = 795.0$ kip-ft
$\phi P_n = 1546$ kips
$\phi V_n = 257$ kips
$1.1R_yM_p = 1068.84$ kip-ft

Both braces at maximum capacity:
Flexural DCR = $\frac{375}{795} = 0.47$

Axial DCR = $\frac{265}{1546}$=0.08 < 0.2
Combined DCR = $\frac{0.08}{2}$+0.47 = **0.51**

Post-buckling unbalanced load:
Flexural DCR = $\frac{629}{795}$= 0.79
Axial DCR = $\frac{203.7/2}{1546}$= 0.07 < 0.2
Combined DCR = $\frac{0.07}{2}$+ 0.79 = **0.83**

A2.3 Shear Plate Design

Demand
Both braces at maximum capacity:
V = (93.7 kips)/2 = 46.9 kips
P = (265 kips)/2 = 132.5 kips
Resultant = 140.6 kips @ 19.5°

Post-buckling unbalanced load:
V = (157.2 kips)/2 = 78.6 kips
P = (203.7 kips)/2 = 101.9 kips
Resultant = 128.7 kips @ 37.6°

Plate Design
W14x120
T = 10" → Use 10"x4.5" plate
t_w = 0.59"
Use A572 Gr. 50 Plate.

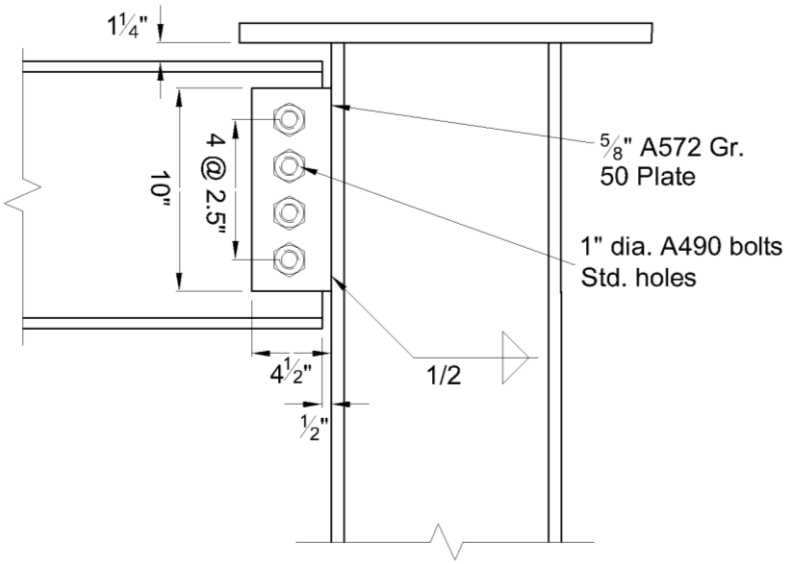

Figure A2.3: Shear plate detail.

Use 4 1"-dia. A490-X Bolts:
ϕr_n = 49.5 kips
ϕR_n = 4(49.5 kips) = 198 kips > 140.6 kips

Determine required plate thickness
Bolt bearing:
l_c= 2 in./cos(19.5°)=2.12 in.
$\phi 1.5 l_c t F_u$ > 140.6 kips/4 bolts
0.75(1.5)(2.15 in.)t(65 ksi) > 35.2 kips
t > 0.223 in.

Bolt tear-out:
l_c = 2.12 in.

$\phi 3.0dtF_u > 35.2$ kips
$0.75(3.0)(1.0 \text{ in.})t(65 \text{ ksi}) > 35.2$ kips
$t > 0.241$ in.

Plate tensile rupture:
$\phi F_u A_e > 132.5$ kips
$0.75(65 \text{ ksi})(10\text{-}4(1.0625"))t > 132.5$ kips
$t > 0.473$ in.

Plate shear rupture:
$\phi F_u A_e > 78.6$ kips
$0.75(0.6)(65 \text{ ksi})(10\text{-}4(1.0625"))t > 78.6$ kips
$t > 0.467$ in.

Block shear rupture (due to tension component – U shaped tear out):
$U_{bs}F_u A_{nt}=1.0(65 \text{ ksi})(7.5"\text{-}3(1.0625"))t=280.3t$
$0.6F_u A_{nv}=0.6(65 \text{ ksi})(2)(2"\text{-}0.5(1.0625"))t=114.6t$
$0.6F_y A_{gv}=0.6(50 \text{ ksi})(2)(2")t=120t$
$\phi R_n = 0.75(114.6t+280.3t) > 132.5$ kips
$t > 0.45$ in.

Block shear rupture (due to shear component – L shaped tear out):
$U_{bs}F_u A_{nt}=1.0(65 \text{ ksi})(2"\text{-}0.5(1.0625"))t=95.5t$
$0.6F_u A_{nv}=0.6(65 \text{ ksi})(8.75"\text{-}3.5(1.0625"))t=196.2t$
$0.6F_y A_{gv}=0.6(50 \text{ ksi})(8.75")t=262.5t$
$\phi R_n = 0.75(95.5t+196.2t) > 78.6$ kips
$t > 0.36$ in.

Shear and Tension Interaction
Combined shear and tension:

$$\left(\frac{P_u}{\phi P_n}\right)^2 + \left(\frac{V_u}{\phi V_n}\right)^2 < 1$$

Try 5/8” plate (plate rupture controls):

Bolt Bearing: $\varphi R_n = 98.3$ kips/bolt
Bolt Tear-Out: $\varphi R_n = 91.4$ kips/bolt
Plate Tensile Rupture: $\varphi R_n = 175.2$ kips
Plate Shear Rupture: $\varphi R_n = 105.1$ kips
Block Shear Rupture (Tension): $\varphi R_n = 185.1$ kips
Block Shear Rupture (Shear): $\varphi R_n = 136.7$ kips

Both braces at capacity:

$$\left(\frac{132.5 \text{ kips}}{175.2 \text{ kips}}\right)^2 + \left(\frac{46.9 \text{ kips}}{105.1 \text{ kips}}\right)^2 = 0.75628^2 + 0.44624^2 = 0.77 < 1$$

Unbalanced load:

$\left(\frac{101.9 \text{ kips}}{175.2 \text{ kips}}\right)^2 + \left(\frac{78.6 \text{ kips}}{105.1 \text{ kips}}\right)^2$ = 0.58162^2 + 0.74786^2 = 0.90 < 1

Size welds:
From AISC *Manual* Table 8-4: Angle = 19.5°, l = 10", e = 2.5", a = e/l=0.25, k=0 →C=4.54 (interpolated)
Angle = 37.6°, l = 10", e = 2.5", a = e/l=0.25, k=0 →C=3.91 (interpolated)

ϕR_n = 0.75(4.42(1.0)D(10") > 140.6 kips
D = 4.24 sixteenths → Use 5/16" fillet welds

ϕR_n = 0.75(3.91(1.0)D(10") > 128.7 kips
D = 4.39 sixteenths → Use 5/16" fillet welds

A2.4 Gusset Plate Design

Corner Gusset Plate Design

Demand
HSS4x4x5/16: P_t = 256 kips
P_c = 126 kips

Capacity
Brace-to-gusset welds
4 fillet welds, 3/8" thick

$$L = \frac{P_{ut}}{\beta(0.6)F_{exx}N_w(0.707)w}$$
$$= \frac{256\ kips}{(0.75)(0.6)(70\ ksi)(4)(0.707)(0.375")}$$
= 7.66"
→ Use 9" fillet welds

Brace-to-gusset base metal
$\beta R_n = 0.75(0.6)F_u N_s L_{ct} t_f$
= 0.75(0.6)(62 ksi)(4)(9")(0.375")
= 377 kips > 256 kips o.k.

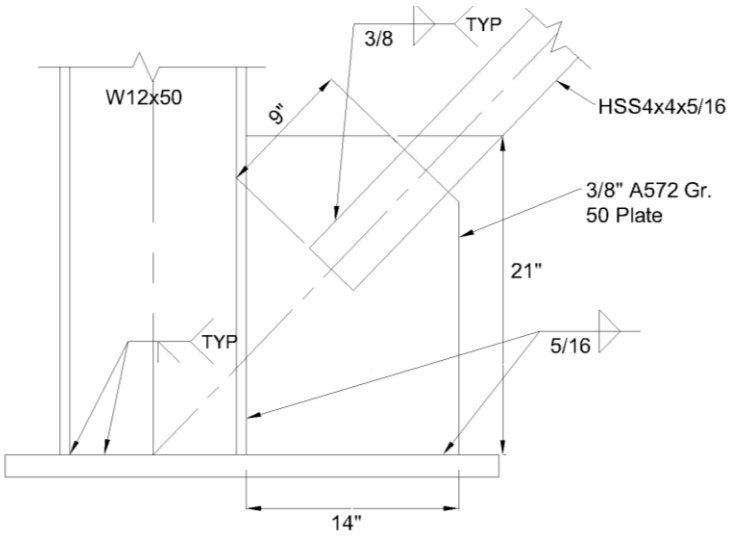

Figure A2.4: Corner gusset plate detail.

Gusset plate thickness
Whitmore width: B_w = 4" + 2(9"(tan37.5°)) = 17.8"

Yielding: $t_p > \frac{P_{ut}}{\phi F_y B_w} = \frac{256\ kips}{0.9(1.1)(50\ ksi)(17.8")} = 0.32"$

Rupture: $t_p > \frac{P_{ut}}{\phi F_u B_w} = \frac{256\ kips}{0.75(65\ ksi)(17.8")} = 0.30"$

Block Shear: $t_p > \frac{P_{ut}}{\phi(0.6F_u A_{gv} + U_{bs} F_u B)} = \frac{256\ kips}{0.75[0.6(65\ ksi)(2)(9)+1.0(65\ ksi)(4.0)]} = 0.351"$

Plate buckling capacity
Brace buckling capacity: P_c = 126 kips

$$L_{avg} = \frac{8.25" + 8.3125" - 1.0625"}{3} = 5.17"$$

$$\frac{KL_{avg}}{r} = \frac{0.65(5.17")}{0.375"/\sqrt{12}} = 31.0$$

$$F_e = \frac{\pi^2 E}{\left(\frac{KL}{r}\right)^2} = \frac{\pi^2(29000\ ksi)}{31.0^2} = 297.8\ ksi$$

$F_{cr} = \left(0.658^{F_y/F_e}\right)F_y = \left(0.658^{(50\ ksi)/(298\ ksi)}\right)(50\ ksi) = 46.6\ ksi$

$P_{uc} = \beta B_w t_p F_{cr} = 0.9(17.8)(0.375")(46.6\ ksi) = 280\ kips > 127.4\ kips$ o.k.

Interface welds
$w > \frac{R_y F_y t_p}{2(1.5)\beta(0.6)F_{exx}(0.707)} = \frac{(1.1)(50\ ksi)(0.375")}{2(1.5)(0.75)(0.6)(70\ ksi)(0.707)} = 0.309"$
→ Use 5/16" fillet welds

Net section fracture
A_{nt} = 4.1" – 2(0.375" + 0.125") = 3.7875"

$$\bar{x} = \frac{B^2 + 2BH}{4(B+H)} = 1.5$$

$$U = 1 - \frac{\bar{x}}{l} = 1 - \frac{1.5}{9} = 0.833$$

$\beta R_n = \beta U(R_{tb} F_u b A_{nb} + F_{up} A_{gp})$
= 0.95(0.833)(1.3)(62 ksi)(3.7875")
= 241.6 kips <281 kips
→ Net section reinforcement needed

Workable flat = 2.575 in.
Try 2"x0.25" Gr. 50 plates:
$\beta R_n = \beta U(R_{tb} F_u b A_{nb} + F_{up} A_{gp})$
= 0.95(0.833)[1.3(62 ksi)(3.7875")+1.1(65 ksi)(2)(2")(0.25")]
= 298 kips < 281 kips **o.k.**
Use ¼" fillet welds.

Middle Gusset Plate

Everything the same as corner gusset except plate buckling:

$$L_{avg} = \frac{5.125" - 2.9375" - 3.5"}{3} = -0.4375"$$

Gusset plate buckling will not control.

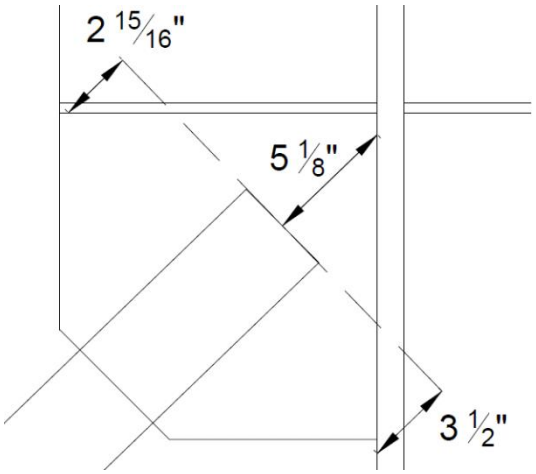

A2.5 Column Web Doubler

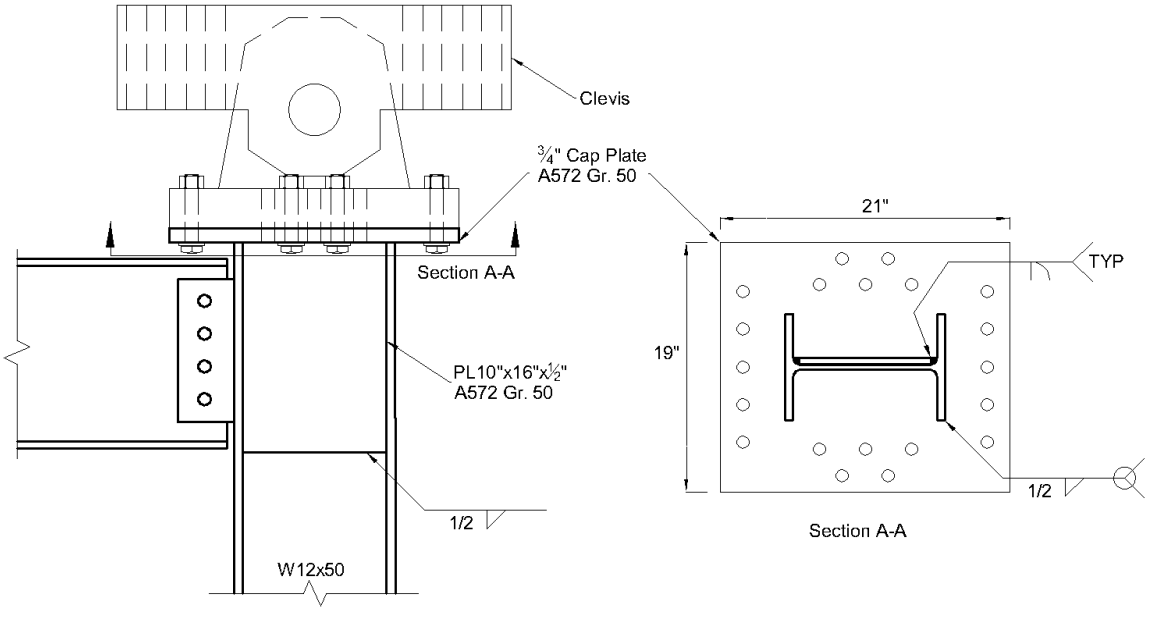

Figure A2.5: Column web doubler detail.

Actuator capacity = 450 kips tension (225 kips/column), 500 kips compression (250 kips/column)
Expected maximum frame resistance = 372 kips (186 kips/column)

W12x50 shear strength
Nominal: $V_n = 0.6F_ydt_w = (0.6)(50\ ksi)(12.2")(0.37") = 135.4$ kips
Available: $0.9(V_n) = 121.9$ kips

Doubler plate required thickness
$t_p > (250\ kips - 121.9\ kips)/[(0.9)(0.6)(50\ ksi)(12.2")]$
$t_p > 0.39"$
→ Use ½" web doubler

Combined shear strength
$\varphi V_n = 0.9(0.6)(50\ ksi)(12.2")(0.37"+0.5") = 286.6$ kips

Doubler plate-to-column weld
CJP groove weld will fully develop doubler plate (see detail).

Column-to-cap plate weld
$0.75(0.6)(70\ ksi)(0.707)[1.5(2*8"+4*2.5")+2*10"]w > 250$ kips
$w > 0.19"$
→ Use 5/16" fillet welds

Appendix 3

Verification of Strain Gauge Data

In order to verify the accuracy of the member forces determined from the strain gauges, various equilibrium checks were performed. Sections A3.1 through A3.3 document these checks. A3.4 provides conclusions based on the results of these studies.

A3.1 Beam total vertical force vs. vertical component of brace force

The total vertical force on the beam, measured with the beam strain gauges, should match the vertical component of the axial load in the braces determined from the brace strain gauges. The beam total vertical force was determined by adding the shear on each half of the beam. The vertical component of the brace axial force was determined by dividing the axial force into its vertical and horizontal components based on the original brace angle. Beam deflection causes the brace angle to reduce, so this calculation becomes less accurate as beam deflection increases. Figure A3.1 shows a comparison of the two forces as a function of drift in each of the 3 tests.

In all three tests, there was a net downward force on the beam at drifts less than 0.5% according to the brace strain gauge data, which was not reflected in the beam strain gauge data. Prior to brace buckling, there should be no vertical force on the beam, which suggests that the beam strain gauge data may be more accurate. The vertical force determined from the brace gauges and beam gauges match well for drifts greater than 1% in Chevron 1 and 2. However for Chevron 3, the measured vertical forces differ by close to 40% at 3% drift. The beam flexural demand determined from the beam strain gauges in Chevron 3 was less than expected based on the amount of yielding observed during the test. It may be that the

beam data is less accurate in Chevron 3 since the brace vertical load was significantly higher than the total vertical load determined from the beam gauges.

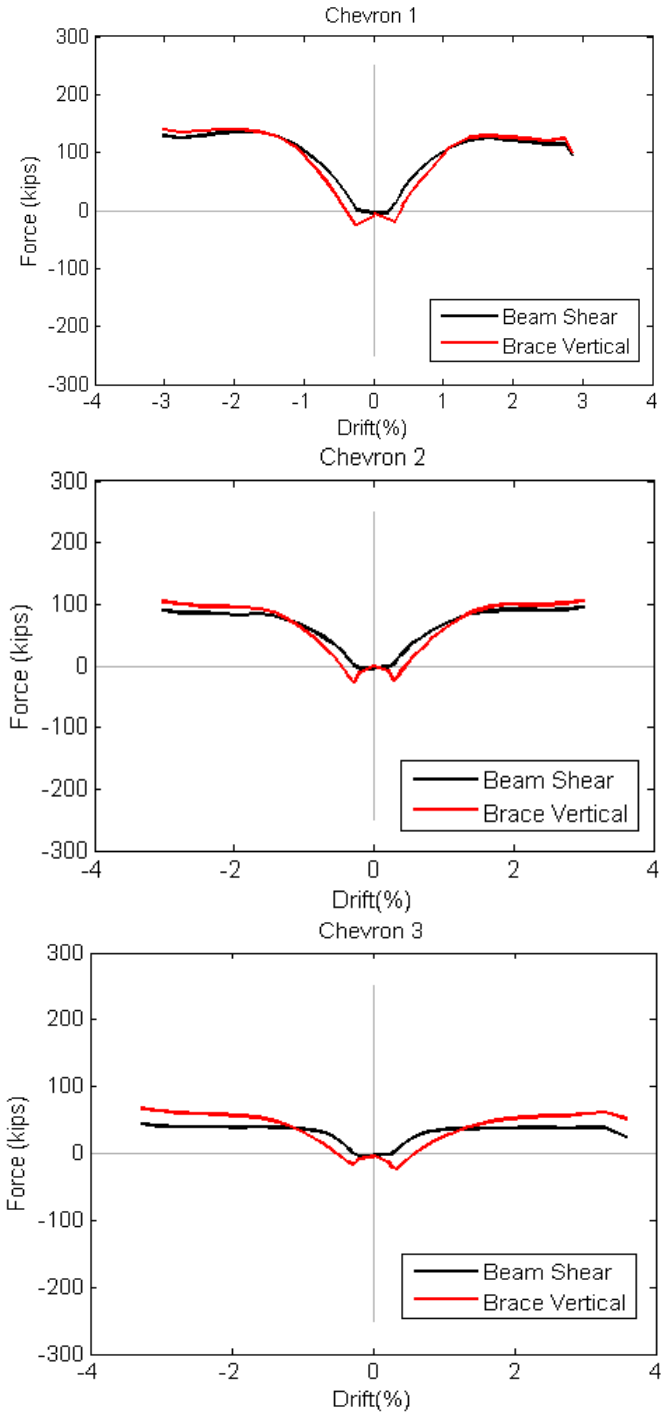

Figure A3.1: Comparison of brace and beam vertical force.

A3.2 Beam total horizontal force vs. horizontal component of brace force

The total horizontal force on the beam as measured by the beam strain gauges should match the horizontal component of the brace axial force determined from the brace strain gauges. The beam total horizontal force was determined by adding the axial load on each half of the beam. The horizontal component of the brace axial force was determined by dividing the axial force into its vertical and horizontal components based on the original brace angle. Beam deflection causes the brace angle to reduce, so this calculation becomes less accurate as beam deflection increases. Figure A3.2 shows a comparison of the two forces as a function of drift in each of the 3 tests.

The horizontal force measured from the beam strain gauges matches remarkably well for Chevron 2. For Chevron 1 and 3, the measured brace horizontal load tends to be larger than the measured beam horizontal load at positive drifts and smaller at negative drifts, but the difference does not exceed 10%.

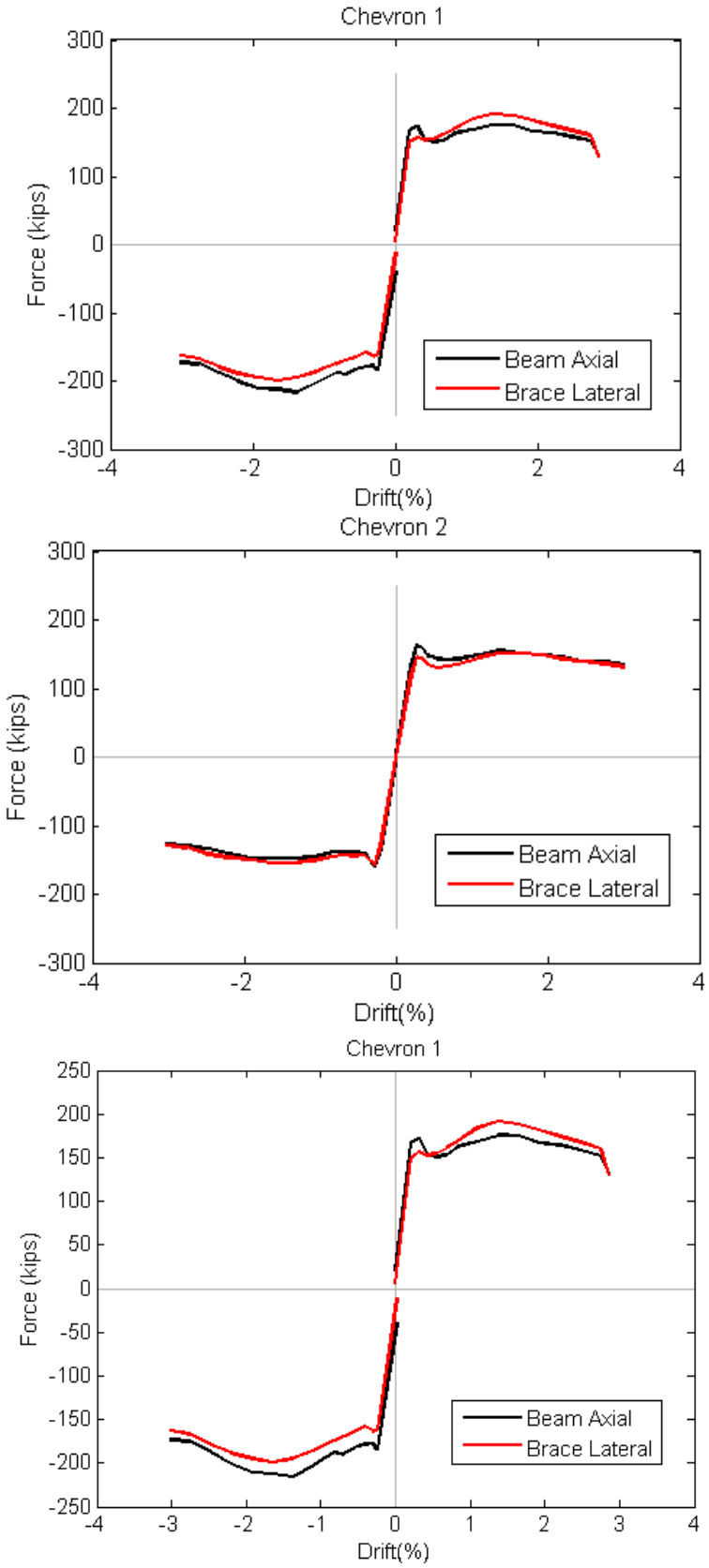

Figure A3.2: Total beam horizontal load versus horizontal component of axial forces in the braces.

A3.3 Actuator force versus component lateral resistance

The total base shear measured by the actuator's internal load cell should equal the horizontal component of the brace axial load plus the shear in the columns. The horizontal component of the brace axial force was determined in the same way as described in Section A3.2. The column shear was determined from the strain gauges on the column as described in Section 5.5. Figure A3.3 shows a comparison of the total base shear and the lateral resistance provided from the columns and braces.

Until brace buckling, the brace lateral force is almost exactly equal to the actuator load. The reversed shear forces in the columns at low drifts do not fit with this observation. At higher drifts, the columns become a larger proportion of the lateral resistance. The lateral resistance from the braces and columns matches well with the actuator force at high drifts in Chevron 2 and 3, but deviates around 10% for Chevron 1.

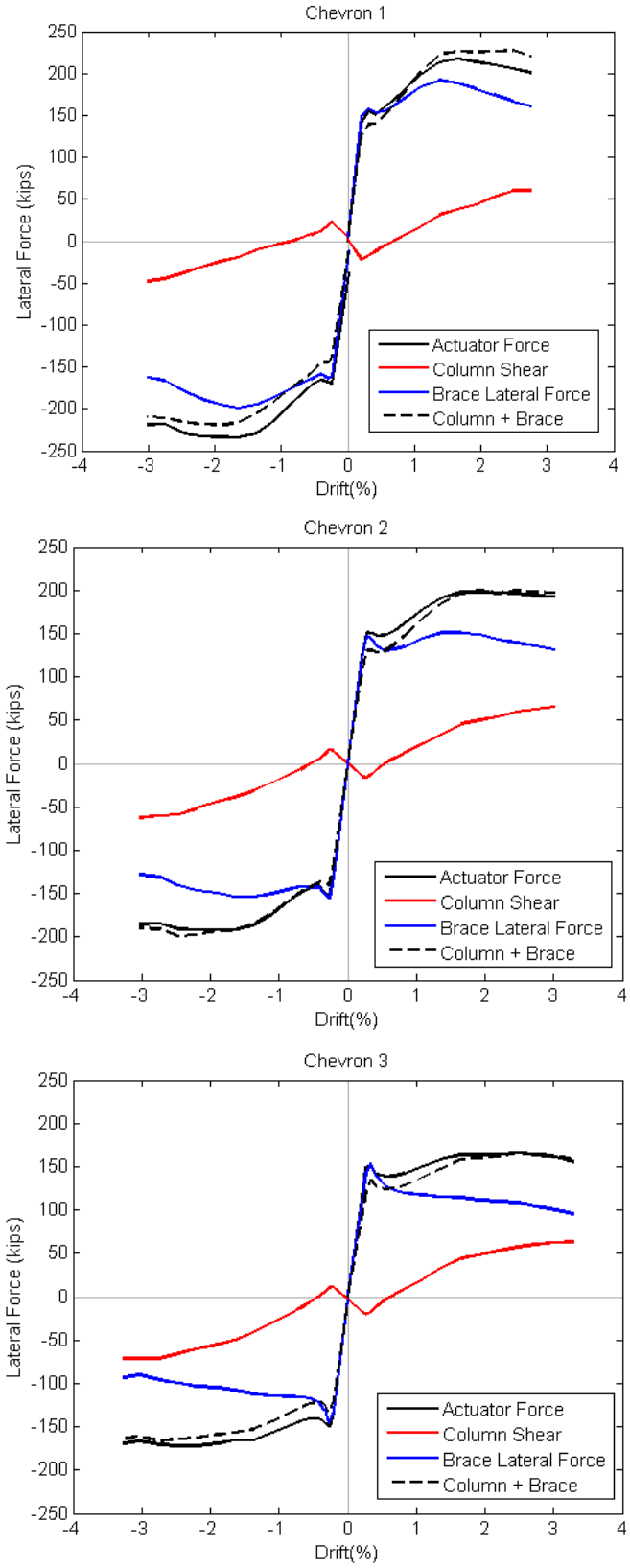

Figure A3.3: Actuator force versus component lateral resistance.

A3.4 Conclusions about strain gauge accuracy

It is clear from the plots in Sections A3.1 through A3.3 that there is some error in the strain gauge data, but in many cases the forces measured by different methods match well, and at their worst they do not differ by more than 10%. The exception is the total vertical load on the beam in Chevron 3; the brace strain gauge data indicated a vertical load 40% greater than that indicated by the beam strain gauge data. The beam flexural demand measured using the beam strain gauges in Chevron 3 barely reached M_y* even though there was significant yielding in the beam top and bottom flanges at relatively low drifts, indicating that the vertical force measured from the brace data is likely to be more accurate than the beam strain gauge data for Chevron 3.